Capriccio For Strings: Collision-Mediated Parallel Transport in Curved Landscapes and Conifold-Enhanced Hierarchies Among Mirror Quintic Flux Vacua

Kate Eckerle

Submitted in partial fulfillment of the
requirements for the degree of
Doctor of Philosophy
in the Graduate School of Arts and Sciences

COLUMBIA UNIVERSITY

2017

ABSTRACT

Capriccio For Strings: Collision-Mediated Parallel Transport in Curved Landscapes and Conifold-Enhanced Hierarchies Among Mirror Quintic Flux Vacua

Kate Eckerle

This dissertation begins with a review of Calabi-Yau manifolds and their moduli spaces, flux compactification largely tailored to the case of type IIb supergravity, and Coleman-De Luccia vacuum decay. The three chapters that follow present the results of novel research conducted as a graduate student.

Our first project is concerned with bubble collisions in single scalar field theories with multiple vacua. Lorentz boosted solitons traveling in one spatial dimension are used as a proxy to the colliding 3-dimensional spherical bubble walls. Recent work found that at sufficiently high impact velocities collisions between such bubble vacua are governed by "free passage" dynamics in which field interactions can be ignored during the collision, providing a systematic process for populating local minima without quantum nucleation.

We focus on the time period that follows the bubble collision and provide evidence that, for certain potentials, interactions can drive significant deviations from the free passage bubble profile, thwarting the production of a new patch with different field value. However, for simple polynomial potentials a fine-tuning of vacuum locations is required to reverse the free passage kick enough that the field in the collision region returns to the original bubble vacuum. Hence we deem classical transitions mediated by free passage robust.

Our second project continues with soliton collisions in the limit of relativistic impact velocity, but with the new feature of nontrivial field space curvature. We establish a simple geometrical interpretation of such collisions in terms of a double

family of field profiles whose tangent vector fields stand in mutual parallel transport. This provides a generalization of the well-known limit in flat field space (free passage). We investigate the limits of this approximation and illustrate our analytical results with numerical simulations.

In our third and final project we investigate the distribution of field theories that arise from the low energy limit of flux vacua built on type IIb string theory compactified on the mirror quintic. For a large collection of these models, we numerically determine the distribution of Taylor coefficients in a polynomial expansion of each model's scalar potential to fourth order. We provide an analytic explanation of the proncounced hierarchies exhibited by the random sample of masses and couplings generated numerically. The analytic argument is based on the structure of masses in no scale supergravity and the divergence of the Yukawa coupling at the conifold in the moduli space of the mirror quintic. Our results cast the superpotential vev as a random element whose capacity to cloud structure vanishes as the conifold is approached.

Contents

List of Figures

Acknowledgements

The mathematics my advisors Brian Greene and Frederik Denef have taught me is impossible to learn alone. Since it is beautiful and I would not trade this knowledge for anything[1], I find it impossibly difficult to articulate my gratitude for the two of you. Various attempts at avoiding cliché resulted in two poems (on the next page).

I am furthermore incredibly lucky to have had the support of wonderful mentors and friends while at Columbia: Rachel Rosen, Alberto Nicolis, Ruben Monten, and Riccardo Penco. I would also like to thank Oliver Janssen, my axionic counterpart at NYU this past year, whose careful reasoning and camaraderie I am truly grateful for.

And to my very first mentor, Richard Holman, if you are on top of a mountain, as I suspect likely is the case, I hope it has the internet. Either way, I will never forget you. Thank you for making me a theorist.

Finally, beautiful as it might be, physics is largely solitary. Maybe some people have the stamina and self-regulating perspective to manage alone. Not me. The unflinching love and support of my family, my parents Ceci and Tom, and brother Matteo, was essential, so I dedicate this to them.

[1] Yes, even a Bernie presidency, though it is an excruciatingly tough call. There's always 2020.

Brian taught me about Calabi-Yau,
to truly say thanks I don't know how.
Told me about their neat topology, and de Rham cohomology.
Though it has been swell, it's time for so-long, farewell —
also to your kids, who know about the Higgs.

Frederik is Belgian, he's really quite tall.
But little creatures rejoice, he stands up first for the small.
Chipmunks and squirrels, mouses and sparrows,
there's more gold in his heart,
than in the crowns of kings and pharaohs.

My twin Teo's the best, he's my mirror manifold.
He's got all Shakespeare's sonnets in his genes' DNA-folds.
Matte, math words are already pretty hard to rhyme,
so I'll have to leave iambic pentameter for another time.

Chapter 1

Introduction

The widespread view is that the Standard Model of particle physics is a low energy effective field theory. In the more fundamental theory the strong and electroweak forces would unify into a single interaction at higher energy. Theories that accomplish this are called Grand Unified Theories (GUTs). It is believed that at an even higher energy scale gravity, the only remaining fundamental force, is also unified and described within the framework of quantum field theory. A theory that accomplishes this would be a Theory Of Everything.

String/M-theory is an attractive candidate. It is also a theory in more than the four spacetime dimensions we observe. This is not disqualifying however because of the suggested abundance of metastable solutions in which the extra spatial dimensions (six for superstring theory) are wrapped up into a manifold of finite — and moreover very small — volume. The compact manifolds, one located at each point in the large dimensions, have special structure. For example, compactifications of superstring theory to flat Minksowski space (which our universe is a weak but nontrivial departure from) that maintain supersymmetry require the internal space to be a Calabi-Yau 3-fold[1].

These manifolds come in continuous families. Each family has a unique identifier; a set of numbers that contain only topological information. The parameters that vary across a given family are complex valued, and are called moduli. There are typically a very large number of them, on the order of hundreds, and in these large-

[1] Orientifolds in the case of IIb.

dimensional moduli field spaces there are a tremendous number of local minima of the potential energy. This vast space of possibilities — the ways of wrapping up the extra dimensions — and the undulating potential energy density they correspond to is termed the *string landscape*.

The moduli enter the effective field theory that results upon compactification — supergravity — as dynamical complex valued scalar fields: they describe how the Calabi-Yau vary from one 4-dimensional spacetime location to the next. Field configurations that are spatially homogeneous and locally minimize the energy density are stable at the classical level. Whether or not the absolute minimum energy density of the theory is attained is irrelevant in determining stability. A basic result of quantum field theory, on the other hand, is that only quantum states with field expectation values that globally minimize the potential are arbitrarily long lived[2]. The quantum state underlying a homogeneous field configuration that only locally minimizes the energy density is *metastable* — quantum fluctuations inevitably cause it to decay.

Loosely speaking, quantum fluctuations in a given spatial volume can violate energy conservation and change the field value(s) there to value(s) inside the basin of attraction of a new local minimum of the potential, and particularly one of lower energy density. Just as a quantum mechanical system in its ground state can be observed at a classically forbidden location, the field in a given spatial volume can tunnel through a potential barrier from a false vacuum configuration to one of lower energy.

In the first of the Fate of The False Vacuum papers [1], Sidney Coleman draws an analogy between vacuum decay in quantum field theory and phase transitions in ordinary fluids; from the superheated liquid phase to the vapor phase. The super-

[2]Gravitational effects on vacuum decay are outside the scope of the research that appears in this document, so we neglect uptunneling throughout.

heated liquid phase is not arbitrarily long lived, despite the fact that it corresponds to a local minimum of the free energy (as a function of density). Bubbles of the vapor phase with various sizes appear within the fluid due to thermal fluctuations. Bubbles smaller than some critical size collapse due to their surface tension. Though large bubbles are of course less likely to appear than small ones, bubbles that are larger than the critical size *expand* because their gain in volume energy overcomes their loss to surface energy. These large bubbles mediate the phase transition. Similarly, quantum fluctuations cause expanding regions — bubbles — of lower energy density vacuum to appear in the initially homogeneous false vacuum field configuration. The false parent vacuum decays away just as the superheated liquid boils away.

The picture to have in mind then is that our observable universe evolved from a patch of a much larger cosmos in which a rich variety of bubble universes — vacua in the string landscape — nucleate, expand and potentially interact with one another. The goal, still beyond reach, is to compare our universe with the late time demographics of such a multiverse. I believe such a comparison has the capacity to explain observable features of our universe currently deemed mysterious by appealing to dynamics.

1.1 Flux Compactification

The strength of interactions in quantum field theory (encoded by the associated couplings) depends on the background energy scale. This is a consequence of renormalization. The *running* of couplings is described by the renormalization group equations. This enables unification of all the Standard Model gauge interactions. Supersymmetric theories with the appropriate gauge group structure, namely those which can be broken into the Standard Model gauge group, have been the the most popular GUTs since the 1980's (though there are also non-supersymmetric GUTs). For example, the

frequently cited value of 10^{16} GeV for the GUT scale comes from the Minimal Supersymmetric extension of the Standard Model (MSSM) which is based on SU(5) and gives couplings that converge around that order. Quantum effects to gravitational interactions on the other hand are expected at the Planck scale, $\sqrt{\hbar c^5/G} \sim 10^{19}$ GeV.

One reason gauge unification has predominantly been realized in supersymmetric models is because the proposed symmetry between fermions and bosons has to potential to resolve what would otherwise be a fine-tuning of UV theory's bare parameters that leaves the small observed Higgs mass $\sim 10^2$ GeV (small relative to the cut-off energy scale, GUT or Planck). A "cut-off" is the scale at which a given effective field theory ceases to be a valid description of the physics. The Higgs mass receives loop corrections that individually diverge quadratically in the cut-off. For example, the diagram consisting of a single top quark loop gives a contribution $\sim 10^{34}$ times larger than the bare mass when the cut-off is taken at the Planck scale [2]. To yield the comparably much smaller observed Higgs mass a tremendous coincidence would need to take place wherein the large radiative corrections merely cancel off most of the bare mass of near equal value.

This fine-tuning is avoided if supersymmetry is broken "softly" around a TeV. Essentially, there is near cancellation between the divergent diagrams of SUSY partners which renders the small Higgs mass technically natural. However, with the LHC having found no SUSY at several TeV it is becoming clear that the soundness of this expectation should be reevaluated. There are nevertheless different motivations for SUSY which are unconcerned with however high the scale of SUSY breaking might be. These more resilient considerations are rooted in quantum field theory (QFT), particularly in aspects a QFT's symmetry groups, and the implications this has for theories of quantum gravity.

Coleman and Mandula proved a no-go theorem regarding how the spacetime symmetries and internal symmetries of a QFT can be combined. Specifically, the sym-

metry group G of the S-matrix of a QFT is restricted to be the direct product of the Poincaré group (global) an internal group (local) if G contains a subgroup that is locally isomorphic to the Poincaré group, and the QFT is to have certain basic/reasonable attributes [3]. These characteristics include, for example, that the QFT have finitely many different particle types below any finite energy scale. In terms of the Lie algebra of G, the generators of the spacetime symmetries commute with those of the internal symmetries (for example generators of gauge symmetries in the Standard Model).

Coleman and Mandula did not allow for anti-commutators in the symmetry algebra. Haag, Łopuszański, and Sohnius showed that if these are permitted you can extend to supersymmetry, but go no further. So, supersymmetry becomes the only nontrivial extension of Poincaré and internal [4], [5].

Superstring theory in flat or weakly curved Minkowski space only exists in ten dimensions. There are five superstring theories: type I, type IIa, type IIb, heterotic $\mathrm{E}_8 \times \mathrm{E}_8$, and heterotic SO(32). They can be viewed as different limits of M-theory, which itself is a supersymmetric theory of quantum gravity in one dimension higher, eleven. All the different formalisms are related to one another by S and/or T-duality. These identify the weak coupling regime of one theory with the strong coupling regime of another (S-duality), or swap the compact length scale R in one theory with its inverse $1/R$ in another. Finally, there is a formulation in 12 dimensions known as F-theory. While the full extent of its interpretation is unsettled, it can cautiously be thought of as a geometric formulation of IIb theory, in a particular sense.

A plausible explanation of the excess dimensions of these theories from the four we observe is that the additional ones range over a compact and exceedingly small space, Y. More precisely, the full spacetime is written as the direct product of Y

with an observed 4-dimensional Lorentzian manifold M_4. For instance,

$$M_{10} = M_4 \times Y \tag{1.1.1}$$

for the superstring theories. If the length scale of the compact manifolds, one located at each point in M_4, is much smaller than the distances the LHC is capable of probing physics on, $L_{\text{LHC}} \sim 10^{-19}$ m, they would not be detectable. The manifolds could nevertheless be *large* compared to the string length, ℓ_s, the only free parameter in string theory[3]. This is because, modulo the string coupling, the string length is the Planck length, order 10^{-34} m, which is many orders of magnitude smaller than L_{LHC}. In this case classical notions of geometry are valid. Integrals over the compact space can be performed unambiguously and effective field theories from compactification retrieved. We proceed with Y such that,

$$L_{\text{LHC}} \approx 10^{-19} \text{ m} \gg \text{Vol}(Y)^{1/6} \gg L_{\text{pl}} \approx 10^{-34} \text{ m}, \tag{1.1.2}$$

though it should be noted the second assumption is made for the purposes of tractability. There is no reason to expect this a priori.

The low energy approximation to string/M-theory is 10/11-dimensional supergravity. The mathematical structure of Y determines the characteristics of the effective theory following compactification, for instance its symmetries. If the 4-dimensional theory is to retain some amount of supersymmetry, a covariantly constant spinor has to exist on the compact manifold [6]; in other words a spinor which does not change upon parallel transport. For the 6-dimensional case we can make use of the fact that the spin group Spin(6), the double cover of SO(6), and SU(4) are isomorphic. In the 4-dimensional representation spinors transform under rotations of the 6-space simply by matrix multiplication. Note that if the constant spinor exists,

[3]Equivalently the string tension $T = \frac{1}{2\pi\alpha'}$, where $\alpha' \equiv \ell_s^2$.

we can always choose a basis in which it is given by

$$\begin{pmatrix} 1 \\ 0 \\ 0 \\ 0 \end{pmatrix}. \tag{1.1.3}$$

All elements of $\mathrm{Hol}(Y)$ have to act trivially on this vector, in other words, can only act nontrivially on the bottom 3 components of a generic 4-vector. Thus they have the form,

$$\begin{pmatrix} 1 & \mathbf{0}^\top \\ \mathbf{0} & A \end{pmatrix}. \tag{1.1.4}$$

Since the determinant of the full 4×4 has to be one, the matrices A have to be in SU(3). Clearly this set of 4×4 matrices forms a group. We conclude, SU(3) this is the largest subgroup of SO(6)[4] that can serve as a holonomy group of compact manifold Y and still yield a supersymmetric effective theory upon compactification. Compact manifolds with SU(3) holonomy are Calabi-Yau 3-folds.

The 7-dimensional manifolds relevant to M-theory that satisfy the analogous condition are those with G_2 holonomy. Both are examples of manifolds with what is known as *special holonomy*. Both admit Ricci-flat metrics. To summarize, the heterotic theories and type I on Calabi-Yau 3-folds, type II on Calabi-Yau orientifolds[5] and M-theory on G_2 holonomy manifolds yield effective field theories with $\mathcal{N} = 1$ SUSY in Minkowski space [7]. The F-theory realization of IIb involves elliptically fibered Calabi-Yau 4-folds.

Integrating the relevant higher-dimensional supergravity action over the compact manifold gives rise to complex scalar fields in the lower-dimensional theory. One of

[4]The holonomy group filled out by a generic 6-dimensional manifold is SO(6).

[5]Orientifold planes reduce the $\mathcal{N} = 2$ to $\mathcal{N} = 1$ supersymmetry (SUSY).

these is known as the "dilaton" ϕ and is associated with the string coupling by $g_{\rm s} = e^{\phi}$. Others — geometric moduli — of which there are typically very many, describe how the compact manifolds smoothly vary from point to point in the four large dimensions. They are intimately related to the cohomology classes of the compact manifold. Before delving into further the intricate (decidedly elegant) details of these manifolds we discuss a toy model of compactification that illustrates some of the basic features of the procedure.

This is Kaluza-Klein reduction on a circle. Prior to compactification this is a theory of pure gravity in empty 5-dimensional spacetime, so for its action we take only the Einstein-Hilbert term,

$$S_5 = -\frac{1}{16\pi G_5}\int d^5x\ \sqrt{-\tilde{g}}\ \tilde{R} \tag{1.1.5}$$

where G_5 and $\tilde{R}$ are the 5-dimensional Newton constant, and scalar curvature, respectively. In terms of a 5-dimensional Planck mass, the overall factor is $2M^3_{\rm pl,5}$. The curvature is computed from Ricci-tensor for the spacetime metric,

$$ds^2 = \tilde{g}_{MN}dx^M dx^N \tag{1.1.6}$$

$$\tilde{g}_{MN} = \begin{pmatrix} g_{\mu\nu} & \tilde{g}_{\mu 5} \\ \tilde{g}_{5\nu} & \tilde{g}_{55} \end{pmatrix} \tag{1.1.7}$$

where the first four dimensions will serve as our non-compact directions using signature $+---$, and the fifth as our extra spatial dimension. To proceed with reduction on a circle we make the identification $y \equiv x_5 \simeq x_5 + 2\pi r$ and, for reasons that will become apparent momentarily, relabel the components of the metric as follows

$$\tilde{g}_{MN} = \begin{pmatrix} g_{\mu\nu} + \kappa\phi^2 A_\mu A_\nu & \kappa\phi^2 A_\mu \\ \kappa\phi^2 A_\nu & \phi^2 \end{pmatrix}. \tag{1.1.8}$$

By taking all fields in 1.1.8 independent of y it can be shown that reduction of 1.1.5 over the circle $\int d^5x \to \int d^4x \int_{S^1} dy$ gives [8]

$$S_{eff} = -\int d^4x\sqrt{-g}\phi \left(\frac{1}{16\pi G_4}R + \frac{1}{4}\phi^2 F_{\mu\nu}F^{\mu\nu} + \frac{2}{3\kappa^2}\frac{\partial_\mu\phi\partial^\mu\phi}{\phi^2}\right) \tag{1.1.9}$$

where R is the 4-dimensional Ricci scalar, and we've defined the field strength $F_{\mu\nu} \equiv \partial_\mu A_\nu - \partial_\nu A_\mu$, the 4-dimensional Newton constant G_4 and related Einstein-Hilbert constant κ as

$$G_4 = \frac{G_5}{2\pi r}, \quad \kappa^2 = 16\pi G_4. \tag{1.1.10}$$

Imposing the y-independence of all metric degrees of freedom, also known as the "cylinder condition", amounts to taking only the zero modes of a Fourier series expansion (in y) of the fields with full 5-dimensional dependence; the idea being that if the circle is very small all subsequent modes are above the cut-off of the theory, see for instance [9]. Traditionally the scalar ϕ is set to a 1 to, somewhat miraculously, give a theory of Einstein gravity coupled to Maxwell electromagnetism. The virtue of this calculation is the simplicity with which it unifies electromagnetism with gravity; deriving it from the vacuum of spacetime in one dimension higher[6].

Some of the important results of actual supergravity compactifications can be gleaned by keeping the scalar $\phi(x^\mu)$ in the toy example's effective description. Compactification of supergravity on Calabi-Yau manifolds results in the production of scalar fields φ^i just as Kaluza-Klein on a circle. These fields φ^i parameterize the internal geometry exactly like $\phi(x^\mu)$ does in the Kaluza-Klein example where the circle is described by a single scalar, the radius $r\phi$. Continuing to suspend detailed discussion of Calabi-Yau moduli until section 1.2, we simply note here that an overall volume modulus can always be identified; a higher dimensional analog of the radius.

[6]It should be noted that this is meant as an illustrative example. There are incompatibilities with observation, for example the mass of the electron it predicts.

This volume modulous appears in the expression for the 4-dimensional Planck mass in terms of the D-dimensional supergravity theory. The scaling is the straightforward expectation,

$$M_{\mathrm{pl},D}^{D-2} \sim M_{\mathrm{pl},4}^{2}\,\mathrm{Vol}(Y). \tag{1.1.11}$$

The second important feature is the fact that in the absence of sources in the D-dimensional theory, the scalars proliferated by compactification are massless, just as in 1.1.9. Since massless scalars are not consistent with observations, an abundance of them is problematic. Quantum corrections are of course expected to change this classical triviality of the potential, but quantum corrections are — in a fundamental sense — incapable on their own of curing the masslessness of the moduli. We follow the explanation of this insufficiency, an instance of the Dine-Seiberg problem [10], given by Denef in [7].

Quantum corrections are expected to be significant when the compactification length scale $\varrho \sim (\mathrm{Vol}(Y)/{\ell_s}^6)^{1/6}$ is small, and/or when the string coupling $g_{\mathrm{s}} = e^{\phi}$ is large[7]. In the same breathe, corrections should vanish in the limit of large volume or weak coupling, restoring the potential to zero.

Quantum corrections can contribute either positively or negatively to the energy density. So, as a function of either one of the real dimensionless scalars ϱ or g, the potential V can approach zero asymptotically either from above (positive corrections at large value of the modulus) or from below (negative corrections). If the former is the case, the potential decays to zero as the scalar grows and the modulus is unstabilized at large values; the direction $\varrho \to \infty$ or $1/g_{\mathrm{s}} \to \infty$ is a runaway direction in moduli space. If the latter is the case and leading order corrections are negative then the modulus is pulled into the small ϱ, or strong coupling region. The essential problem is that higher order corrections cannot be appealed to produce a local min-

[7]The overall volume is itself a function subvolumes of the manifold (the 2-cycle volumes for a Calabi-Yau 3-fold) which might vary widely. For the heuristic description it suffices to consider the behavior of corrections as the overall volume grows.

imum at smaller ϱ or inverse coupling, because a term which produces a dip in an otherwise monotonically decreasing/increasing function *exceeds the bounds of what can legitimately be deemed a higher order "correction."*

A significant step was realizing that turning on nontrivial background configurations for the higher-form fields allowed by the symmetries of supergravity can generate a potential at tree-level for the moduli. Compactification in the presence of these sources — flux compactification — involves p-form fluxes that wrap nontrivial cycles of Y. These fluxes generate a superpotential W and in turn a scalar potential V for the moduli. The local minima of this flux potential — flux vacua — would correspond to optimal Calabi-Yau geometries for compactifying the extra dimensions. The vacua can be either supersymmetric or non-SUSY.

For instance, IIb theory involves Ramond-Ramond (RR) and Neveu Schwartz-Neveu Schwartz (NSNS) 3-form field strengths $F_{(3)}$ and $H_{(3)}$, each defined as the exterior derivative of their associated 2-form potentials $F_{(3)} := dC_{(2)}$ and $H_{(3)} := dB_{(2)}$. The term in the supergravity action responsible for producing the moduli potential at tree-level is

$$\frac{2\pi}{\ell_s^8}\int \frac{1}{\mathrm{Im}(\tau)} G_{(3)} \wedge *\overline{G_{(3)}} \ \subset S_{\mathrm{IIb}} \tag{1.1.12}$$

where we've defined the total 3-form flux $G_{(3)} := F_{(3)} - \tau H_{(3)}$ in terms of the axio-dilaton τ, the complex scalar related to the dilaton by $\tau := C_{(0)} + ie^{\phi}$, where the "zero-form" is just a real constant. The 3-form field configurations that wrap internal dimensions are quantized in units determined by the compact geometry.

The term 1.1.12 for such a wrapped configuration gives, upon integration over the Calabi-Yau Y, a no scale $\mathcal{N} = 1$ SUSY scalar potential. The set of scalars φ^m this potential involves clearly includes the axio-dilaton for whom we reserve the zero index, $\varphi^0 := \tau$, via $G_{(3)}$. The remaining scalars parametrize the Calabi-Yau geometry.

Calabi-Yau manifolds are Kähler. They can be deformed smoothly by varying the complex structure or by varying the Kähler form (or both). The independent deformations of a given Calabi-Yau are tied to its cohomology groups — there are $h^{2,1}$ complex scalars z^I needed to specify the complex structure, and $h^{1,1}$ real scalars v^A, simply the volumes of 2-dimensional homology cycles, needed for the Kähler form. The Kähler moduli (the second type) enter the tree-level scalar potential only in a specific combination which, moreover, appears only as an overall multiplicative factor; as the inverse square of the dimensionless Calabi-Yau 6-volume $\mathcal{V}_0 := \mathrm{Vol}(Y)/\ell_s^6$.

In particular, the no scale $\mathcal{N} = 1$ SUSY scalar potential is

$$V(\varphi, \bar{\varphi}) = \frac{M_{\mathrm{pl}}^2}{4\pi} e^{\mathcal{K}} \; \mathcal{K}^{I\bar{J}} \; D_I W \; D_{\bar{J}} \overline{W}. \tag{1.1.13}$$

where indices run from zero to $h^{2,1}$ only, with $\varphi^I := z^I$ for all natural number indices. W is the Gukov-Vafa-Witten holomorphic superpotential generated by the 3-form flux,

$$W(\varphi) = \int_Y G_{(3)} \wedge \Omega, \tag{1.1.14}$$

Ω is the Calabi-Yau's nowhere vanishing holomorphic 3-form, $\mathcal{K}$ is the Kähler potential for the full moduli space, D_I is the Kähler covariant derivative defined from it,

$$D_I := \frac{\partial}{\partial \varphi^I} + \frac{\partial \mathcal{K}}{\partial \varphi^I} \tag{1.1.15}$$

and the contraction in 1.1.13 is taken with the inverse of the Kähler metric on moduli space $\mathcal{K}_{I\bar{J}} := \partial_I \partial_{\bar{J}} \mathcal{K}$. Though excluded from the superpotential, the Kähler moduli appear in the $e^{\mathcal{K}}$, specifically in the combination $1/\mathcal{V}_0^2$. Specifically, at the classical level

$$\mathcal{K} = -\log\left(-i(\tau - \bar{\tau})\right) - \mathcal{K}^{\mathrm{cs}} - \log\left(\mathcal{V}_0^2\right). \tag{1.1.16}$$

Hence, the $\sim |DW|^2$ contains no dependence on the 2-cycle volumes. The term "no

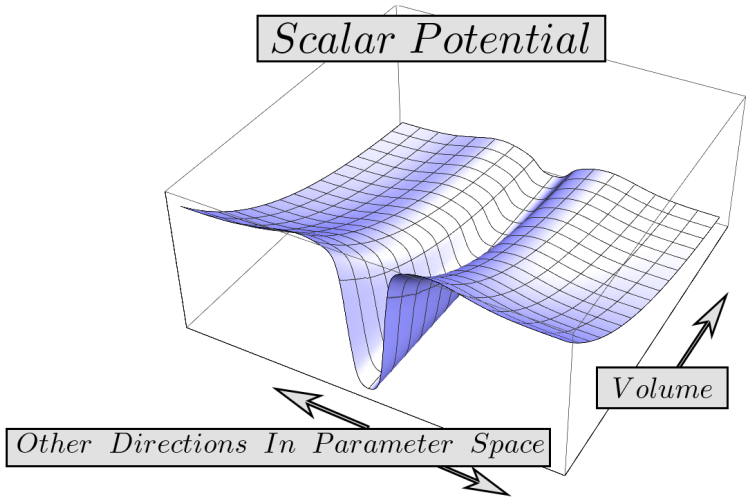

Figure 1.1: The qualitative dependence of the scalar potential on the volume of a Calabi-Yau manifold.

scale" refers to the volume-independence of 1.1.13's global minima, zeros. These are solutions to the SUSY condition $D_I W = 0$. At generic points in moduli space, on the other hand, the potential is nonzero and the direction of increasing Calabi-Yau volume in moduli space is a runaway direction. A schematic illustration can be found in figure 1.1.

The "no scale" structure found at tree-level is entirely a result of the Calabi-Yau special geometry. In general, quantum corrections break this, resulting in the standard expression for an $\mathcal{N} = 1$ theory,

$$V(\varphi, \bar{\varphi}) = \frac{M_{\rm pl}^2}{4\pi} e^{\mathcal{K}} \left(\mathcal{K}^{a\bar{b}} \, D_a W \, D_{\bar{b}} \overline{W} - 3|W|^2 \right), \tag{1.1.17}$$

where indices now include Kähler moduli; the complex indices for these refer to the complexified Kähler moduli whose axionic parts come from the self dual 5-form $\tilde{F}_5$. A full derivation of the tree-level potential 1.1.13 from the term 1.1.12 in the IIb supergravity action can be found in chapter 4 section 4.1, and Calabi-Yau moduli space is reviewed in the following section of this chapter, section 1.2.

The extremely large number of distinct consistent wrapped flux configurations (the different quanta of RR and NSNS 3-form flux in 1.1.14 in the case of IIb) gives rise to the notion of an enormous landscape, the earliest recognition of this being [11]. Our universe would be identified with one of the great number of diverse string vacua. Across the many patches of a much greater cosmos the effective actions that describe nature vary, as they are expansions about different backgrounds, and along with them the vacuum energy density, particle content/masses, types and strengths of interactions that take place etc. This has implications for the naturalness of certain observables. Our universe's Cosmological Constant (CC), equivalently the vacuum energy density, is unnaturally small; another problem of fine-tuning problem much like the small electroweak scale, only many orders of magnitude more egregious.

The proper way to understand probability in the context of a landscape is unclear, but roughly speaking if life requires a CC within a small window and most of the patches in the cosmos are thereby rendered barren, then the verdict of "unnatural" would change by conditioning on the fact that we are around to observe the exceedingly small CC. The judgement of whether a certain parameter is natural or not depends not only on basic dimensional analysis using the vacuum's observed parameters, but also on whether the parameter's taking on that value makes the universe inhospitable to observers. It's even plausible the small electroweak scale might fall into this category too, potentially a prerequisite for the infrastructure necessary to support intelligent life, as some have suggested [2].

For this kind of Anthropic Principle [12] to be used, it is important to confirm the expected diversity among string vacua, and that ones like ours with exceedingly small CC are included. In other words, it is essential to show that the tools of flux compactification and quantum corrections can be combined in such a way to stabilize moduli while generating a nontrivial but small positive vacuum energy *in a controlled way*. The KKLT scenario [13] is the best known procedure for achieving

this. Important works leading up to KKLT include [14], [15], [16], [17], [18].

Next we turn to building some of the basic machinery — Calabi-Yau manifolds and their moduli space.

1.2 Calabi-Yau Manifolds

Definition Of A Calabi-Yau

In this subsection we briefly review the essential background that is required to define a Calabi-Yau manifold, following [19].

The following notions from complex geometry are necessary. First, a complex manifold is an even-dimensional real manifold that *admits a complex structure*. A complex structure $\mathcal{J}$ is a map from the tangent space at a point p in Y to itself such that: 1. when applied twice each tangent vector maps to itself times negative one, and 2. the Nijenhuis tensor vanishes. More precisely, a complex manifold consists of the pair $(\mathcal{J}, Y)$ such that

$$\mathcal{J} : T_pY \to T_pY, \quad \mathcal{J}^2 = -1 \tag{1.2.1}$$

$$N \equiv [U, V] + \mathcal{J}[\mathcal{J}U, V] + \mathcal{J}[U, \mathcal{J}V] - [\mathcal{J}U, \mathcal{J}V] = 0 \tag{1.2.2}$$

where the square braces denote Lie brackets, and U and V are any two vector fields on Y. Or in component form,

$$\mathcal{J}^i_b \mathcal{J}^b_c v^c = -v^i \quad \forall\ \boldsymbol{v} \in T_pY \tag{1.2.3}$$

$$N^i{}_{jk} \equiv \partial_j \mathcal{J}^\ell{}_k \mathcal{J}^i{}_\ell - \mathcal{J}^\ell{}_j \partial_\ell \mathcal{J}^i{}_k - \partial_k \mathcal{J}^\ell{}_j \mathcal{J}^i{}_\ell + \mathcal{J}^\ell{}_k \partial_\ell \mathcal{J}^i{}_j \tag{1.2.4}$$

A map $\mathcal{J}$ that satisfies the first without necessarily satisfying the second is called an "almost complex structure." In this more relaxed context, those which satisfy the

second as well are referred to an *integrable*.

When both conditions are satisfied it means there is a manner to define complexified coordinates which have the property that the transition functions (between coordinates systems in overlapping patches) are holomorphic. This is a significantly more stringent condition than the mere differentiability of the transition functions one requires for a manifold to be smooth. For a generic even-dimensional real manifold the complex-valued "transition functions" obtained by complexifying the coordinates, say in the canonical manner,

$$y_a = x_a + i x_{\frac{n}{2}+a}, \quad a = 1, \ldots, n/2 \tag{1.2.5}$$

typically will not happen to solve the Cauchy-Riemann equations. Throughout we will distinguish between real coordinates and complex coordinates with indices $i, j, k, \ldots$ and $a, b, c \ldots$, respectively. We'll take the real dimension n to be equal to $2d$ unless otherwise stated.

On top of the differentiability of transition functions, the complex structure provides the requisite additional structure for the notion of a holomorphic function on Y to be well-defined. This is analogous to the way smoothness enables notion of differentiable functions on manifold, and at a more primitive level, the way satisfying the conditions for being a topological space enables a notion of continuity.

Clearly, regardless of whether a complex manifold Y is viewed in real or complex coordinates, the dimensionality in the sense of how many real numbers in an ordered list are required to uniquely specify a point p in Y is the same, $n = 2d$. However, it is worthwhile to expand the tangent space from the n-dimensional T_pY spanned by $\{\partial/\partial x^i|_p\}$ when using complex coordinates. In particular we consider the $\mathbb{C}$-linear span of the (local) complex coordinate basis vectors without assuming any special relation between coefficients of holomorphic and antiholomorphic components. This

defines the complexified tangent space,

$$T_pY^{\mathbb{C}} = \left\{ \boldsymbol{w} = w^a \frac{\partial}{\partial y^a}\bigg|_p + w^{\bar{b}} \frac{\partial}{\partial \bar{y}^{\bar{b}}}\bigg|_p : w^a \in \mathbb{C} \text{ and } w^{\bar{b}} \in \mathbb{C} \right\} \tag{1.2.6}$$

which note has real dimension $2n$.

Next, recall that a metric $g(\cdot, \cdot)$ consists of a set of inner products on the tangent spaces of a manifold. A real manifold equipped with a smoothly varying (from point to point in the manifold) metric or set of inner products is called a Riemannian manifold. The metric g evaluated at an arbitrary point $p \in Y$ is a symmetric bilinear map from $T_pY \times T_pY$ to the reals which allows one to compute distances along curves on the manifold. The set of one-forms $\{dx^1, dx^2, \ldots, dx^n\}$, where we've suppressed the "evaluated at point p" notation, are a local basis for the dual to the real tangent space at a point $p \in Y$. The elements $dx^i \otimes dx^j$ then form a local basis for the metric. Specifically we may write the metric as,

$$g = g_{ij} dx^i \otimes dx^j \tag{1.2.7}$$

where the $n \times n$ matrix of coefficients g_{ij} is symmetric.

For Y a complex manifold, a complex version of the metric may be constructed straightforwardly. The complex metric then is a map from $T_pY^{\mathbb{C}} \times T_pY^{\mathbb{C}}$ to $\mathbb{C}$. Its components in local coordinates can be obtained directly from the real metric. They are symmetric under exchange of indices, whether of like or of mixed type, and respect complex conjugation, i.e. $\overline{g_{ab}} = g_{\bar{a}\bar{b}}$ and $\overline{g_{a\bar{b}}} = g_{\bar{a}b}$. Now, if all components of like-index type, g_{ab} and $g_{\bar{a}\bar{b}}$, vanish the metric is called *hermitian*. This is equivalent to "compatibility" of the real metric and complex structure $\mathcal{J}$ in the following sense,

$$g(\boldsymbol{u}, \boldsymbol{v}) = g(\mathcal{J}\boldsymbol{u}, \mathcal{J}\boldsymbol{v}). \tag{1.2.8}$$

From a hermitian metric we may build the $(1,1)$-form J which we'll call the Kähler form,

$$J = ig_{a\bar{b}}\, dy^a \wedge d\bar{y}^b. \tag{1.2.9}$$

A *Kähler* manifold is one for whom the Kähler form is closed, $dJ = 0$. A direct consequence of this is that the metric components can be expressed as the partial derivatives of a scalar function K,

$$g_{a\bar{b}} = \frac{\partial^2 K}{\partial y^a \bar{y}^b}. \tag{1.2.10}$$

$K(y, \bar{y})$ is referred to as the Kähler potential.

On Kähler manifolds parallel transport using a connection compatible with the metric — the unique procedure for moving tangent vectors along curves such that the relative angles between any given pair of tangent vectors as well as the length of each vector remain fixed — simplifies significantly owing to the restricted form of the Kähler metric. In particular, the holomorphic and anti-holomorphic components of all tangent vectors remain separate upon parallel transport along any curve in Y because 1.2.10 implies the only nontrivial Christoffel symbols are those whose indices are all of like-type.

Now, the holonomy group of a manifold consists of the entire set of possible linear transformations (matrices) that describe how tangent vectors are modified upon parallel transport about closed paths in the manifold. For this reason the separation between the holomorphic and anti-holomorphic subspaces of a Kähler manifold's tangent spaces can be stated precisely in terms of its holonomy group, $\mathrm{Hol}(Y)$: the group must be contained in $U(d)$. While a generic Kähler manifold fills out all of $U(d)$, a Calabi-Yau manifold only fills out $SU(d)$. This restriction completes the definition: a Calabi-Yau d-fold is a compact Kähler manifold with $SU(d)$ holonomy.

An equivalent statement can be given in terms of Chern classes. The condition

of $SU(d)$ holonomy is equivalent to vanishing of the first Chern class. We conclude this subsection with a statement of Yau's theorem: for a Calabi-Yau manifold with Kähler form J there exists a form J' in the same cohomology class as J such that the metric associated to J' is Ricci-flat [20]. In other words, the Kähler form constructed from the metric on a Calabi-Yau in arbitrarily chosen coordinates differs from that of a Ricci-flat metric merely by an exact form.

Moduli Space of Calabi-Yau Manifolds

A given Calabi-Yau manifold can be deformed continuously without violating any of the conditions for being Calabi-Yau. There are two distinct types of deformations — those associated with changing the complex structure $\mathcal{J}$, and those associated with changing the Kähler form, J. These parameters, or *moduli*, are complex-valued[8]. For each Calabi-Yau there are finitely many moduli.

In this subsection we highlight key results, sometimes providing only abridged derivations. We follow Candelas and de la Ossa mainly, and direct the reader to [21], [22] for further detail. Other references include [23], [24]. In an effort to avoid confusion, we'll use indices $a, b, c, \ldots$ ($\bar{a}, \bar{b}, \bar{c} \ldots$) to denote holomorphic (anti-holomorphic) components. When we mean that an object is expressed in the real coordinates we'll use $i, j, k, \ldots$. We'll continue to label complex coordinates on the Calabi-Yau by y^a and real coordinates by x^i.

Each set of moduli — those which vary the complex structure and those which vary the Kähler class — spans an inner product space that is meaningfully thought of geometrically. The full moduli space not only separates locally into the direct product of these two subspaces (i.e. the metric on the moduli space in local coordinates does

[8]More precisely, the parameters that describe deformations of J alone are real scalars. They are, quite literally, associated with changing the volumes of 2-cycles. These real moduli are "complexified" by incorporating the NSNS 2-form potential B. The resulting complex scalars associated with the 2-cycles of Y are then said to parameterize the complexified Kähler cone.

not mix moduli of different type), but each subspace itself has significant structure. Each subspace is Kähler.

Before proceeding a discussion of the moduli spaces, we briefly note some facts about the homology/cohomology groups of Calabi-Yau 3-folds. The groups are of prime importance to us here due to a one-to-one correspondence between the moduli and the elements of particular cohomology groups, which we'll shortly see are $H^{(2,1)}(Y)$ and $H^{(1,1)}(Y)$. First, the dimension of the $(p,q)^{\text{th}}$ Dolbeault cohomology group[9] is labeled by the hodge number $h^{p,q}$.

For Calabi-Yau d-folds $h^{(d,0)} = 1$. Taking $d = 3$ we label the sole member of $H^{(3,0)}(Y)$ as Ω, the holomorphic 3-form. Due to the (precise) $SU(d)$ holonomy we also have $h^{1,0} = 0$. The hodge star duality, complex conjugation duality and holomorphic duality for Calabi-Yau,

$$h^{p,q} = h^{3-p,3-q}, \quad h^{p,q} = h^{q,p}, \text{ and } \quad h^{0,q} = h^{0,3-q} \tag{1.2.11}$$

hold [24]. This leaves only two unspecified hodge numbers for a Calabi-Yau 3-fold, $h^{1,1,}$ and $h^{2,1}$. The relations among the hodge numbers are illustrated using the hodge

[9]The Dolbeault cohomology groups are the complex version/extension of the de Rham cohomology groups. The convention is to take the (p,q) Dolbeault cohomology group to be the set of (p,q)-forms that are $\bar{\partial}$ closed, with the equivalence relation $\omega \simeq \omega + \bar{\partial}\alpha$. However, the same analysis can be performed using ∂ closed forms and the analogous equivalence relation.

diamond, formed by arranging the hodge numbers as,

$$\begin{array}{ccccccc}
 & & & h^{3,3} & & & \\
 & & h^{3,2} & & h^{2,3} & & \\
 & h^{3,1} & & h^{2,2} & & h^{1,3} & \\
h^{3,0} & & h^{2,1} & & h^{1,2} & & h^{0,3} \\
 & h^{2,0} & & h^{1,1} & & h^{0,2} & \\
 & & h^{1,0} & & h^{0,1} & & \\
 & & & h^{0,0} & & &
\end{array} \tag{1.2.12}$$

For a Calabi-Yau the identities mentioned imply,

$$\begin{array}{ccccccc}
 & & & 1 & & & \\
 & & 0 & & 0 & & \\
 & 0 & & h^{1,1} & & 0 & \\
1 & & h^{2,1} & & h^{2,1} & & 1 \\
 & 0 & & h^{1,1} & & 0 & \\
 & & 0 & & 0 & & \\
 & & & 1 & & &
\end{array} \tag{1.2.13}$$

Also, note the number of nontrivial 2-cycles of the Calabi-Yau is $h^{1,1}$ and the number of nontrivial 3-cycles is $2(h^{2,1}+1)$. This follows from using the Hodge decomposition for Kähler manifolds which implies the complex order r de Rham cohomology group[10] consists of,

$$H^r(Y,\mathbb{C}) = \bigoplus_{p=0}^{r} H^{(p,q)}(Y) \tag{1.2.14}$$

followed by the Poincaré duality, see for e.g. [24].

Returning to our main objective — the parameter space of Calabi-Yau manifolds

[10]The group of complex r-forms that are d-closed modulo d-exact forms.

— recall that from Yau's theorem we know each manifold is uniquely specified by its Ricci-flat Kähler metric. So, begin with that of Calabi-Yau Y, labeling the components in real coordinates $\{x^i\}$ as g_{ij}. That Y is a Calabi-Yau means that when the complex coordinates $\{y^a\}_{a=1}^{n/2}$ defined in terms of $\{x^i\}_{i=1}^{n}$ which cast the complex metric as a hermitian metric are used[11] the Kähler form J this hermitian metric $g_{a\bar{b}}$ defines is closed. Label the complex structure that defines these canonical $\{y^a\}$ as $\mathcal{J}$.

We can smoothly deform Y into a nearby (a priori generic) manifold Y' by adding a real and symmetric perturbation δg_{ij} to g_{ij}, and taking the resulting g'_{ij} as the metric on Y'). We ask: of the variations that 1. maintain Ricci-flatness,

$$R^{(Y)}_{ij} \equiv R_{ij}(g, \partial g, \partial^2 g) = 0 \tag{1.2.15}$$

$$g_{ij} \to g'_{ij} \equiv g_{ij} + \delta g_{ij} \tag{1.2.16}$$

$$R^{(Y')}_{ij} \equiv R_{ij}(g + \delta g, \partial(g + \delta g), \partial^2(g + \delta g)) \tag{1.2.17}$$

$$= R^{(Y)}_{ij} + \underbrace{\mathcal{O}\left(\delta g, \partial \delta g, \partial^2 \delta g\right)}_{\substack{\delta g \text{ such that:} \\ \| \\ 0}} \tag{1.2.18}$$

what is the subset of variations for whom 2. there *still* exists a way to define complex coordinates in terms of $\{x^i\}$ such that the Kähler form J' is closed? Note, the only freedom we are allowing ourselves to check Kählerity after 1.2.18 is imposed is how the potentially new canonical coordinates $\{y'^a\}$ are defined in terms of the $\{x^i\}$, i.e. the ability to select a new complex structure $\mathcal{J}'$. No subsequent holomorphic changes of coordinates are allowed, as these would be changes of coordinates back on the real side as well, and we must not undo the Ricci-flatness of g'_{ij}. In light of Yau's theorem, the parameter space of this subset of variations δg_{ij} is the parameter space of Calabi-Yau smoothly connected to Y.

Setting the leading order terms in the perturbed Ricci-tensor in 1.2.18 to zero

[11] All complex manifolds admit a hermitian metric.

results in the Lichnerowicz equation for the metric variation,

$$\nabla^k \nabla_k \delta g_{ij} + 2R_i{}^{\ell}{}_j{}^{m} \delta g_{\ell m} = 0 \tag{1.2.19}$$

where ∇^k is the covariant derivative and the connection is the Levi-Civita connection. The solutions to this system of partial differential equations are organized in a useful fashion by working in Y's canonical complex coordinates $\{y'^a\}$, as the unperturbed Riemann tensor has many zero entries in these coordinates due to the Kählerity of Y. In general, a perturbation to the real metric alters the both mixed and pure entries in Y's hermitian metric. That is, the real variations are linear combinations of $\delta g_{a\bar{b}}$, δg_{ab}, and $\delta g_{\bar{a}\bar{b}}$.

We do however know the complex perturbations satisfy the relations

$$\delta g_{ab} = \delta g_{ba}, \quad \delta g_{a\bar{b}} = \delta g_{\bar{b}a}, \quad \overline{\delta g_{ab}} = \delta g_{\bar{a}\bar{b}}, \quad \text{and } \overline{\delta g_{\bar{a}b}} = \delta g_{a\bar{b}} \tag{1.2.20}$$

because of the fact that the variation in real coordinates is real-valued and symmetric (otherwise g'_{ij} wouldn't even be a metric on a manifold). Although the indices of the real variation in 1.2.19 are summed over, the equations involving variations of mixed type separate entirely from those involving those of pure type, due to the Kählerity of Y.

So we may consider the cases one at a time. It can be shown that deformations of Y that involve only mixed perturbations $\delta g_{a\bar{b}}$ are such that 1.2.19 is satisfied if and only if the $(1,1)$-form

$$i\delta g_{a\bar{b}}\ dy^a \wedge dy^{\bar{b}} \tag{1.2.21}$$

built from it is harmonic (note this form is also real since $\delta g_{a\bar{b}} = \overline{\delta g_{\bar{a}b}}$). Each cohomology class in $H^{(1,1)}(Y)$ has a harmonic representative[12]. There furthermore is a

[12]By the hodge decomposition theorem every $\bar{\partial}$ closed (p,q)-form α can be expressed as $\alpha = \omega + \bar{\partial}\beta$ where ω is harmonic. Hence each equivalence class in the Dolbeault cohomology group $H^{p,q}(Y)$ has

real harmonic representative because $\Delta = d^\dagger d = \partial^\dagger \partial + \bar{\partial}^\dagger \bar{\partial}$ so if $\Delta\omega = 0$ then $\bar{\omega}$ is also harmonic. Hence, each of the $h^{1,1}$ real harmonic forms defines an independent metric variation of mixed type that maintains Ricci-flatness.

Do these maintain Kählerity? Notice the perturbed metric $g_{a\bar{b}} + \delta g_{a\bar{b}}$ is still in canonical form (i.e. with the original choice of complex structure), simply because the pure components of the full metric still vanish. The new Kähler form J' differs from the original one J precisely by the harmonic form 1.2.21, which is closed. The real expansion coefficients of δJ in a basis of real 2-forms uniquely specifies each one of these Calabi-Yau,

$$J = v^A \, e_A, \quad v^A = \int_{D_{2,A}} J \tag{1.2.22}$$

where $A = 1, \ldots h^{1,1}$.

Sending $J \to J + \delta J$ corresponds to $v^A \to v^A + \delta v^A$. These real scalars are called Kähler moduli. They are the volumes of the 2-cycles $D_{2,A}$ dual to the basis forms e_A[13]. Finally, supersymmetry leads us to recognize that we ought to incorporate the real NSNS 2-form B into the definition by integrate the combination $B + iJ$ over the basis cycles. The reason is because this *complexified* Kähler form transforms under supersymmetric transformations, not J alone. The now complexified Kähler moduli w^A defined by,

$$w^A = \int_{D_{2,A}} B + iJ \tag{1.2.23}$$

have imaginary part equal to the 2-cycle volume. The contribution to w^A from B, which we'll label u^A, is referred to as an axion. This distinction will be discussed momentarily. In sum, the real scalars v^A parameterize all the Calabi-Yau obtained by smoothly deforming the Kähler class alone (leaving $\mathcal{J}$ unchanged).

Turning to deformations involving only metric variations of pure type, these can

a unique harmonic representative.

[13]The Poincaré dual of the 4-form obtained by taking the hodge dual of e_A.

similarly be shown to maintain Ricci-flatness if and only if

$$\Omega^{\bar{c}}{}_{ab}\ \delta g_{d\bar{c}}\ dy^a \wedge dy^b \wedge dy^{\bar{c}} \tag{1.2.24}$$

is harmonic [21], [22]. So variations of this sort are in one-to-one correspondence with the cohomology classes in $H^{(2,1)}(Y)$. Note however that the metric no longer takes canonical form in the coordinates $\{y^a\}$ because of the newly nonvanishing pure components. Instead, the coordinates which cast it as a hermitian metric (a priori, if they exist) are defined by a new complex structure $\mathcal{J}'$ which satisfies the hermiticity condition,

$$g'(v,w) = g'(\mathcal{J}'v, \mathcal{J}'w), \quad \forall\ v \text{ and } w \in T_pY' \tag{1.2.25}$$

where g' is the perturbed real metric.

The result is that there are indeed $h^{2,1}$ independent pure-type metric perturbations which correspond to deformations of $\mathcal{J}$. The moduli that parameterize these are defined in analogous manner as the v^A; namely as the expansion coefficients of 1.2.24 in a basis for $H^{(2,1)}(Y)$. In this case however the expansion coefficients, z^I, are complex. For instance, a pure anti-holomorphic perturbation is given by

$$\delta g_{\bar{a}\bar{b}} = -\frac{1}{\|\Omega\|^2}\ \overline{\Omega}_{\bar{a}}{}^{cd}\ \chi_{I,cd\bar{b}}\ \delta z^I \tag{1.2.26}$$

where $\|\Omega\|^2 \equiv \frac{1}{3!}\Omega_{abc}\overline{\Omega}^{abc}$ is constant, and the $\chi_{I,ab\bar{c}}$ are the components of the I^{th} basis element of $H^{(2,1)}(Y)$. I labels an equivalence class of $H^{(2,1)}(Y)$. Notice that unlike in the case of mixed type, the perturbed metric is no longer a hermitian metric. New complex coordinates need to be defined to cast the metric in canonical form. In other words, the change of variables that is required to cancel the newly introduced pure components of the metric is not holomorphic. This is precisely what it means to

change the complex structure. Indeed, smooth deformations of the complex structure are given by varying the z^I continuously.

The geometry of the moduli space can be ascertained writing the natural expression for the infinitesimal path interval ds^2 associated with a general deformation δg,

$$ds^2 = \frac{1}{2\mathcal{V}_0}\int_Y \sqrt{g}\; dx^6 g^{a\bar{b}}\; g^{c\bar{d}}\,[\delta g_{ac}\;\delta g_{\bar{b}\bar{d}}\; + (\delta g_{a\bar{d}}\;\delta g_{c\bar{b}} + \delta B_{a\bar{d}}\;\delta B_{c\bar{b}})\;] \tag{1.2.27}$$

and expressing the metric perturbations in terms of moduli variations, δu^A, δv^A and δz^I. The contribution from variations of pure type in 1.2.27 is,

$$-\frac{2i}{V\|\Omega\|^2}\;\delta z^I \delta z^{\bar{J}}\int_Y \chi_I \wedge \overline{\chi}_{\bar{J}} \tag{1.2.28}$$

This is the only contribution to the path length from the infinitesimal complex structure deformations. So we recognize the components of the metric on this subspace are given by,

$$G_{I\bar{J}} = -\frac{\int_Y \chi_I \wedge \overline{\chi}_{\bar{J}}}{\int_Y \Omega \wedge \overline{\Omega}} \tag{1.2.29}$$

where we've expressed the factor involving $\|\Omega\|^2$ and dimensionless volume V in 1.2.28 as an integral over the Calabi-Yau. The reason for doing this is that the integral in the numerator involving the χ_I can in fact be expressed in terms of the partial derivatives of the integral involving Ω, taken with respect to the complex structure parameters. Recall we are integrating over Calabi-Yau Y parameterized by the moduli, i.e. $Y = Y(z^1, \ldots, z^{h^{2,1}}, v^1, \ldots v^{h^{1,1}})$.

The crucial step is recognizing that a basis for $H^{(2,1)}(Y)$ can be generated via partial differentiation of the holomorphic 3-form with respect the z^I. In particular, differentiating with respect to the I^{th} modulus generates a $(2,1)$-form in the I^{th} cohomology class plus an I-dependent multiple of Ω,

$$\frac{\partial\Omega}{\partial z^I} = k_I\Omega + \chi_I \tag{1.2.30}$$

Ultimately we find,

$$G_{I\bar{J}} = -\frac{\partial}{\partial z^I}\frac{\partial}{\partial z^{\bar{J}}}\log\left(i\int_Y \Omega\wedge\overline{\Omega}\right). \tag{1.2.31}$$

This is very significant, as it means the space spanned by the complex structure moduli is itself Kähler, its Kähler potential given by

$$\mathcal{K}^{\text{cs}} = -\log\left(i\int_Y \Omega\wedge\overline{\Omega}\right). \tag{1.2.32}$$

A calculation, the technical details of this calculation can be found in [21], reveals the constant k_I in 1.2.28 as

$$k_I = -\partial_I\mathcal{K}^{\text{cs}}. \tag{1.2.33}$$

This motivates defining the operator $D_I := \partial_I + \mathcal{K}^{\text{cs}}_I$, since it produces a basis for $H^{(2,1)}(Y)$ when applied to Ω (with I running from 1 to $h^{2,1}$). This is the Kähler covariant derivative. Then, a basis for the entire 3$^{\text{rd}}$ de Rham cohomology group is given by

$$\left\{\Omega,\ D_1\Omega,\ldots,D_{h^{2,1}}\Omega\ ,\ D_{\bar{1}}\overline{\Omega}\ldots,\ D_{\bar{h}^{2,1}}\overline{\Omega},\ \overline{\Omega}\right\} \tag{1.2.34}$$

It is essentially just an expansion of a general 3-form $G_{(3)}$ (that maintains Poincaré invariance in the large dimensions) in this basis which turns 1.1.12 into the no scale $\mathcal{N}=1$ scalar potential. These steps are reviewed in chapter 4 section 4.1, following [14].

There is yet more structure. The Kähler potential 1.2.32 can itself be expressed in terms of a prepotential. This is can be understood as follows [25]. For Calabi-Yau, there exists of an integral and symplectic basis for the 3-forms of the cohomology group. Here the term integral means the Poincaré duals are true geometrical cycles (actual 3-dimensional submanifolds not merely objects defined formally as the duals of cohomology cycles).

Now, two 3-cycles intersect at points in a 6-dimensional manifold at points. "Sym-

plectic" means the basis' 3-cycles can be grouped into pairs; the members of each of the $h^{2,1}+1$ couples intersects one-another exactly once and no member of any other pair. The intersection numbers have multiplicity ± 1 because the cycles are oriented, and when organized into the elements defining a linear map from $H^{(3)}(Y) \times H^{(3)}(Y)$ to $\mathbb{Z}$

$$Q_{ij} = Q(D_{3,i}, D_{3,j}) = \langle D_{3,i} \smile D_{3,i}[Y] \rangle \tag{1.2.35}$$

form a symplectic matrix Q. This is of course viewed equally well as a map from two copies of the (3)-cohomology groups,

$$\tilde{Q}_{ij} = \tilde{Q}(\alpha_i, \alpha_j) = \int_Y \alpha_i \wedge \alpha_j, \quad \tilde{Q}_{ij} = Q_{ij}. \tag{1.2.36}$$

In such a basis, the Kähler potential for the complex structure moduli 1.2.32 takes the form,

$$\mathcal{K}^{\text{cs}}(z) = -\log\left(-i\,\Pi^\dagger\, Q\,\Pi\right) \tag{1.2.37}$$

where the Π is a vector whose $2(h^{2,1}+1)$ components are holomorphic functions $\Pi_i(z)$ defined as the integrals of the holomorphic 3-form Ω over the symplectic basis 3-cycles.

The Kähler moduli space similarly is also Kähler, in particular with its Kähler potential given by,

$$\mathcal{K}^{\text{kä}} = -\log\left(\frac{4}{3}\int_Y J^3\right) = -2\log\left(\mathcal{V}_0\right) \tag{1.2.38}$$

$$= -2\log\left(\frac{1}{6} D_{ABC}\; v^A\, v^B\, v^C\right) \tag{1.2.39}$$

where the $\mathcal{V}_0$ is the volume of the Calabi-Yau in units of ℓ_{s}^6, and D_{ABC} are the triple intersection numbers. The dramatic simplification of the 6-volume to an expression involving only the intersection numbers (topological information) and 2-cycle volumes is a result of Kählerity.

The topological information contained in the two hodge numbers $h^{1,1}$ and $h^{2,1}$ together with the list of triple intersection numbers uniquely identifies each smooth family of Calabi-Yau. Different constructions can in fact give rise to the same family Calabi-Yau. It is an interesting question whether there are infinitely many Calabi-Yau 3-folds, that is valid sets of hodge and triple intersection numbers allowed. The accumulation of known Calabi-Yau 3-folds in bounded regions of the (topological) parameter space is notable, but it is also possible that the known methods of constructing Calabi-Yau are incomplete.

The independence of 1.2.39 from the B-axions, and consequently also that of the Kähler metric components is significant. Axions are scalars that enter an effective theory's Lagrangian only via kinetic terms which can be cast in canonical form. There is absolutely no dependence of the potential on axions, *which persists through the perturbative level*. Only non-perturbative effects, for example from Dp-brane instantons, break this continuous shift symmetry.

The special symmetry of these scalar degrees of freedom at the perturbative level arises due to a specific symmetry present in the higher-dimensional theory. Anytime a p-form potential enters the supergravity action, axions associated with it will be present in the lower-dimensional theory. Note, this is *not* the higher-form version of Maxwell theory which involves not the 1-form potential A but its filed strength $F = dA$. It is essential that the potential itself enter the action for the continuous shift symmetry to result.

For instance, in the IIb supergravity action the NSNS 2-form enters in the self-dual 5-form

$$\tilde{F_5} := F_5 - \frac{1}{2} C_2 \wedge H_3 + \frac{1}{2} B_2 \wedge F_3 \tag{1.2.40}$$

where the RR and NSNS p-form field strengths are defined as the exterior derivatives of their $p-1$ form potentials $F_p := dC_{p-1}$ and $H_p := dB_{p-1}$, and we've included subscripts for clarity. The NSNS 2-form in the last term of 1.2.40 appears in the

supergravity action due to the contribution,

$$-\frac{2\pi}{\ell_{\rm s}^8}\frac{1}{2}\tilde{F}_5 \wedge *\tilde{F}_5 \subset S_{IIb,(10)}. \tag{1.2.41}$$

Axions are a generic feature of string theory. Once non-perturbative corrections to the superpotential are included, the resulting effective potential has interesting dependence on the axions. Essentially, these corrections have the qualitative form,

$$W_{\rm np} = Ae^{icT} \tag{1.2.42}$$

where c and A are constants and T represents a modulus like the complefixied Kähler moduli, having the form "axion plus i times volume." We are being general because other cycles can also give rise to axions, for example 4-cycles in the case of IIb. The result is an overall factor that is exponentially suppressed in the modulus' associated cycle's volume, and an oscillatory dependence on the axion. In certain limits this can percolate through the terms of the scalar potential and manifest as contributions periodic in the axions.

The properties of such effective theories are particularly relevant to cosmology, and axions are often studied as potential candidates for the inflaton. In recent work with collaborators T. Bachlechner, O. Janssen and M. Kleban [26] we present a systematic procedure involving lattice reduction techniques to study random axion landscapes. We find that these theories not only accommodate a small CC but, also generically have both inflaton and dark matter candidates. We identify a mechanism that generates aligned "gentle slopes" along which slow-roll inflation can take place. The enhancement of the invariant field space distance along these gentle slope directions occurs due to the special combination of random charge matrices and large field space dimension.

1.3 Cast of Moduli

It is useful to summarize the cast of moduli of the compactified IIb theory to give a sense of scope. To distinguish between axionic and "size" components of certain moduli we'll count the real degrees of freedom.

We've seen there are a total of $2h^{2,1}$ associated with complex structure deformations (the z^I), $h^{1,1}$ "size" moduli associated with 2-cycles (the v^A), $h^{1,1}$ B-axions (the u^A), and the dilaton field ϕ. There are also C_2 and C_4 axions, associated with the Calabi-Yau's nontrivial 2-cycles and 4-cycles. Additionally, moduli that parameterize the locations of dynamical stringy objects, in this case D3-branes, also enter the effective description. Since the Calabi-Yau is 6-dimensional there are six real scalars for each D3-brane, for a total of $6N_{\rm D3}$. The effect of orientifolding is to break the otherwise equal hodge numbers associated with axion and "size" moduli, the details of which can be found in [7].

For comprehensive reviews of type II compactifications, including discussions of the obstacles to and consequently strategies for stabilizing moduli to yield de Sitter vacua, see for e.g. [7] (which emphasizes IIb and the geometric formulation computations often permit in the F-theory context), as well as [23], [27], [28]. Systematic approaches to compactification of heterotic $E_8 \times E_8$ with stabilization of all complex structure moduli can be found in the works [29], [30], [31]. An overview of string cosmology, which discusses axions for instance, is [32].

Explicit examples of moduli stabilization include [33], [34]. The distributions and statistics of supersymmetric and nonsupersymmetric vacua by taking the continuum approximation of flux integers were analyzed in [35] and [36], respectively.

Finally, different randomized approaches are often employed to study effect of large field space dimension in a tractable setting, as explicit computations from actual string compactifications often are not feasible. Calculations of the tunneling rates for instance can be carried through, and potentially provide useful intuition.

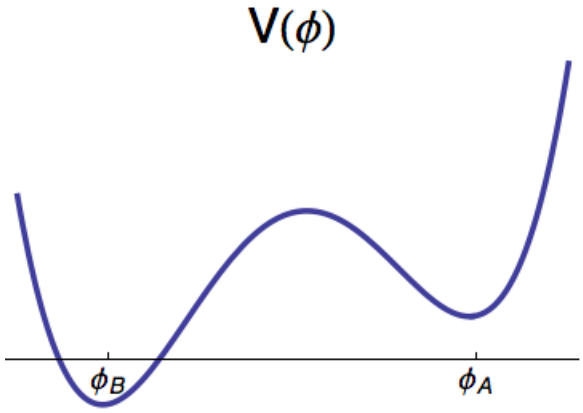

Figure 1.2: Double-well potential. A field configuration that is homogeneous with field value ϕ_A decays into the true vacuum ϕ_B via the nucleation of expanding spherical bubbles, according the Coleman-De Luccia decay rate $\Gamma/V = Ae^{-B/\hbar}(1 + \mathcal{O}(\hbar))$. Since ϕ_A is not arbitrarily long lived we refer to it as a false vacuum.

Results vary depending on the construction. Landscapes with random potentials and superpotentials designed by drawing independent identically distributed Taylor coefficients were studied in [37], while examples of the Random Matrix Theory/Wigner ensemble approach include [38]. Landscapes with some of the additional structure of supergravity theories built in were studied in [39].

1.4 Vacuum Transitions

Field configurations that are spatially homogeneous and locally minimize the energy density are stable at the classical level. Whether or not the absolute minimum energy density of the theory is attained is irrelevant in determining stability. A basic result of QFT however is that only quantum states with field expectation values that globally minimize the potential are arbitrarily long lived. The quantum state underlying a homogeneous field configuration that only locally minimizes the energy density is *metastable* — quantum fluctuations inevitably cause it to decay.

Loosely speaking, quantum fluctuations in a given spatial volume can violate energy conservation and land the field value(s) there in the basin of attraction of a

new local minimum of the potential, and particularly one of lower energy density. Just as a quantum mechanical system in its ground state can be observed at a classically forbidden location, the field value in a given spatial volume can tunnel from a false vacuum value through a potential barrier to a vacuum of lower energy.

Coleman draws a very illuminating analogy between vacuum decay in QFT and phase transitions in ordinary fluids, for instance from the superheated liquid phase to the vapor phase [1]. The superheated liquid phase is not arbitrarily long lived, despite the fact that it corresponds to a local minimum of the free energy (as a function of density). Bubbles of the vapor phase with various sizes appear within the fluid due to thermodynamic fluctuations. Bubbles smaller than some critical size collapse due to their surface tension. Though large bubbles are of course less likely to appear than small ones, bubbles that are larger than the critical size *expand* because their gain in volume energy overcomes their loss to surface energy. These large bubbles mediate the phase transition. Similarly, quantum fluctuations cause expanding regions — bubbles — of lower energy density vacuum to appear in the initially homogeneous false vacuum field configuration. The false vacuum decays away just as the superheated liquid boils away.

The quantitative analysis of this process in scalar field theories was first laid out in [1], [40], [41]. This work involves the field theory extension of the *semiclassical* analysis of barrier tunneling in single particle quantum mechanics in several spatial dimensions, wherein a particle sits at the bottom of a potential well until it the instant it tunnels. At this instant it appears on the other side of the barrier with zero kinetic energy and thereafter propagates classically (according to the gradient of the potential). A decay rate and the location where the particle exits the barrier are computed by using the WKB approximation. For the field theory the decay rate has units of inverse four volume. Similarly the field is said to sit in the false vacuum configuration $\phi = \phi_A$ until the it changes instantaneously to the tunneled configuration with zero

kinetic energy $\dot{\phi} = 0$, after which it evolves classically. The field configuration upon tunneling is analogous to the location at which particle exits barrier. Just as in the semiclassical approximation the classical energy of the quantum mechanics particle is the same before and after tunneling, the tunneled field configuration conserves the classical energy.

Here I highlight some of the key results. Note that $V(\phi_A)$ is chosen to be zero in this analysis. This can be relaxed, and I will point out how to do so in the context of the Thin Wall Approximation at the end of this section. The decay rate takes the form,

$$\Gamma/V = Ae^{-B/\hbar}(1 + \mathcal{O}(\hbar)) \tag{1.4.1}$$

and is computed using the WKB approximation. This leads to the identification of B with the action in the Euclidean theory (theory with imaginary time coordinate τ) evaluated at a particularly special extremum of the Euclidean action, known as the O(4) invariant "bounce."

The Euclidean action for the scalar field theory is

$$S_E = \int d\tau d^3x \left(\frac{1}{2} \left(\frac{\partial \phi}{\partial \tau} \right)^2 + \frac{1}{2} |\vec{\nabla}\phi|^2 + V(\phi) \right). \tag{1.4.2}$$

When O(4) symmetry is imposed the Euler-Lagrange equation becomes an ODE in $\rho = \sqrt{\tau^2 + |\vec{x}|^2}$,

$$\frac{d^2\phi}{d\rho^2} + \frac{3}{\rho}\frac{d\phi}{d\rho} = \frac{\partial V}{\partial \phi} \tag{1.4.3}$$

Taking the time at which the tunneling event occurs as $t = 0$, the boundary conditions for the bounce are,

$$\lim_{\rho \to \infty} \phi(\rho) = \phi_A \tag{1.4.4}$$

$$\frac{d\phi}{d\rho}(0) = 0 \tag{1.4.5}$$

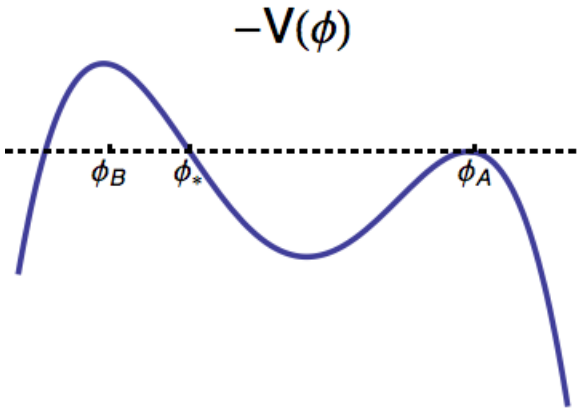

Figure 1.3: Inverted potential relevant for identifying the bounce solution.

The first of these ensures that decay be localized in space at finite time — the false vacuum is not affected at spatial infinity and in the infinite past. Requiring that the field tunnel with zero kinetic energy gives the second condition. It is useful to define an auxiliary system in order to deduce the solutions to this boundary value problem. If we associate ϕ with the position of a classical particle moving in one dimension and ρ with time, then the above system describes the damped motion of a particle in the *inverted* potential, $-V(\phi)$. The particle is released at $\rho = 0$ with zero kinetic energy somewhere between ϕ_B and ϕ_A, and rolls towards ϕ_A, reaching it in the infinite future $\rho \to \infty$. If there were no damping the particle would start off at the same energy level as $-V(\phi_A)$, indicated by ϕ_* in figure 1.3. Clearly the damped particle stops short of ϕ_A if released from ϕ_*, and so must be released further up the inverted potential closer to ϕ_B in order to account for the loss to dissipation and reach ϕ_A in the infinite future. There is a unique value between ϕ_B and ϕ_* such that this occurs.

Since 1.4.3 is invariant under $\rho \to -\rho$ an even solution to problem defined by 1.4.3, 1.4.4, and 1.4.5 can be defined for $\rho \in (-\infty, \infty)$. We call this solution the "bounce", because it describes the auxiliary particle coming in from ϕ_A in the infinite past, coming to rest somewhere in between ϕ_B and ϕ_* at $\rho = 0$, and retreating toward ϕ_A, approaching it in the infinite future. Let us denote this solution $\phi_{\text{bounce}}(\rho)$. Then the coefficient in the decay rate, B, is the Euclidean action of the (full) bounce.

In the semiclassical treatment the field configuration changes at an instant ($t = 0$) from $\phi(x) = \phi_A$ to the configuration obtained by evaluating the bounce at $\tau = 0$, namely $\phi_{\text{bounce}}(\rho = |\vec{x}|)$. This is a spherically symmetric configuration. The field value in the center is the value at which the auxiliary particle bounces, $\phi_{\text{bounce}}(0)$. The configuration's radial profile changes monotonically from $\phi_{\text{bounce}}(0)$ to the parent vacuum value, ϕ_A, as the distance from the center increases. In the semiclassical approximation the evolution of the underlying quantum state is captured by evolving this tunneled configuration by the classical equations of motion in Minkowski space. The field value in the center of the tunneled configuration (which recall is in between ϕ_* and ϕ_B) is in the basin of attraction of ϕ_B in the original potential $V(\phi)$, and so it relaxes to ϕ_B. In fact, the full classical evolution of the tunneled field configuration can be obtained from the bounce solution alone.

The bounce solves the imaginary time version of the classical equations of motion in Minkowski space. Consequently the evolution of the bubble subsequent to the instant it appears is simply given by the analytic continuation of the bounce solution from imaginary time to real time. So we can define the bubble solution by $\phi_{\text{bubble}}(t, \vec{x}) = \phi_{\text{bounce}}(\sqrt{|\vec{x}|^2 - t^2})$. Though in general we don't have an analytic expression for the bounce, the qualitative features of its analytic continuation can nonetheless be gleaned.

The case of nearly degenerate bubble and parent vacua helps us with this, so we review the approximations that can be made in this limit. Let us denote the small difference in energy densities by $V(\phi_B) - V(\phi_A) = -\epsilon$. Small ϵ has the effect of pushing ϕ_* in figure 1.3 towards ϕ_B, and so the place where the auxiliary particle bounces closer to ϕ_B. This means that the extra energy the auxiliary particle has when the bounce occurs in (order to account for the loss to damping) must be small.

More precisely

$$-V(\phi_B) > -V(\phi_{\text{bounce}}(0)) > -V(\phi_A) \tag{1.4.6}$$

$$\Delta E_{\text{damping, aux}} = -V(\phi_{\text{bounce}}(0)) + V(\phi_A) \tag{1.4.7}$$

$$\epsilon = V(\phi_A) - V(\phi_B) > \Delta E_{\text{damping, aux}} > 0 \tag{1.4.8}$$

This means that $\frac{d\phi}{d\rho}$ must stay small until the damping coefficient, $\frac{3}{\rho}$ is small, i.e. large ρ, in order to keep the net loss to dissipation less than ϵ. Putting this together, the auxiliary particle is released near ϕ_B at $\rho = 0$, stays there until very large $\rho \approx R$, at which point it rolls quickly and approximately undamped through the inverted potential and approaches ϕ_A asymptotically. When $\rho \approx R$ the bounce solution is well described by the solution to the undamped problem, which itself happens to be the definition of a 1-dimensional soliton that interpolates between ϕ_B and ϕ_A (in the degenerate theory).

In particular the 1-dimensional soliton, which I shall denote $f(x)$ is defined by the solution to,

$$\frac{d^2 f}{dx^2} = \left.\frac{\partial V}{\partial \phi}\right|_{\phi = f(x)} \tag{1.4.9}$$

$$\lim_{x \to -\infty} f(x) = \phi_B \tag{1.4.10}$$

$$\lim_{x \to \infty} f(x) = \phi_A \tag{1.4.11}$$

Furthermore, let us choose to the center is soliton about $x = 0$. Now let us approxi-

mate the bounce by,

$$\phi_{\text{bounce}}(\rho) \approx \phi_B,\ \rho \ll R \tag{1.4.12}$$

$$\phi_{\text{bounce}}(\rho) \approx f(\rho - R),\ \rho \approx R \tag{1.4.13}$$

$$\phi_{\text{bounce}}(\rho) \approx \phi_A,\ \rho \gg R \tag{1.4.14}$$

determine the value of R, and the precise condition under which the approximation is valid. This approximation to the bounce describes a large 4-dimensional spherical bubble of ϕ_B surrounded by a sea of ϕ_A, with a spherical boundary separating the two. The value of R is obtained by computing the Euclidean action as a function of R, and demanding that it be extremized (since recal the actual bounce solves $\delta S_E = 0$). The Euclidean action of an O(4) invariant function (expressed in spherical coordinates and after integrating out the angular piece) is,

$$S_E = 2\pi^2 \int_0^\infty \rho^3 d\rho \left[\frac{1}{2} \left(\frac{d\phi}{d\rho} \right)^2 + V(\phi) \right] \tag{1.4.15}$$

Applying 1.4.12 we have

$$2\pi^2 \int_0^R \rho^3 d\rho \left[\frac{1}{2} \left(\frac{d\phi}{d\rho} \right)^2 + V(\phi) \right] \approx 2\pi^2(-\epsilon) \int 0^R \rho^3 d\rho \tag{1.4.16}$$

$$= -2\pi^2 \epsilon \frac{R^4}{4} \tag{1.4.17}$$

In so far as the width of the 1-dimensional soliton is small, and condition we will formulate momentarily, the contribution to the Euclidean action across the boundary can be approximated by taking ρ^3 as constant and equal to R^3. This yields, a contribution of $2\pi^2 R^3 S_1$ to the Euclidean action, where S_1 is the 1-dimensional action of the soliton,

$$S_1 = \int dx \left[\frac{1}{2} \left(\frac{df}{dx} \right)^2 + \tilde{V}(f(x)) \right] \tag{1.4.18}$$

where $\tilde{V}$ is the potential of the exactly degenerate theory.

Lastly, note that outside the boundary the contribution to the Euclidean action is zero because $V(\phi_A) = 0$. Putting everything together we have,

$$S_E = -\frac{1}{2}\pi^2 R^4 \epsilon + \pi^2 R^3 S_1 \tag{1.4.19}$$

and so

$$\frac{dS_E}{dR} = 0 = 2\pi^2 \left(-\epsilon R^3 + 3R^2 S_1\right). \tag{1.4.20}$$

Thus, $R = 3S_1/\epsilon$. The approximation is valid only if the width of the 1-dimensional soliton is small compared to this value. Also note that the width of the 1-dimensional soliton is affected by the height and width of the potential barrier between ϕ_A and ϕ_B, not by ϵ. Tall and/or wide barriers yield thin solitons. Additionally not that if $V(\phi_A) \neq 0$ then R is simply given by,

$$R = \frac{3S_1}{V(\phi_A) - V(\phi_B)} \tag{1.4.21}$$

1.5 Possibility of an Emergent Description

The work herein has been motivated by the desire to understand primordial dynamics in the context of string compactifications. Broadly speaking, we would like to know which field configurations a once roiling sea of a richly varied expanding bubble vacua settles predominantly into at late time. When faced with the notoriously complicated models that give rise to this scenario — flux compactification of string/M/F theory which typically involve large numbers of degrees of freedom, for example the numerous moduli parameterizing a Calabi-Yau compactification — one may be daunted.

However, the complexity present in such descriptions is not necessarily fatal. In fact, quite the opposite may be the case. As often occurs in physical systems with

many degrees of freedom, the system's dynamics may give way to simple description in terms of emergent parameters. I would like to investigate whether simple rules can be used to identify vacuum solutions that are stable attractors of the theory, i.e. to obtain the late-time demographic data of a multiverse governed by string theory.

To that end we ought to identify the processes that populate and depart vacua. Clearly these include the quantum phenomenon of vacuum decay, Coleman-De Luccia tunneling in the case of scalar degrees of freedom described semi-classically. The relevant processes also include the classical evolution of vacuum bubbles following their nucleation. Bubbles created in a parent vacuum whose cosmological constant is sufficiently large with respect to their own will remain causally disconnected from one another; the space between them swells faster than their expanding walls diminish it. The parent *inflates eternally* keeping the bubbles always outside one another's cosmic horizon.

On the other hand, a bubble for whom this difference in energy densities is sufficiently small will inevitably encounter other expanding bubbles. It is thus important to understand the outcome of bubble collisions in addition to (quantum) decay rates, specifically what the late time field configuration is in the collision region. Furthermore, because the wall of a single bubble accelerates outward reaching relativistic speeds in time of the order of the bubble's initial radius, the limit of ultrarelativistic impact velocity is especially relevant.

This document consists of a description of the progress we've made developing this emergent picture. In an effort to give the reader flexibility we've described each project in self-contained chapters. We begin with two papers that focused on collisions in scalar field theory, specifically their limiting behavior in the ultrarelativistic regime. One finds that the nonlinear interaction between incoming bubble walls is suppressed due to their tremendous Lorentz contraction. As a result the wall profiles effectively pass through one another; they merely linearly superimpose. This is

known as the "free passage" approximation. In chapter 2 section 2.1 we show how this simple behavior can result in the production of an expanding patch of offspring vacuum upon collision. Our two projects investigated the robustness of this mechanism and determined the mathematical generalization of the free passage procedure to theories with nontrivial field space curvature, i.e. those with noncanonical kinetic terms (chapter 3).

This latter result is cast elegantly in field space; amounting to the mutual parallel transport of the tangent vector fields to the two soliton curves connecting the two colliding bubble vacua with the parent they were initially nucleated in. Understanding the role of curvature is crucial because it is a common feature of the effective theories retrieved upon flux compactification (for example, Calabi-Yau moduli space has Kähler geometry often rich with branch cuts and curvature singularities near vacuum locations).

Our third project focused instead on the phenomenological features of vacua in the landscape, as opposed to the capacity of collisions to move one around in moduli space. We took the case of compactification of type IIb supergravity on the mirror quintic in the limit of large volume, and obtained a random sample of near conifold no scale vacua. We calculated the masses and coupling coefficients to quartic order for the random collection of effective field theories obtained by expanding the scalar potential about these minima. Indeed a simple description emerged due to the mirror quintic complex structure's moduli space geometry. The pronounced hierarchy among these physical constants that we found was explained analytically in terms of the limiting behavior of the Yukawa coupling for the mirror quintic near the conifold point.

Chapter 2

Collisions in Flat Field Space

We began in [42] by using the simplest of these models, ones involving a single scalar field, and focused on the detailed dynamics of bubble collisions. Earlier work [43], [44] revealed the dramatic simplification that emerges at ultrarelativistic impact velocity mentioned in the introduction — free passage — in which the two colliding bubble walls merely superpose. The higher the Lorentz factor of the incoming bubble walls the better the field configuration in the collision region is approximated by the parent configuration plus the change across each wall. We can immediately see how this can provide a (classical) means for transitioning between vacua, and so is consequential to our project. Consider the simple case of colliding two identical bubbles with field configuration ϕ_B nucleated in parent ϕ_A. Free passage amounts to sending the field in the region between the bubbles from the pre-collision value, ϕ_A, to $\phi_A + 2\Delta = \phi_A + 2(\phi_B - \phi_A) = 2\phi_B - \phi_A$, post-collision. Transitions are possible because the field value in the collision region, $2\phi_B - \phi_A$, could very well be in the basin of attraction of an entirely different vacuum — neither bubble nor parent.

These results were found in models whose potentials enjoyed an nearly exact symmetry about the bubble vacuum, and so had a new vacuum, we'll call ϕ_C, located extremely close to the free passage kicked location, $2\phi_B - \phi_A$. Generically minima are not nearly equally spaced, so a natural issue to investigate was one of robustness. We sought to determine whether collisions for whom free passage landed the field inside ϕ_C's basin of attraction always successfully spawned a bubble of ϕ_C, or instead if there was a minimum distance the kicked field value $2\phi_B - \phi_A$ had to reach inside

the basin of attraction to ensure success.

Free passage preserves the shapes of the spatial profiles of the walls of the two bubbles collided, merely shifting each profile by an overall constant amount. For generic potentials these shifted profiles are not anything particularly special. So, although the free passage obtained post-collision field configuration might no doubt consist of a widening expanse of field value in the basin of attraction of ϕ_C, it's outgoing walls could be so different from the relevant stable profiles that they ultimately collapse. To address this question of the robustness of transitions mediated by free passage we followed the lead of [44] and considered the toy version of bubble collisions valid in the case of nearly degenerate parent and bubble vacua — that of soliton–anti-soliton collisions in $1 + 1$ dimensions.

By means of heuristic reasoning we identified a mechanism that could thwart transitions to ϕ_C despite having landed in it's basin of attraction through a fully realized free passage kick. This mechanism was formulated in terms of the growth of an unstable mode, whose ability to destroy transitions depended on a competition of time scales. This competition, expressed as an inequality, involved a free parameter we obtained numerically. Although such "failures to transition" via the instability we predicted heuristically were borne out by the numerics, they were rare, in a precise sense. The value of the aforementioned parameter is a threshold on how large the magnitude of the potential's ratio of second to first derivatives must be at the free passage kicked field value in order for "failure" to be possible. The fact that this parameter turned out to be large means that, at least in the case of standard polynomial potentials, the mode's ability to hinder transitions is only relevant when free passage lands the field very close (but of course over) the barrier between ϕ_B and ϕ_C. The proximity needed to the peak of the barrier to sufficiently excite the mode in turn drastically limits the allowed distances between parent and bubble vacua. So,

for usual polynomial potentials we deemed this behavior finely tuned[1].

With this first paper providing further evidence that collisions can provide an efficient means for transitioning between vacua (even those that are widely separate), the natural next question was to determine how this process manifests in toy models one step closer to those inhabiting the landscape — namely, models with a nontrivial field space curvature, typical of Calabi-Yau compactifications. The generalization of free passage to *flat* multifield theories (i.e. those with canonical kinetic terms) is straightforward. The equations and analyses from the single scalar case hold component-wise, and so the field in the collision region follows the straight line trajectory in field space from the parent location ϕ_A^i to $\phi_A^i + \Delta^i + \tilde{\Delta}^i$, where the deltas are now the displacements between the parent and bubble vacuum locations.

2.1 Background: Free Passage

Recent works [43], [44], [45], [46] indicate that ultra-relativistic bubble collisions provide a mechanism for efficiently moving between vacua. Generally speaking, an accurate description of the collision between two bubbles embedded in a parent false vacuum requires using the full nonlinear equations of motion. But the ultra-relativistic limit offers a great simplification, as the nonlinearities become subdominant [43], and so the solution is given by superposing two single bubble solutions. This is the free passage approximation.

Qualitatively, free passage is accurate because in the large Lorentz factor limit, the kinetic energy dominates the potential up until and for short time after the collision. The reason is that before the collision, both spatial and time derivatives of the field in the walls are large, but $\partial V/\partial\phi \sim 0$ everywhere. And as the walls become ever more Lorentz contracted the amount of time it takes for the walls to pass through

[1] An interesting exception to this judgement of non-genericity we touched upon briefly in the paper, however, is when the barrier between ϕ_B and ϕ_C is exponentially flat.

each other diminishes, and $\partial V/\partial\phi$ is not large enough to produce an acceleration great enough to significantly alter the field's free evolution during the collision, and so the walls simply superimpose and pass through each other.

More specifically, a collision is sufficiently relativistic for the free passage approximation to be valid if the Lorentz factor of the walls measured by an observer in the rest frame of the collision satisfies two inequalities [43], [44]. One of these comes from energy conservation, and involves the ratio of the heights of the barriers between the relevant vacua. The second condition comes from ensuring that the walls make it past each other before deviations from the homogeneous solution have time to grow. This latter condition is formulated in terms of the slope of the potential at the kicked field value (the field value just after the bubble walls collide), and the rest width of the solitons. In both of these minimum-Lorentz-factor-conditions, there are overall dissipation coefficients which have yet to be related to parameters in the theory.

The authors of [43] claim that after free passage, the field in the collision region rolls to the minimum of the basin of attraction to which it was propelled via the free passage kick. If the kicked field value happens to be in the basin of attraction of a new lower energy density vacuum, then the field in the collision region rolls to the new local minimum, exhibiting a coherent transformation to a new expanding bubble vacuum.

It is worth noting, however, that the specific models considered in [43], [44] respect various non-generic symmetries which may be responsible, in part, for the clean transition to the new vacuum. Namely, the models considered involve a potential with three nearly equidistant minima, which ensures that the free passage collision between two "middle" vacuum bubbles propels the field almost exactly to a new vacuum value. Moreover, the potential studied was (nearly) symmetric about the bubble vacuum. Which raises the natural question: What is the post-free passage dynamics for a more generic potential? When the simplifications/symmetries noted are no longer present,

does the field continue to roll to the local minimum of the basin of attraction it lands in via free passage?

To study this, we follow the approach taken by the authors in [44], and consider soliton-anti soliton collisions in $1+1$ dimensions, with more generic potentials. We invoke the thin wall approximation, which is valid when the two neighboring minima between which a bubble wall interpolates are nearly degenerate. In this case, the initial solitons are expressed as

$$\Box\phi = -\frac{\partial V}{\partial \phi} \tag{2.1.1}$$

$$\phi(0,\vec{x}) = f(|\vec{x}| - R) \tag{2.1.2}$$

$$\dot{\phi}(0,\vec{x}) = 0 \tag{2.1.3}$$

where $f(r)$ is the soliton associated with the degenerate potential, and the initial bubble radius is dependent on the potential — in particular three times the 1-dimensional soliton's action divided by the difference in energy densities of the bubble and parent vacuum. Hence, for large R the collision of two bubbles (nucleated sufficiently far apart that their walls reach relativistic speeds before colliding) looks effectively like the collision of domain walls. So, the collision of a soliton and anti-soliton in $1+1$ dimensions, each boosted to some constant relativistic speed, u, is a relevant problem to consider. The initial value problem is as follows

$$\begin{aligned}
&\frac{\partial^2\phi}{\partial t^2} - \frac{\partial^2\phi}{\partial x^2} = -\frac{\partial V}{\partial \phi} \\
&\lim_{t\to-\infty} \phi(t,x) = f(\gamma(x-ut)) + f(-\gamma(x+ut)) - \phi_A \\
&\lim_{t\to-\infty} \dot{\phi}(t,x) = -\gamma u\left(f'(\gamma(x-ut)) + f'(\gamma(x-ut))\right)
\end{aligned} \tag{2.1.4}$$

where γ is the Lorentz factor, the potential, V, has degenerate minima ϕ_A, and ϕ_B, and the soliton $f(x)$ approaches ϕ_B as $x \to -\infty$, and ϕ_A as $x \to \infty$. To simplify

notation in the following section, we now label the left moving and right moving solitons as follows,

$$f_{\mathrm{R}}(t,x) = f(\gamma(x-ut)) \tag{2.1.5}$$

$$f_{\mathrm{L}}(t,x) = f(-\gamma(x+ut)) \tag{2.1.6}$$

and define the free passage solution,

$$\phi_{\mathrm{FP}}(t,x) = f_{\mathrm{R}}(t,x) + f_{\mathrm{L}}(t,x) + \phi_A \tag{2.1.7}$$

Lastly, we note the the field in the region in between the walls before the collision, which is approximately in ϕ_A, is shifted by the sum of the changes in field values across each of the walls, here simply $\delta\phi = 2(\phi_B - \phi_A)$. This field deviation is the mathematical form of the free passage kick.

Let's now turn to the post-free passage field dynamics.

2.2 Heuristic Analysis

To study the classical evolution of the system after the free passage kick, we write the field as

$$\phi(t,x) = \phi_{\mathrm{FP}}(t,x) + \sigma(t,x). \tag{2.2.1}$$

Note that after the collision, ϕ_{FP} takes on the value $2\phi_B - \phi_A$ within the collision region and ϕ_A outside of it, and so all the subsequent dynamics are encoded in σ. Substituting this form into the original equation of motion for ϕ yields

$$\Box\sigma = \left.\frac{\partial V}{\partial\phi}\right|_{\phi_{\mathrm{FP}}+\sigma} - \left.\frac{\partial V}{\partial\phi}\right|_{f_{\mathrm{R}}} - \left.\frac{\partial V}{\partial\phi}\right|_{f_{\mathrm{L}}}. \tag{2.2.2}$$

Shortly after the collision σ remains small and so we expand to obtain

$$\Box\sigma = \left(\left.\frac{\partial V}{\partial \phi}\right|_{\phi_{\rm FP}} - \left.\frac{\partial V}{\partial \phi}\right|_{f_{\rm R}} - \left.\frac{\partial V}{\partial \phi}\right|_{f_{\rm L}} \right) + \left.\frac{\partial^2 V}{\partial \phi^2}\right|_{\phi_{\rm FP}} \sigma + \mathcal{O}(\sigma^2). \tag{2.2.3}$$

By dropping the term linear in σ we find that the field in the collision region is driven by the term

$$\left.\frac{\partial V}{\partial \phi}\right|_{\phi_{\rm FP}}. \tag{2.2.4}$$

Note that we have dropped the other two zeroth order terms appearing in equation (2.2.3) since they evaluate to zero within the collision region. The field dynamics is then driven by the slope of the potential at $2\phi_B - \phi_A$. During the bubble collision, sufficiently high relative wall velocities ensure that the resulting field evolution will be much smaller than the free passage kick. After the bubble collision, the natural expectation is that if the field falls in the basin of attraction of another vacuum, the field will subsequently roll to it. But this expectation relies on dropping the term linear in sigma, and while σ may start out small, it can quickly grow[2]. We will focus on cases in which a growing σ can significantly alter the post collision evolution. Indeed, we will see that there are cases in which the term linear in σ drives the field back toward ϕ_B thereby undoing the work of free passage.

To motivate this result, and to assess its genericity, let's consider the relative strength of the two lowest order terms in σ.

The First Order Term

Here we isolate the effect of the term linear in σ by dropping the zeroth order term in equation (2.2.3) and considering the following equation of motion

$$-\ddot{\sigma} = -\frac{\partial^2 \sigma}{\partial x^2} + \left.\frac{\partial^2 V}{\partial \phi^2}\right|_{\phi_{\rm FP}} \sigma. \tag{2.2.5}$$

[2]This is of course not true when $2\phi_B - \phi_A$ happens to be near a local minimum.

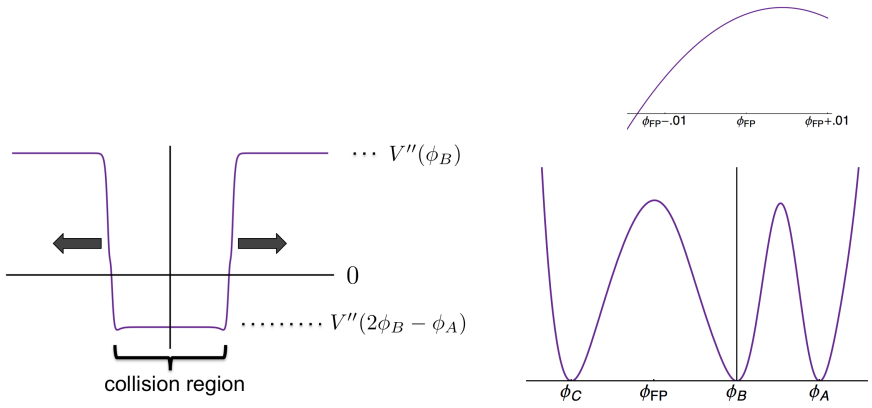

Figure 2.1: To the left is an example of a quantum analog potential after collision. This example is typical of those models that permit unstable mode(s) after collision. The particular collision this is associated with the one pictured in figures 2.3, and 2.4. The model's potential for this collision is shown on the right, with a magnified plot near the free passage field value also included in the upper right corner.

Our approach to analyzing the dynamics governed by 2.2.5 is informed by Coleman's proof of the stability of solitons [47]; we identify the right hand side as an ordinary quantum mechanical Hamiltonian operator acting on σ, with an analog quantum potential given by

$$V_{\mathrm{QM}}(t,x) = \left.\frac{\partial^2 V}{\partial \phi^2}\right|_{\phi_{\mathrm{FP}}} . \tag{2.2.6}$$

Qualitatively, this potential looks like a smoothed out finite square well (or barrier) with value $V''(\phi_B)$ outside the collision region, and $V''(2\phi_B - \phi_A)$ inside. In the relativistic limit, the walls become Lorentz contracted and the potential looks increasingly like a widening square well (or barrier, depending on the magnitudes of $V''(2\phi_B - \phi_A)$ and $V''(\phi_B)$). An example of such an analog quantum potential is shown in figure 2.1.

Of particular interest are cases where the field makes it into the basin of attraction of a new local minimum — which we'll call ϕ_C — but does not migrate sufficiently far into the basin for the curvature of the potential to turn positive. In such cases, our quantum potential is a widening square well with a negative bottom, which means negative energy eigenstates are possible. While negative energies are not particularly

special in the Schrödinger equation, here they are suggestive of exponentially growing (and decaying) modes.

The instantaneous ground state of this system starts with energy $V''(\phi_B) > 0$ immediately after the collision, and then decreases as the well widens, approaching $V''(2\phi_B - \phi_A) < 0$ as $t \to \infty$. Consider a time $t_0 > 0$ when the ground state energy is negative. Had our Hamiltonian been time independent, the ground state, $\psi_0(t_0, x)$, would have evolved exponentially according to $\exp(\pm\sqrt{|E|}(t - t_0))$. While the time dependence of the system does factor in, we can still trust that a growing mode is present as long as the ground state changes sufficiently slowly[3]. Note that implicitly we assume the walls are boosted to a sufficiently large speed that linearization is still valid at t_0.

Of course, at time t_0 the ground state component of the deviation from free passage may be positive or negative. So the mode's contribution to the field's evolution post free passage can be towards or away from ϕ_C. To clarify this we write

$$\sigma(t_0 + dt, x) \sim \alpha_0 \exp(\sqrt{|E_0|}dt) + \beta_0 \exp(-\sqrt{|E_0|}dt)]\psi_0(t_0, x) + ... \tag{2.2.7}$$

where the ellipses represents the contributions from the remaining modes. These consist of scattering states, which are all stable, and additional bound states which, though possibly unstable, are less unstable than the ground state. Hence we expect dynamics (given by the EOM for σ in this subsection, obtained from keeping only the first order forcing) to be dominated by the ground state. The ground state, like any state, is not unique up to a phase. Let us take ψ_0 to be real and positive. Then α_0 is real, and the ground state contributes a push toward ϕ_C if the sign of α_0 is the same as $\phi_C - (2\phi_B - \phi_A)$ (negative for us), and vice-versa (i.e. retreat to the original

[3]More precisely, as long as the overlap between two successive ground states is sufficiently close to 1 so that the exponentially growing factor dominates it, the mode will grow. There is always a t_0 large enough such that this is the case. For a more thorough treatment consult the Appendix.

bubble vacuum).

In terms of the deviation's initial conditions (given at time t_0 that satisfies the above conditions), α_0 is

$$\alpha_0 = \int \psi_0(t_0, x)[\sigma(t_0, x) + \frac{1}{\sqrt{|E_0|}}\dot{\sigma}(t_0, x)]. \tag{2.2.8}$$

The initial conditions for σ are essentially the accumulated effect of the full zeroth order forcing term on ϕ up until t_0 (ignoring $\mathcal{O}(\epsilon)$ terms in σ's EOM is valid until t_0). Recall this term is given by,

$$-\frac{\partial V}{\partial \phi}\bigg|_{\phi_{FP}(t,x)} + \frac{\partial V}{\partial \phi}\bigg|_{f_L(t,x)} + \frac{\partial V}{\partial \phi}\bigg|_{f_R(t,x)}. \tag{2.2.9}$$

Here we demonstrate that our analysis reproduces the correct behavior in the limit $u \to 1$, where ϕ_C bubble nucleation is successful. The deviation the instant after collision, which results from integrating the above forcing against the appropriate Green's function, vanishes in this limit because it is suppressed by u/γ (see eq. 16 in [44]). After this instant, the only non-negligible forcing in the collision region is simply $-V'(2\phi_B - \phi_A)$. Consequently, α_0 will have the same sign as $\phi_C - (2\phi_B - \phi_A)$, since $2\phi_B - \phi_A$ is in the basin of attraction of ϕ_C. Hence, both zeroth and first order forcing terms in σ's EOM would result in the field being pushed toward ϕ_C if treated independently. Also, note that qualitatively our analysis reproduces the correct spatial dependence of the solution post collision — the distance the field rolls toward ϕ_C is peaked in the center of the collision region and decreases to nearly zero at the walls. So long as the contribution to $\sigma(t_0, x)$ and $\dot{\sigma}(t_0, x)$ from the forcing *after* the walls finish passing through each other dominates the contribution accumulated until this time, we expect successful bubble ϕ_C bubble nucleation.

If, on the other hand, the speed is not sufficiently large that the contribution from the forcing before/during collision is negligible it is possible for α_0 to be of the opposite

sign as $-V'(2\phi_B - \phi_A)$. In such a case there is a competition between the zeroth and first order forcing terms. This raises a perhaps surprising prospect. The field could realize enough of the free passage kick that the collision region is indeed taken into the basin of attraction of ϕ_C, but fall short enough that α_0 is sufficiently large in magnitude that the first order forcing term dominates the dynamics. This would mean that, despite having made it into the basin of attraction of a new vacuum via free passage, the field in the collision region would nonetheless be pulled back uphill towards the original bubble vacuum. If the effect is significant enough the field would make it all the way back over the barrier, into the old bubble's basin of attraction thereby undoing the kick from free passage and preventing a bubble of new vacuum from forming. In particular, this would mean that consideration of the post-collision dynamics raises the minimum collision speed necessary to complete the free passage transition.

Competition Of Time Scales

Whether the instability identified in the previous section is realized depends on how the time scale associated with its growth compares with that associated with the zeroth order term. If the slope at $2\phi_B - \phi_A$ is sufficiently large, the field in the collision region accelerates quickly, and the window for exciting the growing mode is lost. The time scale associated with the zeroth order term can be determined by dropping the Laplacian of the deviation and explicitly solving the resulting differential equation,

$$\ddot{\sigma} \approx V'_{2\phi_B-\phi_A} \rightarrow \sigma \sim \frac{V'_{2\phi_B-\phi_A}}{2} t^2 + \mathcal{O}(t). \tag{2.2.10}$$

Hence, the time scale associated with the zeroth order driving term is

$$t_{\text{zeroth}} \sim \frac{1}{\sqrt{V'_{2\phi_B-\phi_A}}}. \tag{2.2.11}$$

The time scale associated with the first order term is roughly given by the time for one e-folding, which in turn depends on the depth of the analog quantum potential,

$$t_{\text{linear}} \sim \frac{1}{\sqrt{|V''_{2\phi_B-\phi_A}|}} \tag{2.2.12}$$

This suggests that in models with

$$\sqrt{\frac{|V''_{2\phi_B-\phi_A}|}{V'_{2\phi_B-\phi_A}}} \gg 1, \tag{2.2.13}$$

the field in the collision region may not simply roll down towards ϕ_C, but rather be significantly influenced by the unstable mode. As indicated previously, whether the mode grows to drive the field toward ϕ_B or ϕ_C depends on the initial conditions for the deviation.

In the following section we undertake a detailed numerical study of this issue and try to determine the threshold value for the expression in equation (2.2.13) for which the field returns to ϕ_B after the collision.

2.3 Numerical Survey

In the previous section we presented a heuristic argument for why the time evolution after a free passage kick takes the field into the basin of attraction of new vacuum (ϕ_C) may bring the field back to the original vacuum (ϕ_B), rather than causing it to roll to ϕ_C. Again, even in such cases there exists a speed above which the "naive" picture of dynamics — free passage followed by evolution according to $-V'$ at the kicked field value — will be realized. Our point, though, is that there can be potentials in which this threshold speed is greater than one would naively expect, due to the instability we've identified. For potentials in which $2\phi_B - \phi_A$ lies in the basin of attraction of a new vacuum, the naive expectation is that the threshold will have been passed if the

kicked field in the collision region is within a small enough distance of $2\phi_B - \phi_A$ that it lies in the new minimum's basin of attraction.

We want to study how the detailed features of the potential, such as the relative size (and sign) of the first and second derivatives at $2\phi_B - \phi_A$, determine whether the free passage dynamics nucleates a bubble of new vacuum, ϕ_C. Thus, we numerically simulate relativistic soliton-anti soliton collisions in models where $V'(2\phi_B - \phi_A)$, and $V''(2\phi_B - \phi_A)$ can be tuned. In particular, we studied the following two potentials, each with degenerate local minima at $\phi = -2, 0,$ and 1:

$$V(\phi) = \phi^2(\phi-1)^2(\phi+2)^2\left(1 + k_1\exp(-k_2(\phi+.2)^2) + k_3\exp(-4(\phi-.5)^2)\right) \quad (2.3.1)$$

and,

$$V(\phi) = \phi^2(\phi-1)^2(\phi+2)^2\left(1 + k_1\exp(-k_2(\phi+.2)^2)(\phi+k_4) + k_3\exp(-4(\phi-.5)^2)\right). \quad (2.3.2)$$

The same initial value problem laid out in section 2.1 is solved with the Cactus Computational Toolkit utilizing a fourth order Runge-Kutta method. For each choice of parameters $\{k_i\}$ we have determined whether the field in the collision region, after receiving its free passage kick, rolls toward the new vacuum at $\phi_C = -2$, or retreats to the original bubble vacuum $\phi_B = 0$. The figure below displays the results. Runs are plotted in the $V'(2\phi_B - \phi_A)$-$V''(2\phi_B - \phi_A)$ plane, and the color indicates the outcome: purple for those that retreat back toward $\phi_B = 0$, and black for those that roll toward $\phi_C = -2$.

The runs naturally separate based on the relative magnitude of $V''(2\phi_B - \phi_A)$, and $V'(2\phi_B - \phi_A)$, as expected. The boundary between the two regions is approximately linear, with slope ~ -26.5. We thus find that the threshold for successful new bubble nucleation via free passage may be increased above the level naively expected (that

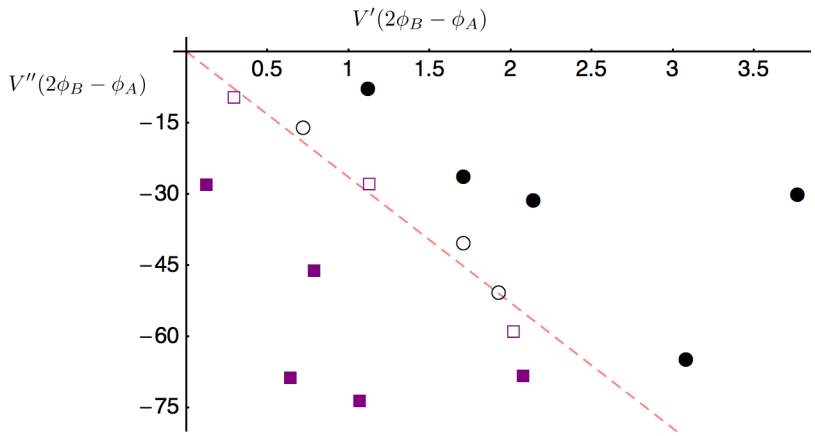

Figure 2.2: The results of numerical simulations for various values of $V'(2\phi_B - \phi_A)$ and $V''(2\phi_B - \phi_A)$. Cases where the field retreats back toward ϕ_B are indicated by a purple square while those that continue toward ϕ_C are indicated by black circles. Note that there is a rough boundary that separates the two classes. We've unshaded the simulations deemed to lie along this boundary, and plotted a least squares fit to these points which has slope -26.5.

which lands the field in the basin of attraction of the new vacuum) for models with

$$\frac{|V''(2\phi_B - \phi_A)|}{V'(2\phi_B - \phi_A)} \gtrsim 26.5. \tag{2.3.3}$$

Snapshots of a collision in a model representative of those where the field in the collision region in pulled back into the basin of attraction of ϕ_B are shown in figures 2.3 and 2.4. We do this to illustrate that the mechanism for this "failure to nucleate" is indeed our unstable mode. Notice that the retreat begins in the center of the collision region and eventually drags the rest of the interior back to ϕ_B. For this particular simulation we used the potential given by 2.3.1, with parameters $k_1 = 1.85$, $k_2 = 1.54$, and $k_3 = 15$, along with a wall speed $u = .999$.

For a given model, the soliton used to construct initial conditions in 2.1.4 was approximated as follows:

$$f(x) = \frac{1}{\sqrt{1 + 3\exp(-x\sqrt{V''(1)})}} \tag{2.3.4}$$

This is a modification of the exact soliton that interpolates between the same vacua, $\phi = 0$ and $\phi = 1$, for the potential,

$$V(\phi) = \phi^2(\phi^2 - 1)^2 \tag{2.3.5}$$

We chose the coefficient in the exponential to be $\sqrt{V''_{\phi=1}}$ in order to send any waves that developed from relaxation of the walls away from the collision region. The effect of the approximation is minimal, as can be seen by comparing the plots in figures 2.3, and 2.4 with the corresponding ones obtained for the same collision simulated using the "true" soliton in the field's initial conditions, pictured in figures 2.5, and 2.6[4].

2.4 Generality Of Instability

While we have demonstrated the existence of an instability, it is now important to address the issue of generality. In particular, how finely tuned does a potential have to be to exhibit the kind of first and second derivatives required by equation (2.3.3)? More precisely we must have this inequality satisfied at $2\phi_B - \phi_A$.

Consider the slope of the potential evaluated very close to $2\phi_B - \phi_A$. As long as the potential is well behaved near that point and derivatives of order higher than two are not very large themselves, we may expand and write

$$V'(2\phi_B - \phi_A + \epsilon) \approx V'(2\phi_B - \phi_A) + V''(2\phi_B - \phi_A)\,\epsilon. \tag{2.4.1}$$

[4]We have recently developed an approach for more accurately constructing initial conditions. Instead of using the closed form approximate expression given in 2.3.4, we use a discrete approximation to the "true" soliton obtained by numerical inversion of

$$x = \int_{f(0)}^{f(x)} \frac{d\phi}{\sqrt{2V(\phi)}}. \tag{2.3.6}$$

By limiting the values of the upper bound to the interval between two neighboring vacua the above is a definition for soliton $f(x)$ equivalent to the usual definition given in terms of a BVP. We have checked that this more precise form has only a marginal affect on our numerical survey of the soliton collisions.

Since the second derivative is so much larger in magnitude than the first derivative, we can set the right hand side of this expression equal to zero by choosing a very small $\epsilon \sim 1/26.5$. In other words, we must be very close to an extremum of the potential. This places severe limitations on the types of potentials in which migration into the basin of attraction via free passage is only temporary. In particular, the locations of the minima of the potential must be so finely tuned that $2\phi_B - \phi_A$ is nearly at a maximum of the potential.

Though our analysis is based on a first order Taylor expansion of V' about the free passage field value being valid for at least some $\delta > \epsilon \sim 1/26.5$, the results suggest it might be worth considering potentials where the condition on the ratio of the first and second derivatives is satisfied in a large interval around $2\phi_B - \phi_A$, albeit without requiring such a δ. For instance, if one inserted an exponential segment, $V \sim \exp[-K\phi]$, into the standard three minima potentials we've considered thus far in an interval around the free passage field value, then the ratio of first to second derivatives everywhere in the interval will be $-1/K$. The size of the interval is arbitrary, so the distance between the locations of the parent and bubble vacuum can be moved liberally, without changing the ratio of the derivative at the kicked field value.

Qualitatively, such a potential will have a plateau leading to a very steep cliff in between the bubble and new vacua, since K must be chosen quite large. Preliminary numerical results indicate that uphill retreat post collision via our unstable ground state may in fact be realized for some potentials of this sort. To avoid a potential that is defined piece-wise, we "carve out" two Gaussians from the plateau in the following way:

$$V(\phi) = 1 - \exp(-K(\phi - \eta)) - \exp(-k_1(\phi - \phi_A)^2) - \exp(-k_2(\phi - \phi_B)^2) \quad (2.4.2)$$

Once again, soliton-anti soliton collisions were simulated with ϕ_B as the bubble vacuum, and ϕ_A as the parent. We took $\eta = -3.5$, $K = 20$, $k_1 = 10$, $k_2 = 5$, $\phi_B = 0$, wall speed $u = .99$, and varied ϕ_A. We started with $\phi_A = 3$, and observed retreat toward the ϕ_B vacuum. In each successive run, ϕ_A was increased. This has the effect, essentially, of leaving the potential in between η, and ϕ_B unchanged. As far as a collision is concerned, moving ϕ_A toward 3.5 has the sole effect of moving the free passage kicked field value leftward along the plateau, ever closer to the cliff, without changing what the potential looks like between the cliff and the entrance to the basin of attraction of the ϕ_B vacuum. A plot of the potential for an example one of these simulations, that with $\phi_A = 3.25$, can be found in figure 2.7.

Our goal was to determine how close to the cliff the free passage kicked field could be (i.e. how large the magnitude V' could be), and yet still exhibit this retreat (in the opposite direction of $-V'$) to the original bubble vacuum. Essentially, at what point do dynamics after collision switch from retreat to rolling off the cliff? We've found that this threshold ϕ_A value lies in between 3.25 and 3.35, as all simulations with $\phi_A \leq 3.25$ retreated, and that with $\phi_A = 3.35$ fell off. Snap shots of an example of a simulation in which retreat occurs, that with $\phi_A = 3.25$, are displayed in figure 2.8.

Of course, the threshold ϕ_A value could be resolved further. These preliminary results nonetheless suggest that the somewhat surprising behavior suggested by our heuristic argument (based on linear analysis), observed in our corresponding numerical survey, and deemed finely tuned for the usual potentials considered (resembling those of simple polynomial form), may be quite general in other classes of models. This is because the effect might extend to models where the condition 2.3.3 is satisfied in a large (non negligible) neighborhood around the free passage kicked field location (hence not finely tuned), but where linearization about the free passage solution in the collision region is not valid in throughout the larger interval.

2.5 Conclusion

In this chapter we have investigated bubble collisions in single scalar field theories whose potentials admit multiple local minima. Motivated by the findings of [43], where high velocity bubble collisions were shown to be governed by free passage dynamics, we've studied post-collision evolution to determine the efficacy of classical nucleation of new bubble vacua. Specifically, we've used analytical and numerical arguments to assess the post-collision deviation from free passage dynamics, and identified potentials for which such deviations both rapidly grow and drive the field away from producing bubbles of with new vacuum field values. An interesting question touched on here, but deserving of more detailed study is the genericity of such deviations.

A natural next step is to consider these questions in multi-field models. With an eye toward applications to eternal inflation and the string landscape, we determined the generalization of free passage to field theories with noncanoical kinetic terms, that is field space curvature, in [48]. These results are presented in the following chapter.

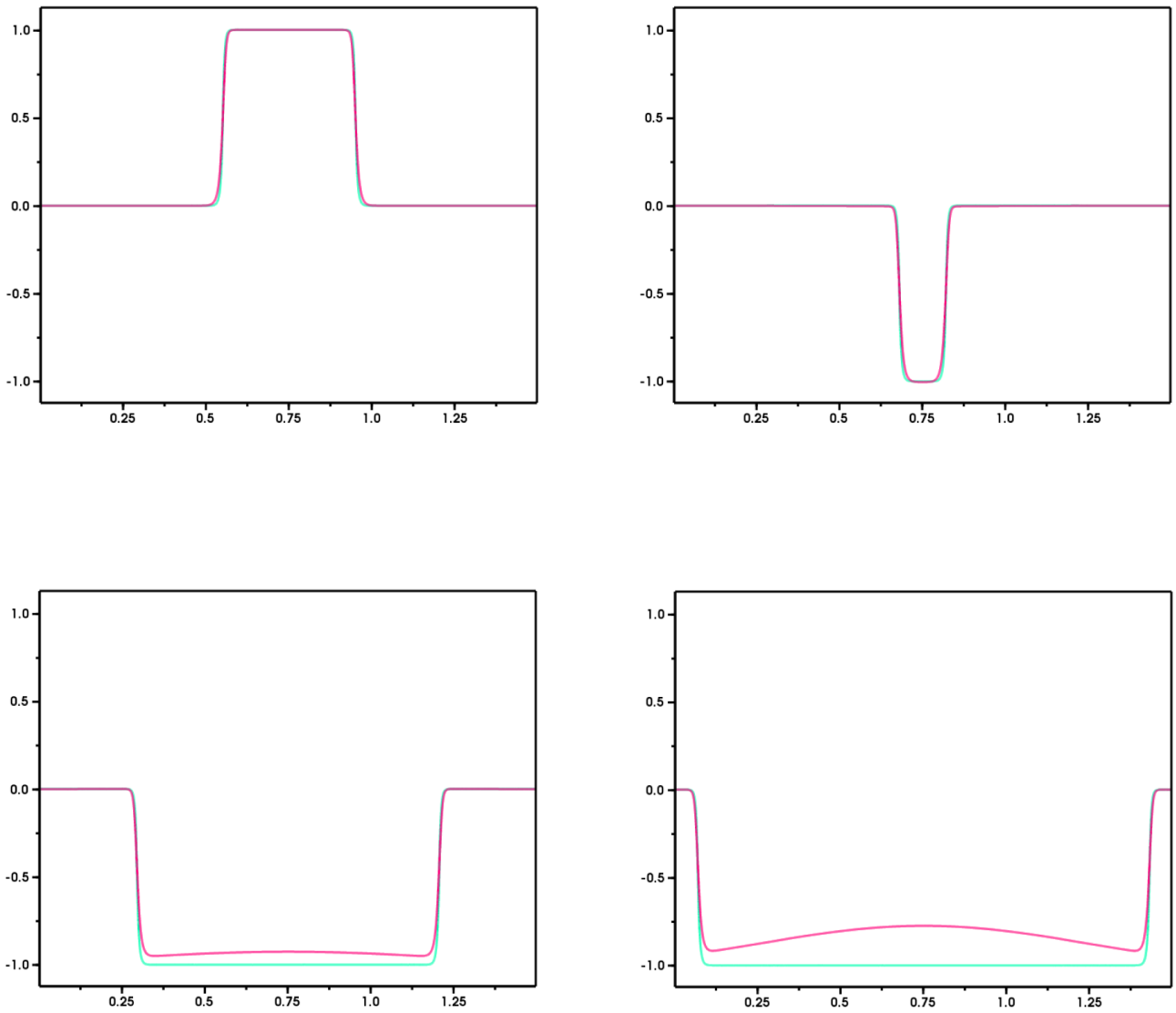

Figure 2.3: A representative case where the field retreats back to ϕ_B despite temporarily migrating into basin of attraction of the minimum at -2 after the collision. The solution to the field's EOM, in red, is plotted over the free passage solution, in green. (Note: solitons in the field's initial conditions were approximated by 2.3.4, whereas those used in the free passage solution were constructed by numerical inversion as discussed in the footnote on page 56. As noted, the effect of using the more exact numerical approach is minimal.)

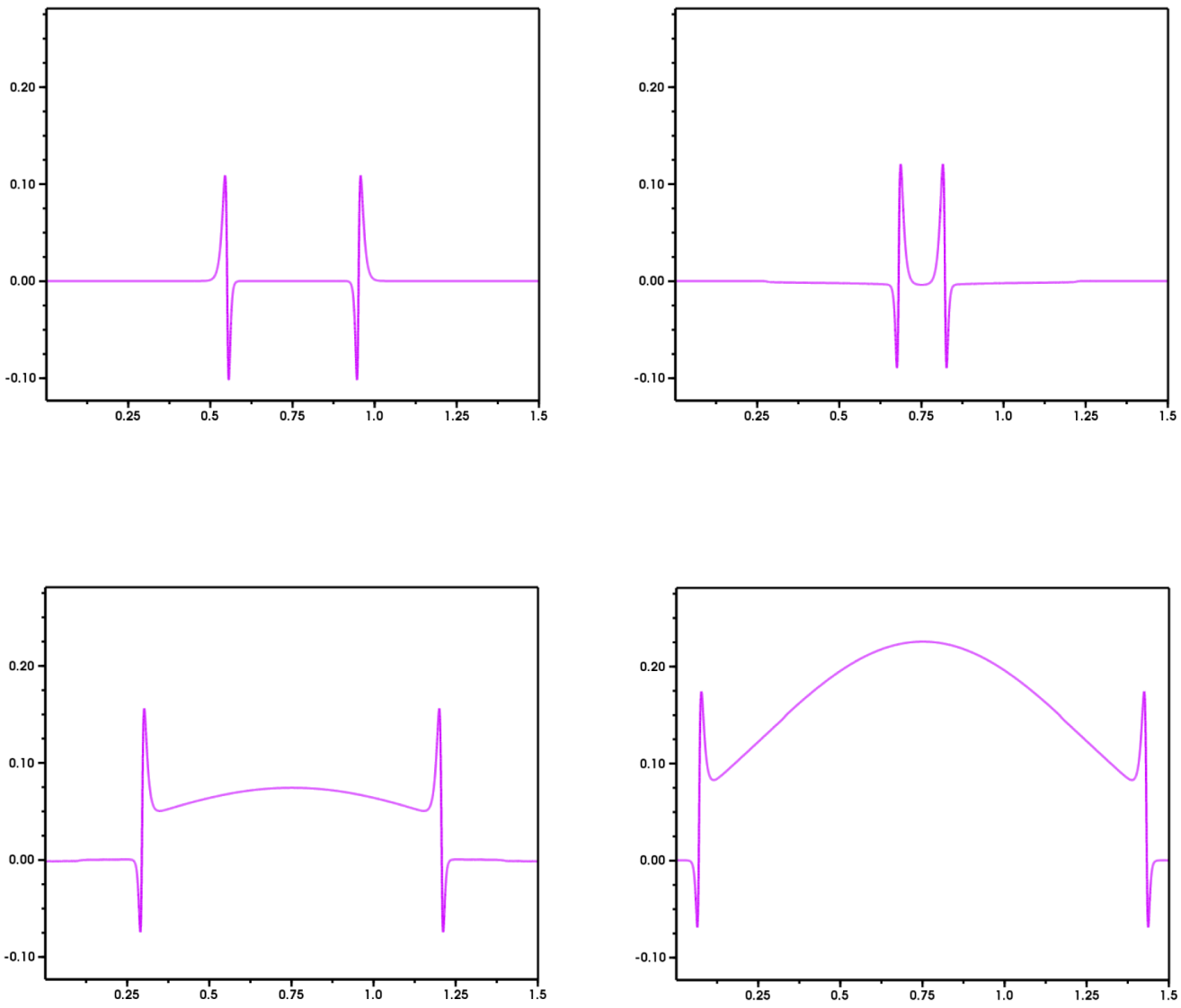

Figure 2.4: For each snapshot in figure 2.3 we plot the corresponding deviation from free passage, merely computed as the difference between the actual field solution and the free passage solution. Notice that the shape of the instability is similar to the ground state of a finite square well thus supporting our heuristic argument in section 2.2. The kinks at the wall locations indicate that the soliton approximation, 2.3.4, produces a slightly wider soliton than the true one. The persistence of the kinks throughout the snapshots means that the approximate walls stay intact. Thus, retreat to the original bubble vacuum does not result from collapse of the walls, but rather from evolution of the field inside the collision region. The former behavior would not be an example of our effect since the ground state is nearly zero at the walls. Instead, it would be the "temporary excursion" observed by [43], [44] at insufficiently relativistic speeds.

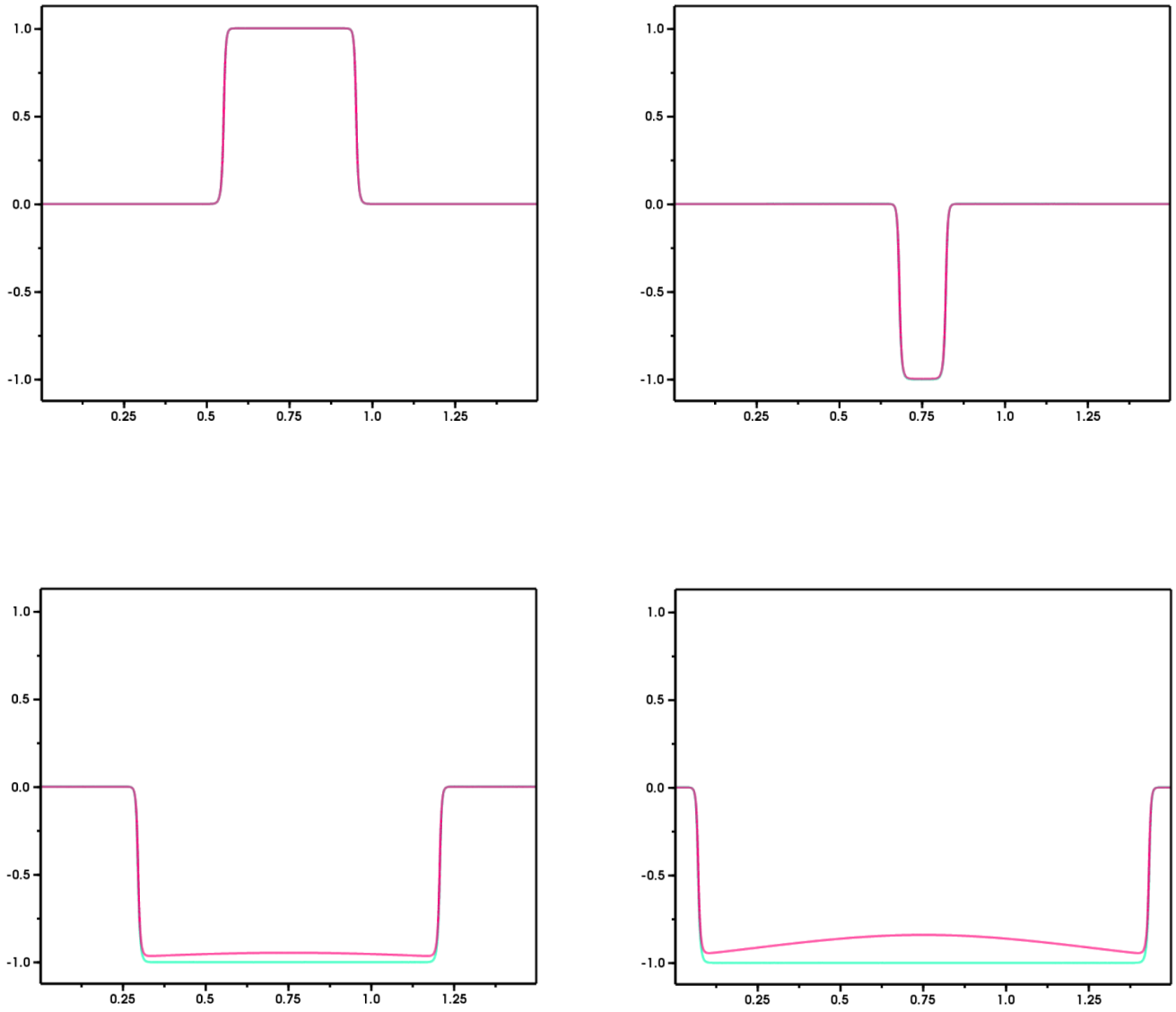

Figure 2.5: Results of the same collision pictured in figure 2.3, only with solitons in the field's initial conditions constructed using the more accurate method described in the footnote on 56. All parameter values, including initial wall locations, and speed, were identical for the two runs. The solution to the field's EOM is in red, and the free passage solution is in green.

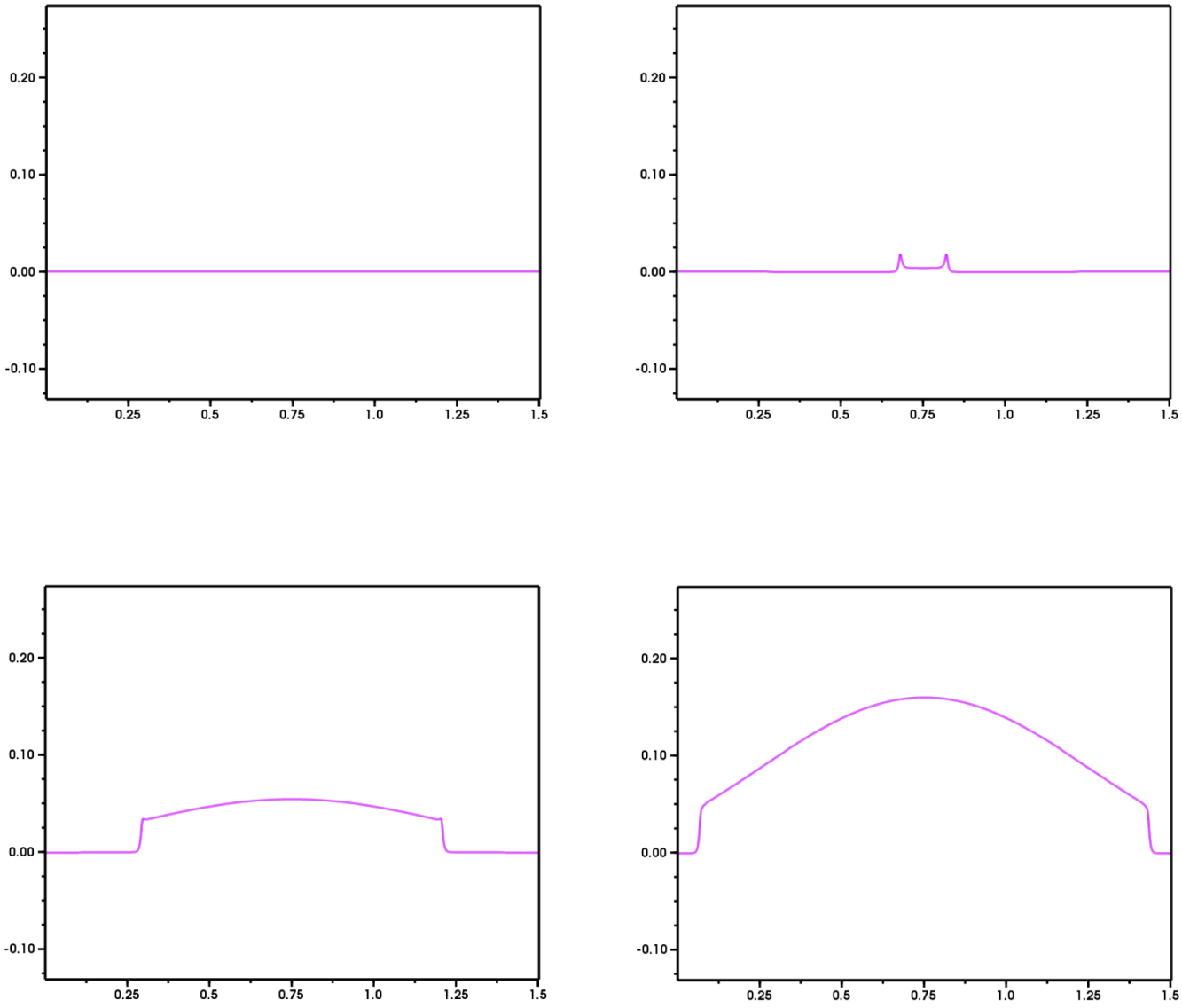

Figure 2.6: The deviation from free passage for the snap shots in figure 2.5, computed as the difference between the actual field solution and free passage solution.

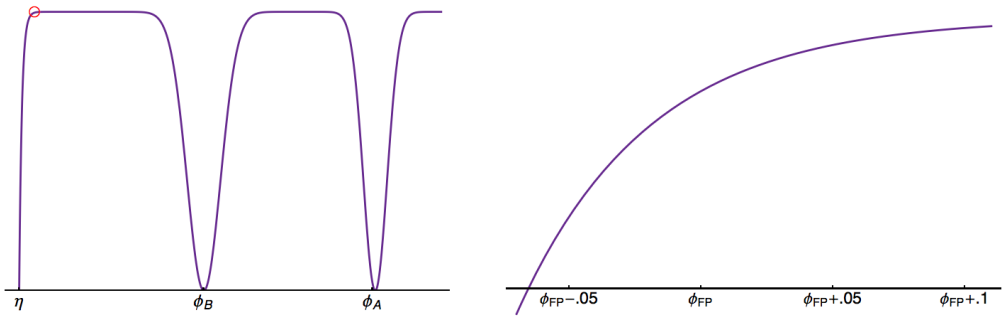

Figure 2.7: On the left is a plot of the potential given by 2.4.2 with parameter values $\eta = -3.5$, $K = 20$, $k_1 = 10$, $k_2 = 5$, $\phi_A = 3.25$ and $\phi_B = 0$. On the right we include a magnified plot of the potential near the free passage field location, $2\phi_B - \phi_A$ (circled in red on the unmagnified plot). The results of a soliton-anti soliton collision for this model are pictured in figure 2.8.

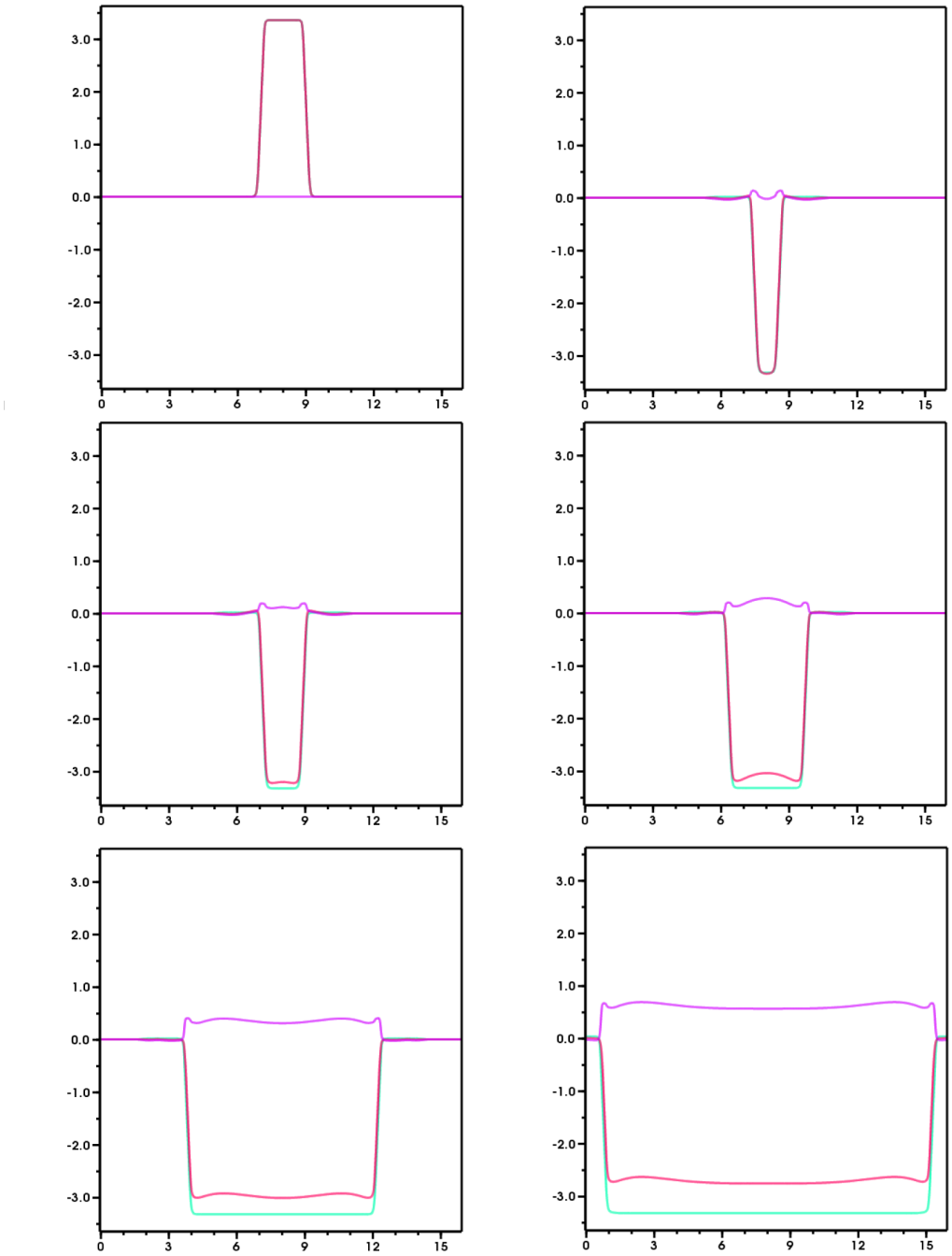

Figure 2.8: Snapshots of the collision of two ϕ_B bubbles nucleated in parent ϕ_A for the potential pictured in figure 2.7. The field is plotted in red, the free passage solution in green, and the deviation in purple. The field in the collision region is kicked via free passage to a location where $-V'$ is negative, yet nonetheless retreats in the positive direction — running through an entire interval where $-V'$ is negative — ultimately back to the original bubble's basin of attraction.

Chapter 3

Collisions in Curved Field Space

As we found in [48], the presence of field space curvature modifies this story nontrivially. Again, we used the proxy of boosted solitons in $1+1$D for expanding bubbles in $1+3$D. We made no restrictions on the field space dimension or its geometry aside from smoothness, and did not take the solitons to be identical. By transforming to an optimal set of variables the collision initial value problem takes the form of a boundary value problem whose solution can be understood geometrically. The collision of two solitons at ultrarelativistic impact velocity amounts to the mutual parallel transport (in field space) of the colliding solitons' tangent vector fields. Not only does this analysis determine the field configuration in the collision region, but also the spatial profiles of the outgoing walls. Unlike in the flat case, we found that ultrarelativistic collisions in curved field space are not in general shape preserving. These results are based on analytic calculations which we also verified in particular examples through numerical studies.

The ultimate fate of the field configuration after a given collision depends crucially on the potential in the neighborhood of field space targeted by parallel transport. Such landing locations depend on the field space geometry throughout a submanifold containing the parent, and bubble vacua, as well as on the shapes of the two solitons collided. The curves these solitons trace out in field space set the boundary conditions for the parallel transported vector fields. A natural and important step toward determining the effectiveness of classical collisions in populating the landscape then is to gain an understanding of the field space geometry, the shapes of soliton curves

and the distribution of vacua in models from actual flux compactifications.

In this chapter we address key subtleties in bubble collisions, even at high relative velocity, that arise from the inherent nonlinearity of nontrivial curvature, and find a satisfying geometrical interpretation of our result. Specifically, in section 3.1 we generalize the notion of the free passage approximation from flat to curved field spaces. We derive a geometrical interpretation of the result in terms of the parallel transport of integral curves on moduli space. In section 3.2 we argue that there always exists a regime in which our generalized free passage approximation applies, and in section 3.3 we numerically study some bubble collision examples (in the setting of 1+1D) and compare the results to those from our analytic expressions in section 3.1.

3.1 Generalization of Free Passage

We take as our starting point the action

$$S = \int d^2x \left(\frac{1}{2} g_{ij} \partial_\mu \phi^i \partial^\mu \phi^j - V(\phi) \right) \tag{3.1.1}$$

where g_{ij} is the generally curved metric on the field space. We assume the potential $V(\phi)$ has three (or more) degenerate minima at the field space locations A, B, and C (the minimum necessary to study collisions as a source of vacuum transitions). The Euler-Lagrange equation takes the form,

$$\Box \phi^i + \Gamma^i_{j\,k} \partial^\mu \phi^j \partial_\mu \phi^k = -\frac{\partial V}{\partial \phi_i} \tag{3.1.2}$$

The A vacuum will play the role of the parent vacuum, and B and C those of the two bubble vacua we seek to collide. Static solutions to (3.1.2) that interpolate between distinct yet degenerate local minima of the potential are solitons. We define $f^i(x)$, and $h^i(x)$ as the components of those solitons centered at $x = 0$ with the following

asymptotics,

$$\lim_{x\to-\infty} f^i(x) = B^i \tag{3.1.3}$$

$$\lim_{x\to+\infty} f^i(x) = A^i \tag{3.1.4}$$

$$\lim_{x\to-\infty} h^i(x) = C^i \tag{3.1.5}$$

$$\lim_{x\to+\infty} h^i(x) = A^i \tag{3.1.6}$$

Our intent is to work out the formalism to describe the collisions between these solitons, taking into account the curved moduli space metric. Of particular interest is the limiting behavior that emerges at ultrarelativistic impact velocity.

The collision of two initially widely separated solitons, say, right-moving f^i, and left-moving h^i (that interpolate between the parent vacuum A and the other local minima B and C, respectively) is described by an observer in the center of the rest frame of the collision by the following initial value problem:

$$\Box\phi^i + \Gamma^i_{j\,k}\partial^\mu\phi^j\partial_\mu\phi^k = -\frac{\partial V}{\partial\phi_i} \tag{3.1.7}$$

$$\phi^i(-T,x) = f^i(\gamma(x-u(-T))) + h^i(-\gamma(x+u(-T))) - A^i \tag{3.1.8}$$

$$\partial_t\phi^i(-T,x) = -u\gamma\left(f^{i\prime}(\gamma(x-u(-T))) + h^{i\prime}(-\gamma(x+u(-T)))\right) \tag{3.1.9}$$

where we've shifted the time coordinate so that the observer's clock is zero when the trajectories of the centers of the colliding solitons (given by $x_{R,0} = ut$ for right-moving f^i, and $x_{L,0} = -ut$ for left-moving h^i) coincide.

In order to be a legitimate representation of a soliton collision, the solitons must be widely separated at the initial time, $-T$. Thus, valid values of T are those for which uT is much much greater than the width of all components of both Lorentz contracted solitons (so the observer measures field value $\phi^i = A^i$ to an exceedingly good approximation initially, since outside this width the solitons approach their

asymptotic values as decaying exponentials). To make this precise we'll define a positive constant w such that all components of the solitons we wish to collide, $f^i(x)$ and $h^i(x)$, differ from the relevant vacuum value by an insignificant amount outside of $x \in [-w/2, w/2]$. That is,

$$\frac{|B^i - f^i(-w/2)|}{|A^i - B^i|} \ll 1 \tag{3.1.10}$$

$$\frac{|A^i - f^i(w/2)|}{|A^i - B^i|} \ll 1 \tag{3.1.11}$$

$$\frac{|C^i - h^i(-w/2)|}{|A^i - C^i|} \ll 1 \tag{3.1.12}$$

$$\frac{|A^i - f^i(w/2)|}{|A^i - C^i|} \ll 1. \tag{3.1.13}$$

So, the initial time $-T$ is any time such that $uT > w/2\gamma$. We'll view the collision as commencing at time $t_{start} = -w/2\gamma$, and lasting until $t_{end} = +w/2\gamma$. The "usefulness" then of an approximation to the actual solution to the collision initial value problem (defined by 3.1.7, 3.1.8, and 3.1.9), at given impact velocity u, is proportional to the fraction of the collision for which the approximation remains valid. Labeling the time until which an approximation accurately captures the dynamics by t_{approx}, the approximation's usefulness is gleaned from t_{approx}/t_{end}. The greater this is the more useful the approximation is, and it will be deemed "fully realized" if $t_{approx} \geq t_{end}$.

The task of understanding the dynamics of collisions in the ultrarelativistic limit amounts to finding a one parameter family of approximations — "free passage field configurations" we'll denote by $\{\phi^i_{FP}(t, x; u)\}_{u\in(0,1)}$ — that are ever more useful approximations to the collision initial value problem's true solution as u is taken to 1. After constructing $\{\phi^i_{FP}(t, x; u)\}_{u\in(0,1)}$ we conclude this section with a proof that there always exists an impact velocity close enough to 1 to ensure that the free passage configuration is fully realized.

We first perform a change of variables from t and x to the natural dynamical variables of the problem, namely the spatial coordinates of the boosted observers riding on the soliton walls, $\sigma := \gamma(x - ut)$, and $\omega := \gamma(x + ut)$, which we'll refer to as the Lorentz variables. This choice of variables enables us to isolate the effect of one soliton, say, left-moving h, on the field at a fixed location on the other soliton, in this case f. By holding σ constant and letting ω vary from minus infinity to infinity one focuses on a fixed location on the right-moving soliton and follows how the field evolves under the influence of the collision with the left-moving soliton.

Similarly, the impact of right-moving f on h can be ascertained by holding ω constant and varying σ. Expressing ϕ in terms of these, the equation of motion takes the form,

$$\begin{aligned} &- 4(1-\epsilon)\gamma^2 \left[\frac{\partial^2\phi^i}{\partial\sigma\partial\omega} + \Gamma^i_{j\,k}\frac{\partial\phi^j}{\partial\sigma}\frac{\partial\phi^k}{\partial\omega}\right] \\ &- 2\gamma^2\epsilon\left[\frac{\partial^2\phi^i}{\partial\sigma^2} + \frac{\partial^2\phi^i}{\partial\omega^2} + \Gamma^i_{j\,k}\left(\frac{\partial\phi^j}{\partial\sigma}\frac{\partial\phi^k}{\partial\sigma} + \frac{\partial\phi^j}{\partial\omega}\frac{\partial\phi^k}{\partial\omega}\right)\right] = -\frac{\partial V}{\partial\phi_i} \end{aligned} \tag{3.1.14}$$

where we've expanded in $\epsilon = 1 - u$, since we are interested in the limiting dynamics that emerge when $u \to 1$. Rearranging and using $1/\gamma^2 = 2\epsilon$ we have,

$$\frac{\partial^2\phi^i}{\partial\sigma\partial\omega} + \Gamma^i_{j\,k}\frac{\partial\phi^j}{\partial\sigma}\frac{\partial\phi^k}{\partial\omega} = \frac{\epsilon}{2}\frac{\partial V}{\partial\phi_i} - \frac{\epsilon}{2}\left[\Gamma^i_{j\,k}\left(\frac{\partial\phi^j}{\partial\sigma}\frac{\partial\phi^k}{\partial\sigma} + \frac{\partial\phi^j}{\partial\omega}\frac{\partial\phi^k}{\partial\omega}\right) + \frac{\partial^2\phi^i}{\partial\sigma^2} + \frac{\partial^2\phi^i}{\partial\omega^2}\right]. \tag{3.1.15}$$

The initial conditions take the form,

$$\phi^i(\sigma,\omega)\Big|_{\partial\Omega_\gamma} = \left(f^i(\sigma) + h^i(-\omega) - A^i\right)\Big|_{\partial\Omega_\gamma} \tag{3.1.16}$$

$$\gamma u\left(\frac{\partial}{\partial\omega} - \frac{\partial}{\partial\sigma}\right)\phi^i\Big|_{\partial\Omega_\gamma} = -\gamma u\left[f^{i\prime}(\sigma) + h^{i\prime}(-\omega)\right]\Big|_{\partial\Omega_\gamma} \tag{3.1.17}$$

or,

$$\phi^i(\sigma,\omega)\Big|_{\partial\Omega_\gamma} = \left(f^i(\sigma) + h^i(-\omega) - A^i\right)\Big|_{\partial\Omega_\gamma} \tag{3.1.18}$$

$$\left(\frac{\partial}{\partial\omega} - \frac{\partial}{\partial\sigma}\right)\phi^i\Big|_{\partial\Omega_\gamma} = -\left[f^{i\prime}(\sigma) + h^{i\prime}(-\omega)\right]\Big|_{\partial\Omega_\gamma} \tag{3.1.19}$$

where $\partial\Omega_\gamma$ is the surface in the σ-ω plane of constant time $t = -T$. This boundary is simply the line, $\omega = \sigma - 2\gamma uT$, which note lies only in the first, third, and fourth quadrants. Its ω-intercept, $-2\gamma uT$, is less than $-w$ for any valid choice of T. We bisect $\partial\Omega_\gamma$ at the point $(\gamma uT, -\gamma uT)$ and name the half that lies in the third and lower fourth quadrants as $\partial\Omega_f$, and the half that lies in the first and upper fourth quadrants as $\partial\Omega_h$. These are indicated in figure 3.1 by the highlighted yellow, and blue rays, respectively. Since all points on $\partial\Omega_f$ have $\sigma < \gamma uT < w/2$, they satisfy,

$$\omega\big|_{\partial\Omega_f} = (\sigma - 2\gamma uT)\big|_{\partial\Omega_f} \leq -\gamma uT \leq -w/2$$

Similarly, all points on $\partial\Omega_h$ have $\omega > -\gamma uT > -w/2$, so their corresponding σ coordinate satisfies,

$$\sigma\big|_{\partial\Omega_h} \geq \gamma uT \geq w/2$$

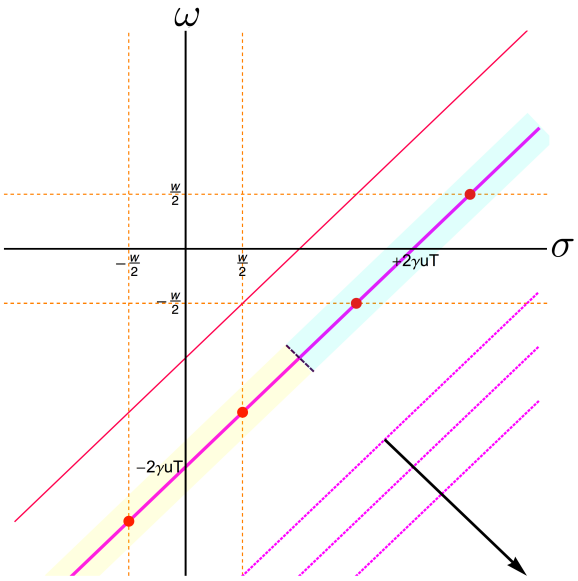

Figure 3.1: When a transformation from (t, x) to the Lorentz variables, $\sigma := \gamma(x - ut)$ and $\omega := \gamma(x + ut)$) is performed, the initial conditions for the collision of solitons boosted to impact velocity u are given by 3.1.18 and 3.1.19. The boundary where the initial data is given, the surface of constant time $t = -T$, is a line in the σ-ω plane with slope 1 and ω-intercept $-2\gamma uT$. We denote this boundary, for a given Lorentz factor and choice for T, by $\partial\Omega_\gamma$ (note that for the collision at a given u the valid T values are those such that the boundary lies below the line $\omega = \sigma - w$, indicated by the thin red line). The center of the f soliton in the shifted superposition in the boundary conditions occurs at the ω-intercept, and that of the h soliton in the superposition occurs at the σ-intercept. We've named the halves of $\partial\Omega_\gamma$ as $\partial\Omega_f$ and $\partial\Omega_h$ according to which soliton's center lies on it. These are indicated by the yellow and blue rays, respectively. In fact, the f soliton in the superposition is almost entirely contained within only the two red points on the yellow half– the points on $\partial\Omega_\gamma$ with $\sigma \in [-w/2, w/2]$. That is, to the left of this interval (in the third quadrant) f evaluates to very nearly B, and to the right evaluates to very nearly A. Similarly the h soliton is almost entirely contained within the two red points on the blue half. As γ is increased the boundary where the field and its derivatives are specified moves along the diagonal with negative slope toward the fourth quadrant, indicated by the black arrow. Consequently, the intervals where the f and h solitons in the superposition are approximately supported move further and further away from each other. Thus, the boundary data effectively splits into two independent pieces each involving a *single* Lorentz variable. On the yellow half boundary the field in the initial data evaluates ever more closely to $f(\sigma)$, and on the blue to $h(-\omega)$. In the limit $\gamma \to 1$ the ω values on the yellow half go to $-\infty$, and the σ values on the blue half go to $+\infty$.

The boundary conditions can then be rewritten as,

$$\partial\Omega_f : \sigma \leq w/2 \rightarrow \sigma - 2\gamma u T \leq -w/2$$

$$\phi^i(\sigma, \sigma - 2\gamma u T) = f^i(\sigma) + h^i(-(\sigma - 2\gamma u T)) - A^i \approx f^i(\sigma) + A^i - A^i = f^i(\sigma)$$

$$\left(\frac{\partial}{\partial\omega} - \frac{\partial}{\partial\sigma}\right)\phi^i(\sigma,\omega) = -\left(f^{i\prime}(\sigma) + h^{i\prime}(-\sigma + 2\gamma u T)\right) \approx -f^{i\prime}(\sigma)$$

$$\partial\Omega_h : \omega \geq -w/2 \rightarrow \omega + 2\gamma u T \geq w/2$$

$$\phi^i(\omega + 2\gamma u T, \omega) = f^i(\omega + 2\gamma u T) + h^i(-\omega) - A^i \approx A^i + h^i(-\omega)A^i = h^i(-\omega)$$

$$\left(\frac{\partial}{\partial\omega} - \frac{\partial}{\partial\sigma}\right)\phi^i(\sigma,\omega) = -\left(f^{i\prime}(\omega + 2\gamma u T) + h^{i\prime}(-\omega)\right) \approx -h^{i\prime}(-\omega)$$

Thus, the entire collision initial value problem stated in the Lorentz variables takes the approximate form:

$$\frac{\partial^2\phi^i}{\partial\sigma\partial\omega} + \Gamma^i_{j\,k}\frac{\partial\phi^j}{\partial\sigma}\frac{\partial\phi^k}{\partial\omega} = \frac{\epsilon}{2}\frac{\partial V}{\partial\phi_i} + \frac{\epsilon}{2}\left[\Gamma^i_{j\,k}\left(\frac{\partial\phi^j}{\partial\sigma}\frac{\partial\phi^k}{\partial\sigma} + \frac{\partial\phi^j}{\partial\omega}\frac{\partial\phi^k}{\partial\omega}\right) - \frac{\partial^2\phi^i}{\partial\sigma^2} - \frac{\partial^2\phi^i}{\partial\omega^2}\right]$$

$$\phi^i(\sigma,\omega)\Big|_{\partial\Omega_f} \approx f^i(\sigma) \tag{3.1.20}$$

$$\frac{\partial}{\partial\sigma}\phi^i(\sigma,\omega)\Big|_{\partial\Omega_f} \approx f^{i\prime}(\sigma) \tag{3.1.21}$$

$$\phi^i(\sigma,\omega)\Big|_{\partial\Omega_h} \approx h^i(-\omega) \tag{3.1.22}$$

$$\frac{\partial}{\partial\omega}\phi^i(\sigma,\omega)\Big|_{\partial\Omega_h} \approx -h^{i\prime}(-\omega) \tag{3.1.23}$$

Now we'll obtain the limiting form of these equations when $\gamma \rightarrow 1$. First we'll turn our attention to the boundary conditions. As γ is increased the boundary $\partial\Omega_\gamma$ is pushed along the diagonal with negative slope toward the fourth quadrant. This causes the ω values of points on $\partial\Omega_f$ to become increasingly negative, and the σ values on $\partial\Omega_h$ to become increasingly positive. Consequently, the approximations made in the boundary conditions (3.1.20, 3.1.21, 3.1.22, 3.1.23) become ever more

accurate.

This can be seen visually as well. The center of the f soliton occurs, by definition, at the ω-intercept of $\partial\Omega_\gamma$, and the center of the h soliton occurs at the σ-intercept. As $\partial\Omega_\gamma$ is pushed along the diagonal toward the fourth quadrant the intercepts move away from each other. The distance between the center of each soliton and the place where the boundary is bisected (the endpoint of both half boundaries) increases, resulting in ever more of the f soliton fitting on $\partial\Omega_f$, and the h soliton fitting on $\partial\Omega_h$.[1]

Thus, the limiting form of the boundary conditions is obtained by replacing the approximate equalities in 3.1.20, 3.1.21, 3.1.22, and 3.1.23 with equalities. Further, note that the two conditions involving the first derivatives (3.1.21, 3.1.23) no longer contain any additional information than what is captured by the two conditions on ϕ^i, (3.1.20, 3.1.22). Clearly the limit of the differential equation, 3.1.15, is obtained by dropping the $\mathcal{O}(\epsilon)$ term on the righthand side.

At the risk of stating the obvious we'll identify this limiting set of equations with the appropriate collision– that of the non-Lorentz contracted profiles f^i and h^i each propagating toward one another with speed $u = 1$ in the *free* theory. To see why this is the case, take the equation of motion and initial conditions associated with this collision,

$$\Box\phi^i + \Gamma^i_{j\,k}\partial_\mu\phi^j\partial^\mu\phi^k = 0 \tag{3.1.24}$$

$$\lim_{t\to-\infty}\phi^i(t,x) = f^i(x-t) + h^i(-(x+t)) - A^i \tag{3.1.25}$$

[1]If one is uncomfortable with this argument for the splitting of the boundary where the initial data is given into two independent pieces, a conformal map can be performed before limit that γ goes to infinity is taken. Under a conformal transformation from σ and ω to $\alpha = \tan^{-1}(\sigma)$ and $\beta = \tan^{-1}(\omega)$, the boundary $\partial\Omega_\gamma$ becomes a hyperbola in the α-β domain (which is the square $[-\pi/2, \pi/2] \times [-\pi/2, \pi/2]$). As γ is increased the hyperbola is pushed further and further into the lower right of the square, and ultimately becomes the union of the horizontal edge at $\beta = -\pi/2$ (σ varying edge), and the vertical at $\sigma = \pi/2$ (ω varying edge). Though it provides a perhaps a more visually satisfying argument in favor of the split, we do not view the conformal map as necessary.

and transform to the characteristics, $\xi = x - t$, and $\eta = x + t$. Doing so yields,

$$\frac{\partial^2 \phi^i}{\partial \xi \partial \eta} + \Gamma^i_{j\,k} \frac{\partial \phi^j}{\partial \xi} \frac{\partial \phi^k}{\partial \eta} = 0 \tag{3.1.26}$$

$$\phi^i(\xi, -\infty) = f^i(\xi) \tag{3.1.27}$$

$$\phi^i(\infty, \eta) = h^i(-\eta) \tag{3.1.28}$$

Since the righthand side of the resulting differential equation is *identically* zero, we view *this* problem as the limit of the original one (the collision of boosted solitons in the model with nontrivial potential, V). So, the approximation to the true solution of the $u < 1$ collision problem should be defined by obtaining the solution to the free problem (3.1.26, subject to 3.1.27, and 3.1.28), and then evaluating it at the Lorentz variables as opposed to the characteristics. If we denote the solution to the free problem by $\Phi^i(\xi, \eta)$, we mean the approximation for impact velocity u ought to be defined by,

$$\phi^i_{FP}(t, x; u) \equiv \Phi^i(\gamma(x - ut), \gamma(x + ut)) \tag{3.1.29}$$

Turning our attention to Φ^i, we note that it maps $\mathbb{R}^2$ to a submanifold of the field space manifold, $N \subset M$.[2] The submanifold is a patch of field space, bounded by four curves. Two of these are simply the original soliton curves (traced out in field space) that we are colliding, since $\Phi^i(\xi, -\infty) = f^i(\xi)$ for $\xi \in \mathbb{R}$, and $\Phi^i(\infty, \eta) = h^i(-\eta)$ for $\eta \in \mathbb{R}$. Significant insight is gained by viewing Φ^i as the coordinates of two sets of integral curves– those of one set obtained by varying the first argument and fixing the second, and those of the second set obtained by fixing the first argument and varying the second. Let us name the two vector fields these sets of integral curves define as

[2]Technically Φ^i should be viewed as a map from the square $[-s/2, s/2]^2$ in the limit that $s \to \infty$, with boundary conditions given on the edges of the square defined by $(\xi, \eta) = (\xi, -s/2)$ for $\xi \in [-s/2, s/2]$, and $(\xi, \eta) = (s/2, \eta)$ for $\eta \in [-s/2, s/2]$.

follows,

$$U \equiv \frac{\partial}{\partial \xi} = \frac{\partial \Phi^i(\xi,\eta)}{\partial \xi} e_i|_{\Phi(\xi,\eta)} \tag{3.1.30}$$

$$W \equiv \frac{\partial}{\partial \eta} = \frac{\partial \Phi^i(\xi,\eta)}{\partial \eta} e_i|_{\Phi(\xi,\eta)} \tag{3.1.31}$$

where we've expanded in the coordinate basis $\{e_i\} = \{\frac{\partial}{\partial \Phi^i}\}$. Expressed in terms of the vector fields U and W, the boundary conditions for Φ^i simply indicate that the vector fields at the relevant two edges of the submanifold line up with the tangent vectors to the two original soliton curves. In an effort to minimize confusion with the negative signs, we explicitly point out where the vacuum locations are in the submanifold, parameterized by ξ and η: $\Phi(\infty,-\infty) = A$, $\Phi(-\infty,-\infty) = B$, and $\Phi(\infty,\infty) = C$.

The differential equation takes the form,

$$\begin{aligned} 0 = \frac{\partial^2 \Phi^i}{\partial \eta \partial \xi} + \Gamma^i_{j\,k} \frac{\partial \Phi^j}{\partial \xi} \frac{\partial \Phi^k}{\partial \eta} &= \frac{\partial U^i}{\partial \eta} + \Gamma^i_{j\,k} U^j \frac{\partial \Phi^k}{\partial \eta} \\ &= \frac{\partial \Phi^\ell}{\partial \eta} \frac{\partial}{\partial \Phi^\ell} U^i + \frac{\partial \Phi^k}{\partial \eta} U^j \Gamma^i_{j\,k} \\ &= \frac{\partial \Phi^\ell}{\partial \eta} \left(e_\ell[U^i] + U^j \Gamma^i_{j\,\ell} \right) \\ &= W^\ell \left(e_\ell[U^i] + U^j \Gamma^i_{j,\ell} \right) \end{aligned}$$

Since the equality holds for each component we have,

$$\begin{aligned} 0 &= W^\ell \left(e_\ell[U^i] e_i + U^j \Gamma^i_{j\,\ell} e_i \right) \\ &= W^\ell \left(\nabla_{e_\ell} (U^i e_i) \right) \\ &= \left(\nabla_{W^\ell e_\ell} (U^i e_i) \right) = \nabla_W U \end{aligned} \tag{3.1.32}$$

Similarly, we obtain $\nabla_U W = 0$ by the analogous series of steps (when ξ and η are swapped, since 3.1.26 is symmetric under exchange of these). We thus arrive

at the geometrical description of bubble collisions in the ultrarelativistic limit: the resulting field profiles post-collision are determined by the mutual parallel transport of each soliton's tangent vector field along that of the other soliton. That is, the tangent vector fields of the soliton profiles are parallel transported along each other everywhere in N.

The remaining two curves that together with $\Phi^i(\xi, -\infty)$, and $\Phi^i(\infty, \eta)$ form the boundary of N are simply $\Phi^i(\xi, \infty)$ and $\Phi^i(-\infty, \eta)$. The first of these, $\Phi^i(\xi, \infty)$, goes between C^i when $\xi = \infty$, and the point $\Phi^i(-\infty, \infty) \equiv D^i$. The second, $\Phi^i(-\infty, \eta)$, has endpoint B^i when $\eta = \infty$, and the other at D^i as well, when $\eta = -\infty$. This is shown schematically in figure 3.2.

This result agrees with heuristic expectations motivated by the flat field space limit. Namely, note that in the flat limit, a right moving soliton that interpolates between the parent vacuum A and a local minimum B leaves in its wake (to the left of the soliton's transition wall) a field value shifted by $\Delta_L = B - A$, while a left moving soliton that interpolates between the parent vacuum A and a local minimum C leaves in its wake (to the right of the soliton's transition wall) a field value shifted by $\Delta_R = C - A$. Thus, after free passage collision, the collision region – which, by definition is to the left of the right-mover and to the right of the left-mover – is shifted by $\Delta_L + \Delta_R$ (which equals $B + C - 2A$). In the case of curved field space, we divide the field shifts, both Δ_L and Δ_R, into infinitesimals, which geometrically are the tangent vector fields of the soliton field profiles. Each such infinitesimal leaves in its immediate wake a field whose value is parallel transported along the infinitesimal shift vector, thus resulting in the geometrical picture we've described. When all tangent vectors of nontrivial magnitude have been mutually transported, they leave a widening interior of field in $\phi = D$.

This type of reasoning indicates that 3.1.32 is the simplest partial differential equation that reduces to free passage in the flat field space limit. Namely, in the flat

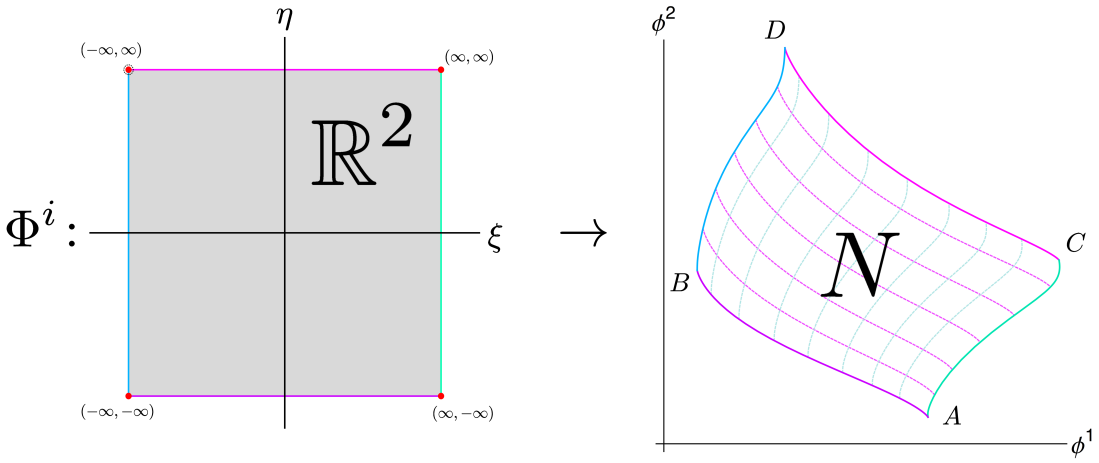

Figure 3.2: The soliton collision initial value problem expressed in the Lorentz variables takes the form 3.1.26, with 3.1.27, 3.1.28 when the limit that the impact velocity goes to 1 is taken. The solution to this limiting set of equations, denoted by Φ^i, maps $\mathbb{R}^2$ to a submanifold N of the field space M. Since the map is smooth the images of the ξ coordinate lines and the η coordinate lines are the integral curves of two vector fields. The partial differential equation 3.1.26 indicates these two vector fields are parallel transported along one another everywhere in N. The initial conditions require that $\Phi(\xi, \eta)$ go to $f(\xi)$ as $\eta \to -\infty$, and go to $h(-\eta)$ as $\xi \to \infty$. This is shown in the schematic illustration above, where $\mathbb{R}^2$ is drawn as a (finite) square. The purple horizontal line in the lower half of the ξ-η plane is mapped to the purple curve with endpoints at B and A in the $\{\phi^i\}$ coordinate plane(f soliton), and the green vertical line in the right half plane is mapped to the green curve with endpoints C and A (h soliton). The remaining two curves that form the rest of the boundary of N are shown in blue and pink. They are the images of the ξ coordinate line at $\eta \to \infty$ and the η coordinate line at $\xi \to -\infty$. These are, in a sense, the curves obtained by completing the transport of h along f and f along h. At sufficiently high impact velocity the field in the collision region takes on value D, and the outgoing walls interpolate between D and the original bubble vacua, B to the right and C to the left. For such a collision the parametric plot of the two walls differs negligibly from the prediction via parallel transport– the blue and pink curves.

limit, the infinitesimal description of free passage is clearly the requirement that the vanishing of the directional derivatives of U with respect to W and W with respect to U. The covariant version of these statements is just 3.1.32. This heuristic argument is suggestive but not sufficient since it is insensitive to any terms in the limiting form of the partial differential equation that vanish in the flat field space limit but which could nonetheless be present in the curved case. The analysis we've performed so far, together with that in the following section verifies that there are no such terms.

It is worth confirming that our free passage field configuration, 3.1.29, does indeed have the qualitative features outlined above. First note that the configuration correctly approaches the B vacuum asymptotically to the left, and the C vacuum to the right for any finite time t, since this amounts to evaluating Φ at $(\gamma(x-ut), \gamma(x+ut)) \to (-\infty, -\infty)$, and (∞, ∞), respectively. At a fixed time *before* collision, any time $t \lesssim -w/2\gamma u$, the free passage field differs from B vacuum by an insignificant amount at $x < ut - w/2\gamma$ since we'd effectively be evaluating Φ^i in 3.1.29 at $(-\infty, -\infty)$. As we march rightward the first argument increases, and reaches zero at $x = ut$ while second argument remains essentially unchanged. $\Phi(0, -\infty)$ is simply the center of the f soliton. So, as one moves between the positions $-ut - w/2\gamma u$, and $-ut + w/2\gamma u$ in free passage field configuration they run through the f soliton's field configuration. If they continue moving rightward they'll reach a stretch of x values where both the arguments of Φ^i in 3.1.29 are effectively negative infinity, and so the A vacuum is measured.

If we continue on rightward the analogous procedure leads us to realize that the free passage field configuration interpolates between the A and C vacua by the (reflected) h soliton, centered at $-ut$. So, pre-collision the spatial profile of the free passage field configuration looks like the usual linear superposition: a nearly homogeneous interior of diminishing size in the parent vacuum, separated from the bubble vacua by the relevant solitons, whose centers lie at ut, and $-ut$.

The same line of reasoning can be used to deduce that post-collision, any time $t \gtrsim w/2\gamma u$, the free passage configuration again consists of three approximately homogeneous regions: a widening interior, or "collision region" with field components $\approx D^i$, separated from regions of original bubble vacua on either side, by walls whose centers follow the same trajectories $x = \pm ut$. The shapes however of the spatial profiles of the field components across the walls are *not* in general the same as those of the incoming solitons. A parametric plot of the free passage configuration at a given time (with the spatial variable as the parameter) in the $\{\phi^i\}$ coordinate plane would consist of the composition of a curve that interpolates between B and D, together with the one between C and D. These would be nearly identical those obtained by completing parallel transport, and approaches the union of these two curves, $\Phi^i(-\infty, \infty)$, and $\Phi^i(\infty, \infty)$ asymptotically as $t \to \infty$.

We claim that there always exists an impact velocity sufficiently close to the speed of light such that the actual solution to 3.1.7 is well approximated by the above free passage evolution throughout the entirety of the collision– i.e. for longer than the amount of time it would take for the incoming Lorentz contracted walls to fully pass through each other. We prove this in the following section.

3.2 Realization of Free Passage

The solution to the parallel transport problem, Φ^i, and the free passage evolution function defined from it, ϕ^i_{FP}, is, of course, only useful in predicting the outcome of a particular collision if deviations from ϕ^i_{FP} remain sufficiently small throughout the entirety of the collision (or longer). As we've mentioned previously, the amount of time it takes the solitons to fully pass through each other is $w/\gamma u$, and since we've chosen to set our $t = 0$ at the middle of the collision we're interested in the time period, $t \in [-w/2\gamma u, w/2\gamma u]$.

We begin by expanding the actual solution (to 3.1.7) about the free passage configuration,

$$\phi^i(t,x;u) = \phi^i_{FP}(t,x;u) + \psi^i(t,x;u) \tag{3.2.1}$$

Simply substituting 3.2.1 into the equation of motion and expanding in powers of ψ yields,

$$\begin{aligned}\Box\psi^i &= -\frac{\partial V}{\partial\phi_i}\bigg|_{\phi_{FP}} - \frac{\partial^2 V}{\partial\phi^\ell\partial\phi_i}\bigg|_{\phi_{FP}}\psi^\ell + \mathcal{O}(\psi^2) - \left[\Box\phi^i_{FP} + \Gamma^i_{jk}|_{\phi_{FP}}\partial_\mu\phi^j_{FP}\partial^\mu\phi^k_{FP}\right] \\ &\quad - 2\Gamma^i_{jk}|_{\phi_{FP}}\partial_\mu\phi^j_{FP}\partial^\mu\psi^k - \Gamma^i_{jk,\ell}|_{\phi_{FP}}\psi^\ell\partial_\mu\phi^j_{FP}\partial^\mu\phi^k_{FP} + \mathcal{O}(\psi(\partial\psi)) + \mathcal{O}((\partial\psi)^2) \\ &= -\frac{\partial V}{\partial\phi_i}\bigg|_{\phi_{FP}} - \left[\Box\phi^i_{FP} + \Gamma^i_{jk}|_{\phi_{FP}}\partial_\mu\phi^j_{FP}\partial^\mu\phi^k_{FP}\right] + \mathcal{O}(\psi)\end{aligned} \tag{3.2.2}$$

We can write an implicit expression for $\psi^i(t,x)$ by integrating the right hand side of 3.2.2 as follows,

$$\psi^i(t,x) = \int_{-w/2\gamma u}^{t} dt' \int_{x-t'}^{x+t'} dx' G^i(t',x') \tag{3.2.3}$$

We now truncate at zeroth order in ψ, and bound the above integral. The term in the square brackets in 3.2.2 is,

$$\begin{aligned}-\left[\Box\phi^i_{FP} + \Gamma^i_{jk}|_{\phi_{FP}}\partial_\mu\phi^j_{FP}\partial^\mu\phi^k_{FP}\right] &= 4(1-\epsilon)\gamma^2\left[\frac{\partial^2\Phi^i}{\partial\sigma\partial\omega} + \Gamma^i_{j\,k}\frac{\partial\Phi^j}{\partial\sigma}\frac{\partial\Phi^k}{\partial\omega}\right] \\ &\quad - 2\gamma^2\epsilon\left[\frac{\partial^2\Phi^i}{\partial\sigma^2} + \frac{\partial^2\Phi^i}{\partial\omega^2} + \Gamma^i_{j\,k}\left(\frac{\partial\Phi^j}{\partial\sigma}\frac{\partial\Phi^k}{\partial\sigma} + \frac{\partial\Phi^j}{\partial\omega}\frac{\partial\Phi^k}{\partial\omega}\right)\right]\end{aligned} \tag{3.2.4}$$

where we've expressed the operators $\Box$ and ∂_μ in terms of the the Lorentz variables, and retained terms up to first order in ϵ. This is identical to the step we took at the outset to obtain 3.1.14. Note that the first term in square brackets on the righthand side of 3.2.4 is, by definition, zero.

The second term, however, does not vanish. It results from the mismatch between the Lorentz variables and the characteristics. The nonvanishing piece can be

expressed in terms of the vector fields U and W as follows,

$$-2\gamma^2\epsilon\left[\frac{\partial^2\Phi^i}{\partial\sigma^2}+\Gamma^i_{j\,k}\frac{\partial\Phi^j}{\partial\sigma}\frac{\partial\Phi^k}{\partial\sigma}+\frac{\partial^2\Phi^i}{\partial\omega^2}+\Gamma^i_{j\,k}\frac{\partial\Phi^j}{\partial\omega}\frac{\partial\Phi^k}{\partial\omega}\right]=-2\gamma^2\epsilon\left[(\nabla_U U)^i+(\nabla_W W)^i\right]$$

A bound on the magnitude of ψ^i can now be computed straightforwardly,

$$|\psi^i(t,x)|\leq\int_{-w/2\gamma}^{t}dt'\int_{x-t'}^{x+t'}dx'|G^i(t',x')| \tag{3.2.5}$$

$$\leq\int_{-w/2\gamma}^{t}dt'\int_{x-t'}^{x+t'}dx'\left|\frac{\partial V}{\partial\phi_i}\right|+2\gamma^2\epsilon\left|(\nabla_U U)^i\right|+2\gamma^2\epsilon\left|(\nabla_W W)^i\right| \tag{3.2.6}$$

where the terms involving the vector fields are evaluated at $(\gamma(x'-ut'),\gamma(x'+ut'))$. Now, we're only interested in the deviation at points x in the collision region (outside of here the field persists very nearly equal to the bubble vacuum field values), and times $t\in[-w/2\gamma u,+w/2\gamma u]$. For this time period the collision region is always contained within $[-w/\gamma,+w/\gamma]$. This means the x' interval we need to integrate over in our expression for $\psi^i(t,x)$ is always contained within $[-3w/2\gamma,+3w/2\gamma]$. So we can write,

$$|\psi^i(t,x)|\leq\int_{-w/2\gamma}^{t}dt'\int_{-3w/2\gamma}^{3w/2\gamma}dx'|G^i(t',x')| \tag{3.2.7}$$

$$\leq\left\{\sup_{\phi\in N}\left(\left|\frac{\partial V}{\partial\phi_i}\right|\right)+2\gamma^2\epsilon\sup_{(\sigma,\omega)\in\mathbb{R}^2}\left(\left|(\nabla_U U(\sigma,\omega))^i\right|+\left|(\nabla_W W(\sigma,\omega))^i\right|\right)\right\}\int_{-w/2\gamma u}^{t}dt'\int_{-3w/2\gamma}^{3w/2\gamma}dx'$$

$$=(k_1^i+2\gamma^2\epsilon k_2^i)\frac{w(t/T+1/2)}{\gamma u}\frac{3w}{\gamma}$$

$$=\left(\frac{k_1^i}{\gamma^2}+2\epsilon k_2^i\right)3w^2=\left(2\epsilon k_1^i+2\epsilon k_2^i\right)3w^2$$

So,

$$|\psi^i(t,x)|\leq k^i\epsilon \tag{3.2.8}$$

where the positive constants,

$$k^i \equiv 6w^2 \left\{ \sup_{\phi \in N} \left(\left| \frac{\partial V}{\partial \phi_i} \right| \right) + 2\gamma^2 \epsilon \sup_{(\sigma,\omega)\in\mathbb{R}^2} \left(\left| \left(\nabla_U U(\sigma,\omega)\right)^i \right| + \left| \left(\nabla_W W(\sigma,\omega)\right)^i \right| \right) \right\}$$

are finite due to the smoothness of the potential and the field space manifold.

Since the difference in the coordinates of the true field configuration and free passage configuration can be made arbitrarily small, we conclude that the post collision field (for any two solitons in any curved multi-scalar field theory) successfully realizes the late-time free passage field configuration, provided the impact velocity was sufficiently relativistic. The threshold above which the impact velocity ought to be is dependent on both the model and the choice of the two colliding solitons. This threshold can be estimated by requiring that the distance in field space between the free passage field (say for the center of the collision region) at time t, and the free passage plus deviation location be much much smaller than the length of the path the observer at the center of the collision region has through field space from the parent vacuum until time t. Since the walls of bubbles nucleated via Coleman-De Luccia tunneling accelerate as they move outwards, we expect our parallel transport procedure to be a useful means of predicting the field configuration following the collision of two bubbles, provided they were nucleated sufficiently far apart (and they're radii upon nucleation is sufficiently small compared to the separation distance such that high enough impact velocity is reached upon collision).

3.3 Numerical Simulations

We simulated soliton collisions at a variety of impact velocities in three different models with actions of the form 3.1.1. Each model featured a different two dimensional curved field space. We reiterate that the field space is curved in the sense that the matrix of $\{\phi^i\}$ dependent functions, g^{ij}, in the noncanonical kinetic term in the La-

Table 3.1: Metric Components and Vacuum Locations

Geometry	g^{ij}	Parent and Bubble Vacua			Free Passage
		A	B	C	D
Sphere	$g_{\theta\theta} = 1$ $g_{\phi\phi} = \sin^2(\theta)$	$(\frac{\pi}{12}, \frac{2\pi}{15})$	$(\frac{5\pi}{12}, \frac{2\pi}{11})$	$(\frac{3\pi}{12}, \frac{6\pi}{13})$	(1.77,1.08)
Teardrop	$g_{\theta\theta} = \cos^2(\theta)$ $+\left(\frac{\sin(\theta)}{2} + (\theta - \pi)\right)^2$ $g_{\phi\phi} = \sin^2(\theta)$	$(\frac{7\pi}{60}, \frac{\pi}{13})$	$(\frac{118\pi}{327}, \frac{-\pi}{13})$	$(\frac{73\pi}{327}, \frac{35\pi}{109})$	(1.52,0.33)
Torus	$g_{uu} = (1+.7\cos(v))^2$ $g_{vv} = .7^2$	$(\frac{145\pi}{654}, \frac{-20\pi}{109})$	$(\frac{-145\pi}{654}, \frac{20\pi}{109})$	$(\frac{-35\pi}{654}, \frac{235\pi}{654})$	(1.36,0.09)

grangian is the coordinate representation of the metric on a curved manifold (clearly the field components $\{\phi^i\}$ are identified as coordinates on the manifold). The particular manifolds we considered were the sphere, the ring torus, and the "teardrop"– our own creation named for obvious reasons.

For both the sphere and teardrop we used the polar angle and azimuthal angle as our two coordinates. For the torus we used the angles about the major axis, and the minor axis. To minimize the possibility for confusion we adopt standard naming conventions used for these coordinate systems, and refer to the field components (ϕ^1, ϕ^2) as (θ, ϕ) for the sphere and teardrop, and as (u, v) for the torus. For the explicit form of the metric components, as well as vacuum locations refer to table, 3.1.

We numerically approximated the solutions to the initial value problem 3.1.7 associated with the collision of two non-identical solitons in the given theory, as well as solutions to the mutual parallel transport of two tangent vector fields problem, 3.1.26-3.1.28, using Mathematica's finite difference partial differential equation solver, NDSolve. The potential was engineered to have three degenerate vacua with generic

looking wells and barriers by using the product of two trigonometric functions, and then isolating only three minima by multiplying by a superposition of hyperbolic tangents which served as smooth approximations to characteristic functions and hat functions. For the explicit form of the three potentials see table 3.2.

We wanted the potential to be flat outside the neighborhood immediately surrounding the three vacua so as to minimize the influence of the potential on field dynamics, both throughout the collision and after, so that the free passage behavior could feasibly be extracted. Though we absolutely assert that parallel transport is generic (there always exists a speed high enough such that it is fully realized), we wanted to design a nontrivial scenario where the boost needed was small enough, and so the grid size large enough, that we'd have a hope of resolving this in Mathematica, and on a desktop computer. There is a final step to designing a potential that enables us to extract the free passage dynamics– the placement of a fourth degenerate

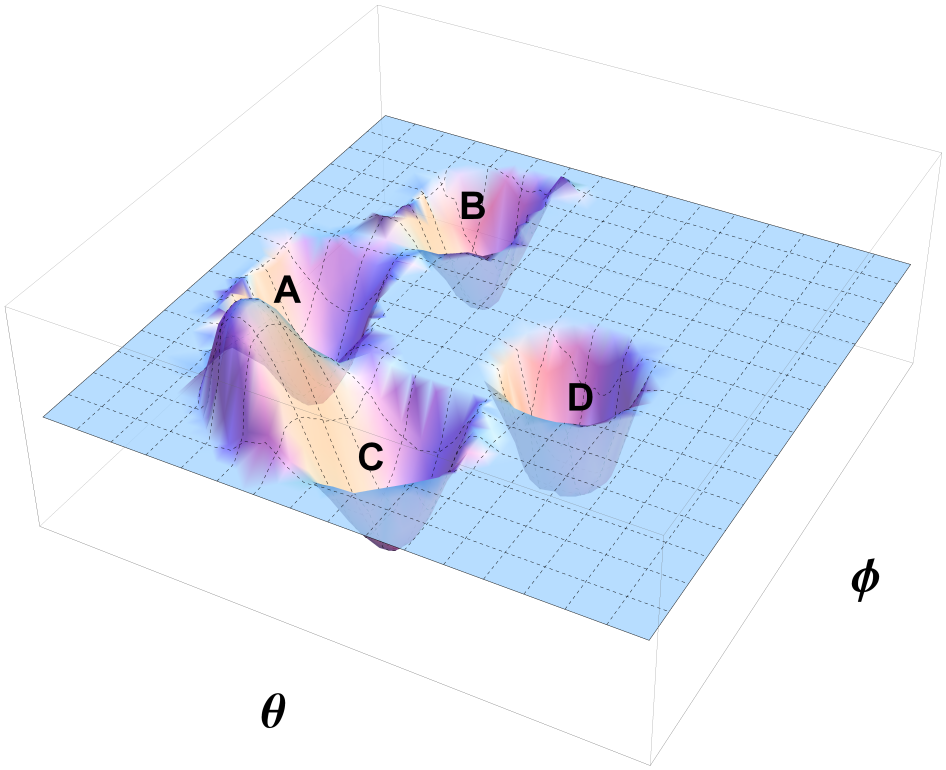

Figure 3.3: Plot of the potential for the teardrop model. Note the cylindrical well carved out of the plateau at D. This addition does not change the solitons f, and h.

vacuum at the free passage location D which of course is not known a priori. Had the potential been left as a plateau outside the three vacua the post collision field dynamics would be tainted by the pressure gradient across outgoing walls resulting from the energy density in the collision region differing from that in the surrounding region (which is still simply that of the degenerate bubble vacua). In order to prolong the amount of time after which free passage would remain a good approximation, without unduly biasing the field toward the free passage field location we carved a cylindrical well out of the plateau at the free passage field location, for each model. Clearly then, the parallel transport solution for each geometry was obtained before any collisions were simulated, so that each of their potentials could be modified in the manner described.

Note that the parallel transport solution Φ is by definition independent of the potential provided that the soliton curves between the parent and two bubble vacua remain unchanged (since these are the boundary conditions in the parallel transport problem). Clearly the potential in the neighborhood of the three original vacua is unaffected by the addition of the narrow cylindrical well placed out on the plateau away from the original three vacua. A plot of the potential in the teardrop model is included as an example in figure 3.3, and the explicit form of the potentials used for all three geometries can be found in table 3.2.

Lastly it is necessary to discuss how the initial conditions and boundary conditions were formulated. Both are defined in terms of the components of the two solitons we are colliding. Solitons are, by definition, static solutions to the equations of motion 3.1.2 that approach two distinct (obviously degenerate) minima of the potential asymptotically. In a multi-scalar field theory solitons are unique to the vacua they interpolate between, and furthermore are the minimum energy field configurations that satisfy the given pair of boundary conditions. Since the coupled ordinary differential equations that define the solitons are nonlinear, analytic solutions generally

Table 3.2: Below is the explicit form of the potentials we used in our simulations of solitons collisions for each of the field space geometries we considered.

Model	Potential
Sphere	$V(\theta,\phi) = V_0 \sin(6\theta)\sin\left(\frac{(3\theta-4\pi)\phi}{\pi}\right)\chi_{\text{sphere}}(\theta,\phi)$ $- \frac{V_0}{2}\tanh(40((\theta-D_\theta)^2+(\phi-D_\phi-.3)^2))+2.5)$ $+ \frac{V_0}{2}\tanh(40((\theta-D_\theta)^2+(\phi-D_\phi-.3)^2)-2.5)$
Teardrop	$V(\theta,\phi) = V_0 \sin(4\phi-1.2\theta+.3\pi)\sin(6\theta-1.5\pi+1.8\phi)\ \chi_{\text{tear}}(\theta,\phi)$ $- \frac{V_0}{2}\left[\tanh(2.7-60(((\theta-D_\theta)^2+(\phi-D_\phi)^2)))+1\right]$
Torus	$V(u,v) = V_0 \sin(2v-.6u)\sin(3u+.9v)\ \chi_{\text{torus}}(u,v)$ $- \frac{V_0}{2}\left[\tanh(3-30((u-D_u)^2+(v-D_v)^2)))+1\right]$
	$\chi_{\text{sphere}}(\theta,\phi) = (1-\tanh((\theta-.25\phi-5\pi/12-.2)30)))$ $(1-\tanh((\phi+1.5\theta-3.2)30))/4$
	$\chi_{\text{tear}}(\theta,\phi) = \frac{1}{2^6}(1+\tanh[40(-0.05+(-1.56+u)^2+(0.06+v)^2)])$ $*(1+\tanh[20(-0.5+(-2.42+2u)^2+(-2.3+2v)^2)])$ $*(1+\tanh[20(-0.75+(-0.07+2u)^2+(-2+2v)^2)])$ $*(1+\tanh[10(-3.2+(-3.87+2u)^2+1/2(-1.9+2v)^2)])$ $*(1+\tanh[20(-1+(-2.27+2u)^2+(-1+2v)^2)])$ $*(1+\tanh[10(2.1-(-1.77+2u)^2-1/2(-0.8+2v)^2)])$
	$\chi_{\text{torus}}(u,v) = \frac{1}{2^6}(\tanh(10(2.1-(v-.8)^2/2-(u-.2)^2))+1)$ $*(1-\tanh(30((.15v+u)-.9)))$ $*(\tanh[10((v-1.9)^2/2+(u-2.3)^2-3.2)]+1)$ $*(\tanh[20((v-1)^2+(u-.7)^2-1.2)]+1)$ $*(\tanh(20((v-2.3)^2+(u-.85)^2-.5))+1)$ $*(\tanh[20((v-2)^2+(u+1.5)^2-.75)]+1)$

cannot be found. However, if an initial profile that satisfies the boundary conditions is evolved in time by the equations of motion plus a damping term, the profile ultimately settles down to the soliton, provided the initial guess was sufficiently close to the true soliton and the damping coefficient was not too large. We performed this relaxation procedure numerically, once again with NDSolve in Mathematica.[3]

Note that analytic expressions for the four soliton components, f^i, and h^i, were needed in order for simulations of the collision to be feasible. At such small grid spacing time evolving initial conditions constructed out of the interpolating functions relaxation yielded was not possible. So the final step was to engineer analytic expressions that approximated each of the soliton components from relaxation (four total, f^1, f^2, h^1, h^2). All were modifications of (scaled and shifted) hyperbolic tangents, typically with the addition of small gaussians and nonlinear terms in the argument of the hyperbolic tangent.

The free passage field configuration was indeed fully realized in all three models at sufficiently large impact velocity. Snapshots of the spatial profile of each field components during such collisions can be found in figures 3.4. Note that each field

[3]It is important to mention how the initial guesses for the soliton components in relaxation were chosen. Since the (true) soliton is defined by both the geometry and the potential, we sought to allow both to play a role in our guesses. For a given pair of vacua we first parameterized the geodesic connecting them by writing one field component in terms of the other (for instance, in the case of the sphere the geodesics were great circles and the polar angle was parameterized in terms of the azimuthal). The potential was then evaluated along the geodesic, and the resulting function was approximated as a double well potential, which has a single free parameter after the distance between the minima is fixed. This parameter was tuned such that the approximate potential not only qualitatively resembled the true one along the geodesic, but also so that their integrals of the inverse square root of the difference between the vacuum value, $-V_0$, and the potential, between the minima were nearly identical for the. For example, for the sphere initial guess we'd compute

$$\int_{\phi_A}^{\phi^B} d\phi / \sqrt{V_{\text{sphere}}(c_{\text{geo},AB}(\phi), \phi) + V_0} \tag{3.3.1}$$

numerically and tune the double well potential's curvature parameter until its integral matched this. The double well approximation then provides us with an initial guess, a (scaled and shifted) hyperbolic tangent, for one of the two soliton components– that which the geodesic is parameterized in terms of. To obtain a guess for the remaining component the expression for the geodesic was simply evaluated at the guess function that was just obtained for the former component– resulting in a spatial profile.

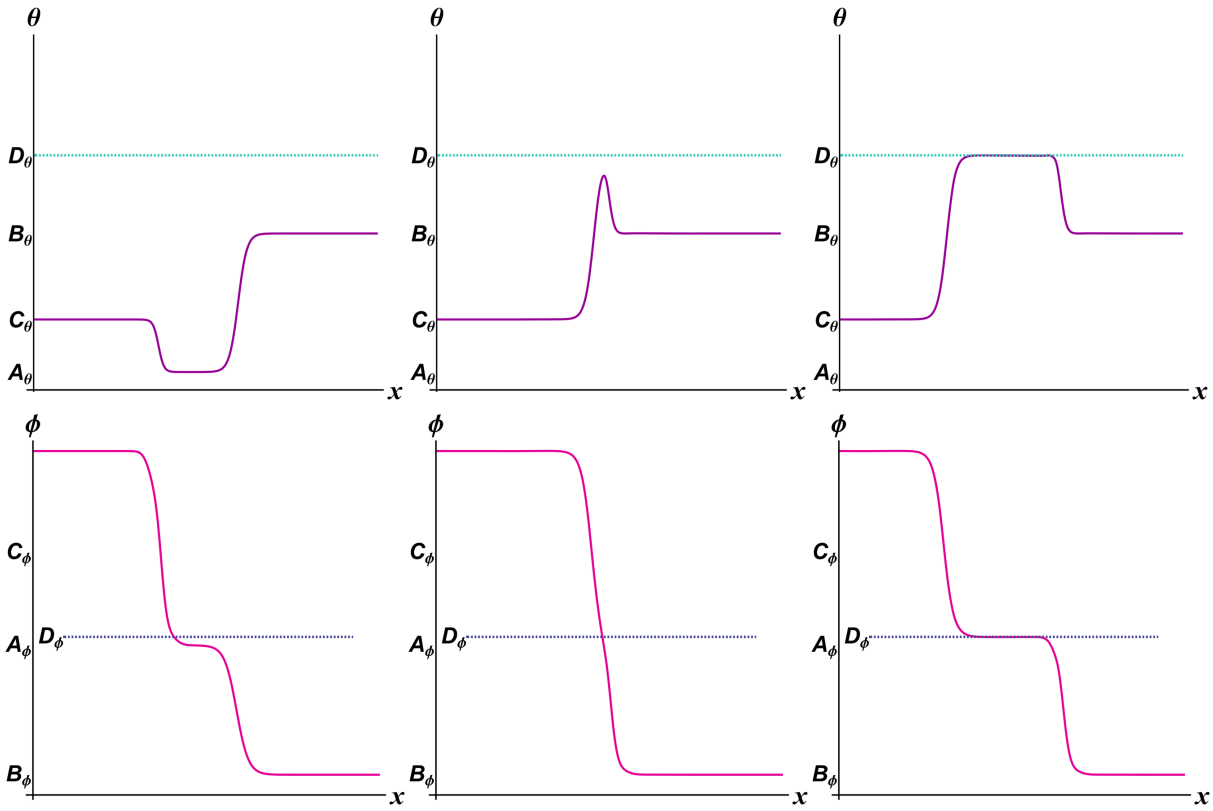

Figure 3.4: Here we show snapshots of each field component of the configuration during a collision simulated in the teardrop model at impact velocity $u = .995$ (the θ component is on the top row, and the ϕ on the bottom row). The prediction of each component's value inside the collision region obtained by parallel transport, D^i are indicated by the dashed teal and purple horizontal lines for θ, and ϕ, respectively. Note both the homogeneity of the field in the collision region, and its extraordinarily strong agreement with the free passage prediction.

component's collision region is homogenous, with the precise value predicted by the parallel transport solution, indicated by the contrasting dashed line. Furthermore, the shapes of the outgoing soliton profiles matched the prediction as well, as shown in figures 3.5, 3.6, and 3.7.

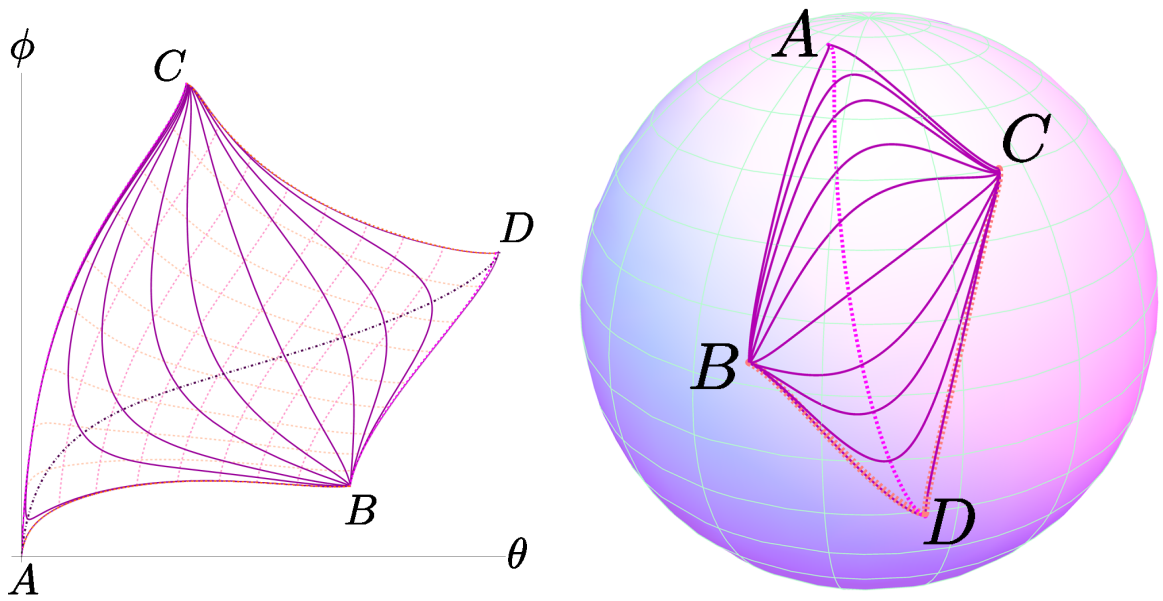

Figure 3.5: A comparison the results of a collision at impact velocity $u = .995$ in the sphere model with the prediction from parallel transport. On the left we plot the field configuration at various times throughout the collision parametrically in the $\{\phi^i\}$ coordinate plane (by treating the spatial variable as the parameter) with solid purple curves. We identify the field at the origin, $x = 0$, throughout the collision with the dot-dashed dark purple line. This is the path taken through field space over the course of the collision by an observer at the center of the collision's rest frame. The solution to the parallel transport problem is shown with dashed lines. Those in pink are lines of constant η, those in orange are lines of constant ξ, i.e. the integral curves of the vector fields U and W. The curves that form the boundary of the submanifold are drawn brighter and are overlaid so that they can easily be compared to the results of the collision. On the right these results are plotted on the field space manifold embedded in three space (the $\{\phi^i\}$ coordinate lines are shown in light green). The field configuration in the collision problem is again shown in solid purple for a variety of times. The post collision prediction made by parallel transport (that is, the integral curves obtained by completing the parallel transport procedure which yields the remaining two curves that form the boundary of N) are shown in dashed orange. The path taken through field space by an observer at the origin is shown in dashed pink. The fact that the boundary of N lines up nearly perfectly with the parametric plots of the initial and final field configuration in the collision problem indicates that there is extraordinarily good agreement between the prediction, computed via parallel transport, and the actual outcome of the collision.

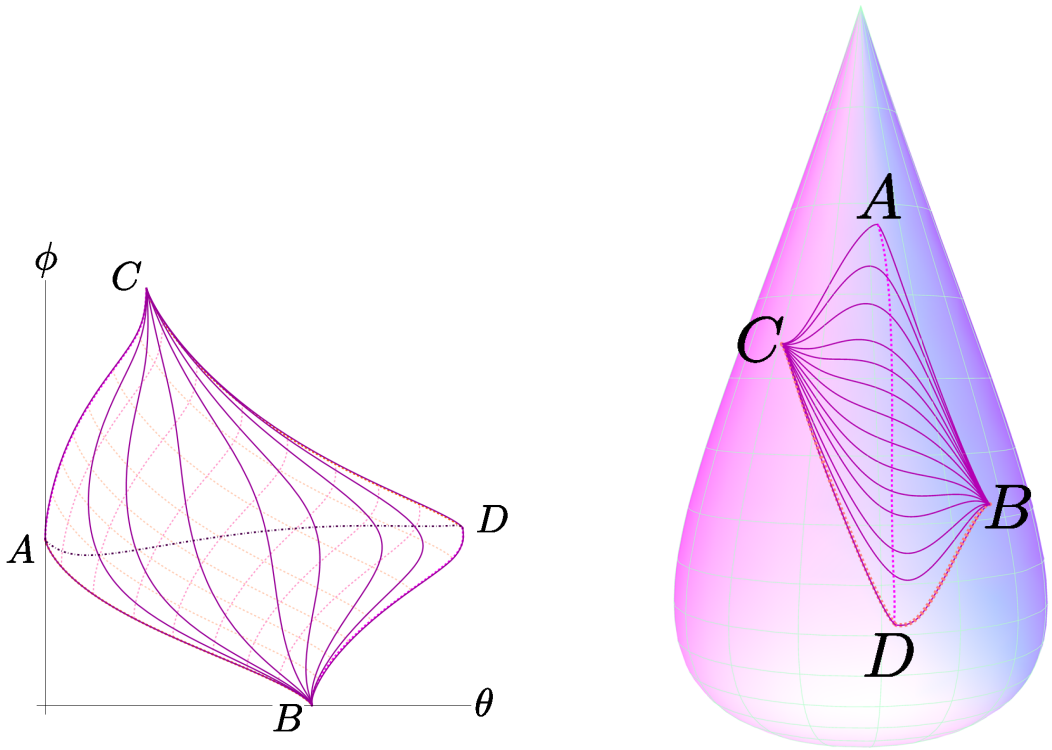

Figure 3.6: Comparison of the results of a collision simulation at impact velocity $u = .995$ in the teardrop model with the prediction from parallel transport. The same coloring scheme is the same as that in figure 3.5.

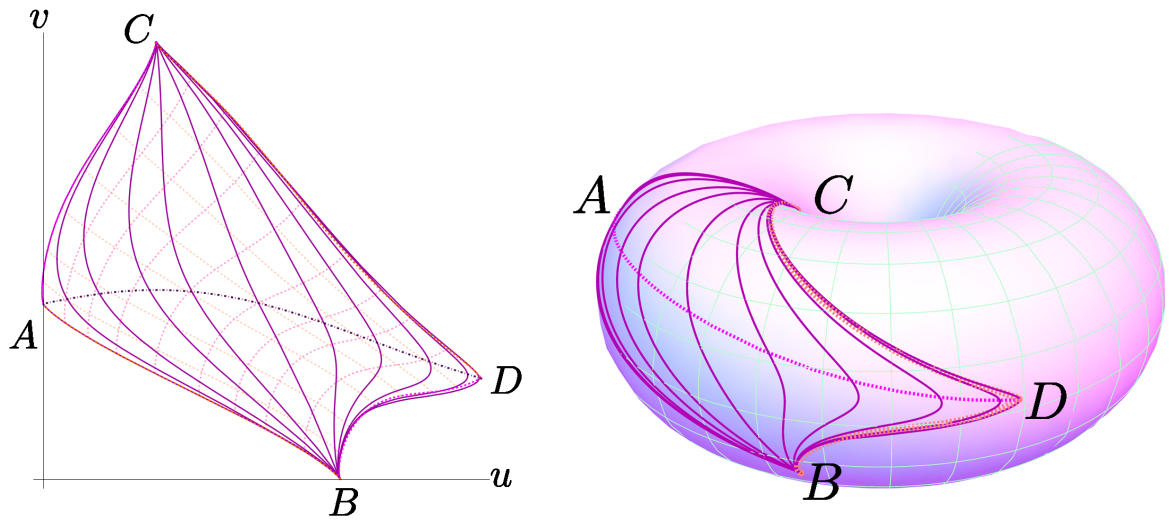

Figure 3.7: Comparison of the results of a collision simulation at impact velocity $u = .985$ in the torus model with the prediction from parallel transport. The same coloring scheme is the same as that in figure 3.5.

Chapter 4

Vacua In The Mirror Quintic Moduli Space

An accessible setting conducive to making progress on these issues is offered by compactifying type IIb supergravity on the mirror quintic — a particular Calabi-Yau notable for its single complex structure modulus and the well-understood moduli space associated with it. Of course, this feature is only beneficial from the standpoint of tractability if the manifold's 101 Kähler moduli in some sense separate from the complex structure at level of effective action, and thus enable the latter's stability to be analyzed independently from the former.

The large volume limit accomplishes precisely this. Without going into too much extraneous detail, the key is that the classical expressions for the Gukov-Vafa-Witten superpotential and Kähler potential for the Kähler moduli (which otherwise would receive both α' and g_s corrections) are valid in this regime. Backreaction of fluxes on the compact geometry is also suppressed. Consequently, the holomorphic superpotential, is independent of the Kähler moduli. Since it is defined as the integral of the wedge product of the total 3-form flux with the Calabi-Yau's holomorphic 3-form, the superpotential is given by a linear combination of the Calabi-Yau's *period integrals*. These are the integrals of the holomorphic 3-form over a basis of nontrivial 3-cycles, of which there are $2(h^{(2,1)} + 1) = 4$ in the case of the mirror quintic. Their only dependence is on the complex structure.

An essential feature of one parameter models like the mirror quintic is that the periods are known explicitly in terms of Meijer-G functions. Hence, for effective theories expressed solely in terms of the periods, exact calculations may be carried

out without any reliance on toy models or stand-ins for the Calabi-Yau geometry.

Using an integral and symplectic basis of periods we write the pure flux superpotential, W, as

$$W = W(z,\tau) = \sum_{i=1}^{4}(F_i - \tau H_i)\cdot\Pi_i(z). \tag{4.0.1}$$

where z is the complex structure, τ is the axio-dilaton, and the integer valued parameters F_i and H_i indicate the amount of flux Ramond–Ramond and Neveu-Schwartz–Neveu-Schwartz flux wrapping each of the basis 3-cycles. In [49] we studied the effective field theories arising from the expansion of the scalar potential about near conifold no scale vacua generated by randomly scanning through a large number of 3-form flux configurations; that is by randomly selecting the above eight integers. The characteristics of the ensemble of field theories was analyzed statistically.

Our effective action involved two complex degrees of freedom, z and τ. The ability to set aside the Kähler moduli is a simple consequence of the superpotential's independence from them and the Calabi-Yau special geometry's formula for the Kähler moduli's Kähler potential.

To see this note first that compactification on a generic manifold would yield an effective potential describing the complex scalars $\{\varphi^a\}$ (the axio-dilaton and all moduli parameterizing the internal geometry) with $\mathcal{N}=1$ supersymmetry[1]. In particular,

$$V(\varphi^a) = e^{\mathcal{K}}(\mathcal{K}^{a\bar{b}}D_aW\bar{D}_{\bar{b}}\bar{W} - 3|W|^2) \tag{4.0.2}$$

where D_a denotes the Kähler covariant derivative $D_a = \partial_a + \mathcal{K}_a = \partial_a + (\partial_a\mathcal{K})$. In the special case of a Calabi-Yau there is an exact cancellation between the Kähler moduli's contribution to the term $\sim |DW|^2$ and the $-3|W|^2$ term because the contraction $\mathcal{K}_a\mathcal{K}^a$ with the index running only over Kähler moduli is precisely equal to $+3$.

The action retrieved upon compactifying the 10-dimensional supergravity theory

[1]Orientifold planes must be included in the compactification to satisfy a tadpole condition for the 3-form fluxes. They break the $\mathcal{N}=2$ to $\mathcal{N}=1$ supersymmetry

then takes the form,

$$S_{\text{eff}} = \frac{M_{\text{pl}}^2}{2} \int d^4x \left(\mathcal{K}_{I\bar{J}} \partial_\mu \varphi^I \partial^\mu \bar{\varphi}^J - \frac{M_{\text{pl}}^2}{4\pi \mathcal{V}_0^2} \, e^{\mathcal{K}} \, \mathcal{K}^{I\bar{J}} \, D_I W \, \bar{D}_{\bar{J}} \overline{W} \right) \tag{4.0.3}$$

where capital letter indices take values 0 or 1 corresponding to τ and z, respectively, $\mathcal{K}$ is the sum of the Kähler potentials associated with each, $\mathcal{K}_{I\bar{J}} \equiv \partial_I \partial_{\bar{J}} \mathcal{K}$ is the corresponding Kähler metric on the z-τ field space, and $\mathcal{V}_0$ is the dimensionless volume of the Calabi-Yau (the volume in natural units, namely the string length to the sixth power).

Although $\mathcal{V}_0$ has Kähler dependence, specifically via the combination of Kähler moduli known as the "volume modulus", this only translates to Kähler dependence in the scalar potential at (z, τ) locations where its value is nontrivial. At zeros the potential is flat in the direction of the volume modulus. Thus the stability of these "no scale" minima may be studied in terms of z and τ alone. Such vacuum locations (z, τ) are global minima of the potential. They satisfy the SUSY conditions,

$$D_z W = D_\tau W = 0. \tag{4.0.4}$$

To search for such vacua numerically a "guess" location is required. We chose to target our search near a known accumulation point for vacua — the conifold point. This location in moduli space corresponds to a mirror quintic with one of its 3-cycles shrunken to zero size. It's intersecting partner in a symplectic and integral basis experiences a monodromy transformation, picking up one copy of the shrinking cycle for each revolution around the conifold. This manifests as a logarithm in the period associated with the intersecting partner, a branch point singularity in the period's first derivative, and ultimately divergences in the curvature and Kähler metric $\mathcal{K}_{z\bar{z}}$.

Series expansions of the periods about the confiold enable leading order solutions to 4.0.4 in terms of the set of eight flux integers that specify W to be obtained;

i.e. the calculation of a starting/guess vacuum location for each flux configuration. Our computation proceeded in three major steps — 1. assemble a random sample of flux vacua by drawing the integers $\{F_i, H_i\}$ from a flat measure and employing a numerical search algorithm, 2. evaluate the Taylor coefficients to fourth order of the relevant scalar potential expanded about each vacuum, 3. report the coefficients in the appropriate field coordinates so as to endow the coefficients with physical significance. Though straightforward in principle this computation was riddled with technical obstructions, owing largely to the multiple-valued period associated with the collapsing cycle's the intersecting partner. In an effort to avoid paralyzing the reader with boredom I direct them to [49] for a detailed discussion of these hurdles and the efficient numerical schemes we designed to resolve them.

We found a pronounced hierarchy in the masses and coupling coefficients which was entirely attributable to the proximity of vacua to the conifold point. The complex symmetric matrix of second covariant derivatives, $Z_{IJ} = D_I D_J W$, is useful in expressing the masses. When evaluated at vacua satisfying the SUSY condition it's entries take the form,

$$Z_{IJ} = \mathcal{F}_{IJK}\bar{Z}^{0K}. \tag{4.0.5}$$

in canonically normalized coordinates, where $\mathcal{F}_{IJK}$ are the Yukawa couplings defined in terms of the Calabi-Yau prepotential.

For us there is a single Yukawa coupling, $\mathcal{F}_{111}$, and it diverges at the conifold point. The SUSY conditions imply Z_{00} vanishes resulting in

$$Z = \begin{pmatrix} 0 & Z_{01} \\ Z_{10} & \mathcal{F}_{111}\bar{Z}^{01} \end{pmatrix} = ae^{i\theta}\begin{pmatrix} 0 & 1 \\ 1 & be^{i\delta} \end{pmatrix}, \tag{4.0.6}$$

with a and b real, and $b \gg 1$. The positive definite matrix $Z\bar{Z}$ in turn has one large and one small eigenvalue, Λ_+^2 and Λ_-^2 .

The masses in no scale supergravity theories consist of pairs $m_{i\pm}$ given in terms of the eigenvalues λ_i^2 of the $Z\bar{Z}$ matrix as follows,

$$m_{i\pm}^2 = e^{\mathcal{K}}(\lambda_i \pm |W|)^2. \tag{4.0.7}$$

In our case the divergence in $|\mathcal{F}_{111}|$ at the conifold resulted in a heavy and light mass pair because the superpotential vev was subdominant to Λ_+, but typically greater than Λ_-. The vev of the superpotential was not correlated with either of the parameters that control the magnitude of $\Lambda_\pm$, namely the vacuum-to-conifold distance and the magnitude of the off-diagonal entry in Z. We developed a Random Matrix Model that replicated the mass data accurately, and confirmed our interpretation of the superpotential vev as a random element that slightly clouds the rigid structure imposed by the Yukawa coupling. The naive extension of these hierarchies was found at cubic and quartic order as well, indicating that there are not countervailing effects that subdue the Yukawa coupling's dominance at higher order.

4.1 Background

Review IIb Flux Compactification

The low energy dynamics of the type IIb string is governed by the type IIb supergravity action, which provides our starting point [14],

$$S_{IIb} = \frac{2\pi}{\ell_s^8}\left[\int d^{10}x\sqrt{-g^{10}}R^{10} - \frac{1}{2}\int \frac{d\tau\wedge *d\bar{\tau}}{(\mathrm{Im}(\tau))^2} + \frac{G_{(3)}\wedge *\bar{G}_{(3)}}{\mathrm{Im}(\tau)} + \frac{\tilde{F}_{(5)}^2}{2} + C_{(4)}\wedge H_{(3)}\wedge F_{(3)}\right] + S_{loc}, \tag{4.1.1}$$

where R^{10} is the 10d Ricci Scalar in the Einstein frame, $G_{(3)}$ is the combined 3-form flux,

$$G_{(3)} = F_{(3)} - \tau H_{(3)}, \tag{4.1.2}$$

τ is the axio-dilaton related to the dilaton, ϕ, by

$$\tau = C_{(0)} + ie^{-\phi} \tag{4.1.3}$$

and $F_{(p)}$ and $H_{(3)}$ are obtained from potentials $C_{(p-1)}$ and $B_{(2)}$,

$$F_{(p)} = dC_{(p-1)} \tag{4.1.4}$$

$$H_{(3)} = dB_{(2)}. \tag{4.1.5}$$

This theory can be compactified on a Calabi-Yau 3-fold to yield an effective action for the moduli fields, which describe how the compact manifold Y varies from one spacetime location to another in the four large dimensions. Such parameters are complex valued and change continuously across the given family of Calabi-Yau, so they enter the 4-dimensional theory as complex scalar fields. It is instructive to sketch the derivation of the effective action, and give a very brief review of the geometry of Calabi-Yau moduli spaces. In the process we introduce notation and summarize our strategy for generating an ensemble of random effective field theories. Experienced readers may wish to skip this section.

Calabi-Yau moduli come in two different types: those associated with deformations of the manifold's complex structure, and those associated with deformations of its Kähler form, J. The former are in one-to-one correspondence with elements of the $(2,1)$-de Rham cohomology group, $H^{(2,1)}(Y)$, and the latter with $H^{(1,1)}(Y)$. We denote the dimension of these vector spaces by their Hodge numbers, $h^{2,1}$ and $h^{1,1}$,

respectively.

Complexifying the Kähler form, we deal with a moduli space of complex dimension $h^{(2,1)} + h^{(1,1)}$, itself a Kähler manifold that factors locally into the direct product of two separate Kähler manifolds: one spanned by the complex structure moduli and the other spanned by the complexified Kähler moduli, with Kähler potential of the form,

$$\mathcal{K}^{\text{cs}}(z^1, \ldots, z^{h^{2,1}}) + \mathcal{K}^{\text{kä}}(v^1, \ldots, v^{h^{1,1}}). \tag{4.1.6}$$

Lowercase indices $(a, b, c, ...)$ will refer to Calabi-Yau moduli. They are ordered from 1 to $h^{2,1} + h^{1,1}$ running through all the complex structures first, followed by those of Kähler type. However, their range in certain expressions may be restricted to moduli of one of the two types. Most often this will be obvious from the context, but where there is the possibility for ambiguity we will state which if any moduli are excluded.

The Kähler potential for the complex structure moduli is,

$$\mathcal{K}^{\text{cs}}(z^1, ..., z^{h^{2,1}}) = -\log\left(-i\int_Y \Omega \wedge \bar{\Omega}\right) \tag{4.1.7}$$

where Ω is the holomorphic 3-form of the Calabi-Yau manifold. It can be shown that differentiating Ω with respect to any of the complex structure moduli yields a component proportional to Ω, and a remaining closed $(2,1)$-form. That is,

$$\frac{\partial \Omega}{\partial z^a} = k_a \Omega + \chi_a \tag{4.1.8}$$

with $\chi_a \in H^{(2,1)}(Y)$. In particular the proportionality constant k_a turns out to be,

$$k_a = -\mathcal{K}_a = -\partial_a \mathcal{K}. \tag{4.1.9}$$

This allows us to construct a basis for $H^{(2,1)}$ by acting on the holomorphic 3-form

with a *Kähler covariant* derivative, D_a, whose action on Ω is defined by,

$$D_a\Omega \equiv \chi_a = \partial_a\Omega + \mathcal{K}_a^{\text{cs}}\Omega. \tag{4.1.10}$$

Furthermore, since

$$\int_Y \Omega \wedge \frac{\partial\Omega}{\partial z^a} = 0, \tag{4.1.11}$$

such $(2,1)$-forms are orthogonal to Ω.

We can now compute the term proportional to $G_{(3)} \wedge *\bar{G}_{(3)}$ in the supergravity action upon compactification. This process amounts to taking the 10-dimensional spacetime to be the direct product of a 4-dimensional (noncompact) Lorentzian manifold, M_4, and a compact Riemannian one, Y, which for us is a Calabi-Yau 3-fold. We write,

$$M_{10} = M_4 \times Y(z^1, \ldots, z^{h^{2,1}}, v^1, \ldots, v^{h^{1,1}}), \tag{4.1.12}$$

and perform the integration over Y in the action. Since Y is parameterized by the aforementioned moduli, and since the Calabi-Yau are allowed to vary across locations in M_4, performing the integral over Y will yield an effective field theory involving moduli fields, $\varphi^a(x_\mu)$.

Requiring Poincaré invariance in M_4 implies only $G_{(3)}$'s components with all indices in the compact dimensions may be nontrivial, and so

$$\int_Y G_{(3)} \wedge *\bar{G}_{(3)} = \int_Y G_{(3)} \cdot\ \bar{G}_{(3)}. \tag{4.1.13}$$

This is essentially a norm of a (for now general) closed 3-form on Y. We may expand $G_{(3)}$ and $\bar{G}_{(3)}$ in an orthogonal basis for

$$H^{(3)}(Y) = H^{(3,0)}(Y) \oplus H^{(2,1)}(Y) \oplus H^{(1,2)}(Y) \oplus H^{(0,3)}(Y), \tag{4.1.14}$$

namely,

$$\Omega \ , \ \{\chi_a\}_{a=1}^{h^{2,1}} \ , \{\bar{\chi}_a\}_{a=1}^{h^{2,1}} \quad \text{and} \quad \bar{\Omega} \tag{4.1.15}$$

allowing us to write,

$$\int_Y G_{(3)} \cdot \bar{G}_{(3)} = \frac{i}{\int_Y \Omega \wedge \bar{\Omega}} \left(\int_Y G_{(3)} \wedge \bar{\Omega} \int_Y \bar{G}_{(3)} \wedge \Omega + \mathcal{K}^{a\bar{b}} \int_Y G_{(3)} \wedge \bar{\chi}_a \int_Y \bar{G}_{(3)} \wedge \chi_b \right). \tag{4.1.16}$$

Each of these can be expressed in terms of covariant derivatives of the Gukov-Vafa-Witten superpotential, W, defined in terms of the (3)-form flux as,

$$W(z, \tau) = \int_Y \Omega \wedge G_{(3)}. \tag{4.1.17}$$

The second term on the right hand side of eq. 4.1.16 involves Kähler covariant derivatives of the superpotential with respect to the complex structure moduli (because it is built out of $(2,1)$-forms). It is proportional to,

$$\mathcal{K}^{a\bar{b}} D_a W \bar{D}_{\bar{b}} \bar{W}. \tag{4.1.18}$$

As is standard, we can define a "Kähler potential" for the axio-dilaton such that the first term in on the right hand side of eq. 4.1.16 has the same form as eq. 4.1.18, i.e. so it is $\sim |D_\tau W|^2$. Specifically, we choose

$$\mathcal{K}^{\text{ax}} = -\log(-i(\tau - \bar{\tau})), \tag{4.1.19}$$

and

$$\mathcal{K}^{\text{ax}\,\tau\bar{\tau}} = (\mathcal{K}^{\text{ax}}_{\tau\bar{\tau}})^{-1} = (\partial_\tau \partial_{\bar{\tau}} \mathcal{K}^{\text{ax}})^{-1}. \tag{4.1.20}$$

One makes this choice because

$$\frac{1}{(\bar{\tau}-\tau)}\int G_{(3)}\wedge\bar{\Omega}=\left(\partial_\tau-\frac{i}{\tau-\bar{\tau}}\right)W=\left(\partial_\tau+\partial_\tau\mathcal{K}^{\rm ax}\right)W\equiv D_\tau W, \tag{4.1.21}$$

and so first term in 4.1.16 is proportional to

$$|D_\tau W|^2=\mathcal{K}^{{\rm ax}\tau\bar{\tau}}D_\tau W\bar{D}_{\bar{\tau}}\bar{W}, \tag{4.1.22}$$

which parallels the form arising for the other complex structure moduli, reflecting the relationship of type IIb string theory to F-theory in which the axio-dilaton explicitly becomes another complex structure modulus.

Notationally, to include the axio-dilaton as as additional modulus we use new indices — capital letters — that begin from zero, the index value reserved for the axio-dilaton. We denote the full Kähler potential by $\mathcal{K}$. It is the sum of all three pieces, $\mathcal{K}^{\rm cs}$, $\mathcal{K}^{\rm ax}$ and $\mathcal{K}^{\rm kä}$. The result, then, of dimensionally reducing the 3-form flux term is

$$\frac{2\pi}{\ell_s^8}\frac{i}{2{\rm Im}(\tau)\int_Y\Omega\wedge\bar{\Omega}}\mathcal{K}^{I\bar{J}}D_I W\bar{D}_{\bar{J}}\bar{W}=\frac{2\pi}{\ell_s^8}e^{\mathcal{K}^{\rm cs}+\mathcal{K}^{\rm ax}}\mathcal{K}^{I\bar{J}}D_I W\bar{D}_{\bar{J}}\bar{W} \tag{4.1.23}$$

where the Kähler moduli are excluded.

The kinetic terms for all the Calabi-Yau moduli come from the Einstein Hilbert term in the 10-dimensional action. They are noncanonical. We identify where they come from as well compute the total relative factor between the kinetic and potential terms which will involve one remaining expression given in terms of the volume of the compactification manifold. This is meant as a qualitative description. First we decompose the 10-dimensional curvature scalar into the trace of the noncompact component of the Ricci tensor, that of the compact component (which is zero because Calabi-Yaus are Ricci flat), and the remaining terms which will involve products of

the metric and its derivatives with indices in both the compact manifold and large dimensions, which we label R^{mix},

$$R^{10} = R^4 + R^6 + R^{\text{mix}}. \tag{4.1.24}$$

Since R^4 is a constant over the Calabi-Yau, integration of it over Y yields a factor of the volume of the Calabi-Yau. The factor then in front of the resulting 4-dimensional Einstein-Hilbert term is

$$\frac{2\pi}{\ell_s^8}\text{Vol}(Y) = \frac{2\pi}{\ell_s^2}\mathcal{V}_0 = \frac{M_{\text{pl}}^2}{2}4\pi\mathcal{V}_0 \tag{4.1.25}$$

where we've defined the dimensionless constant $\mathcal{V}_0$, the volume of the Calabi-Yau manifold in string units. Since the string length is the fundamental length scale at which one will see string modes, the volume of the Calabi-Yau must be large compared to ℓ_s^6 for the direct compactification procedure we are employing to be valid.

In order to have a canonical Einstein-Hilbert term in the effective action one must rescale the 4-dimensional metric so that the curvature rescales precisely with a factor of $\frac{1}{4\pi\mathcal{V}_0}$. The new curvature term also comes with kinetic terms for the volume modulus because the volume, and thus the factor by which the 4-dimensional spacetime metric is rescaled, may be expressed in terms of the volume modulus[2], ρ.

Incidentally, the term in eq. 4.1.1 which clearly yields kinetic terms for the axio-dilaton, namely,

$$\sim \int \frac{d\tau \wedge *d\bar{\tau}}{(\text{Im}(\tau))^2}, \tag{4.1.26}$$

arises in precisely the same manner; specifically from transforming from the string metric to the Einstein metric by rescaling the string metric by $e^{\phi/2}$. The resulting

[2]The imaginary part of ρ cubed is proportional to the volume squared.

kinetic terms for ρ and τ are noncanonical, specifically given by,

$$\frac{M_{\rm pl}^2}{2}\int d^4x\ \frac{3}{(\rho-\bar{\rho})^2}\partial_\mu\rho\partial^\mu\bar{\rho}+\mathcal{K}^{\rm ax}_{\tau\bar{\tau}}\partial_\mu\tau\partial^\mu\bar{\tau} \tag{4.1.27}$$

ρ is not itself one of the Calabi-Yau moduli denoted by our indices $a, b, ...$ Rather it is a specific function of *all* the Kähler moduli. We shall shortly see that their noncanonical kinetic terms (involving the contraction with their Kähler metric) reside in that for ρ in eq. 4.1.27.

The kinetic terms for the complex structure moduli come from integration of $R^{\rm mix}$ over Y, and so are also generally noncanonical involving contraction with their respective Kähler metric as follows,

$$\frac{M_{\rm pl}^2}{2}\int d^4x\mathcal{K}_{a\bar{b}}\partial_\mu\varphi^a\partial^\mu\bar{\varphi}^b \tag{4.1.28}$$

We can thus write the effective action describing the moduli,

$$S_{eff}=\frac{M_{\rm pl}^2}{2}\int d^4x\mathcal{K}_{I\bar{J}}\partial_\mu\varphi^I\partial^\mu\bar{\varphi}^J-\frac{M_{\rm pl}^2}{4\pi}\frac{e^{\mathcal{K}^{\rm cs}+\mathcal{K}^{\rm ax}}}{\mathcal{V}_0^2}\left(\mathcal{K}^{I\bar{J}}D_IW\bar{D}_{\bar{J}}\bar{W}\right). \tag{4.1.29}$$

Any consistent flux compactification of type II string theories on Calabi-Yau manifolds requires the addition of negative tension localized objects. This is necessary in order to satisfy $\tilde{F}_{(5)}$'s equation of motion which, when integrated over the Calabi-Yau, yields the following tadpole condition,

$$\frac{1}{\ell_s^4}\int_Y F_{(3)}\wedge H_{(3)}+Q_3^{loc}=0. \tag{4.1.30}$$

This is effectively a statement of the consistency of the configuration of field lines wrapping the Calabi-Yau 3-cycles (i.e. field lines in the small dimensions curl and close onto themselves, while those in large dimensions end on mathematically valid

sources).

It can be shown that the term in eq. 4.1.30 involving the RR and NSNS fluxes is positive definite. Of the allowed localized objects that preserve Poincaré invariance in the four large dimensions and can act as sources for the fluxes, only the O3-planes contribute a negative charge to the total Q_3^{loc}, thus they must be included in the compactifation in order to cancel all the remaining positive definite terms in eq. 4.1.30. Though the O3-planes are not dynamical, they do in general impact the moduli space geometry. We assume a model in which such effects are negligible. O3-planes also reduce the $\mathcal{N} = 2$ supersymmetry we began with to $\mathcal{N} = 1$.

Generic theories with $\mathcal{N} = 1$ supersymmetry involve complex scalars described by a potential of the form,

$$V = e^{\mathcal{K}} \left(\mathcal{K}^{a\bar{b}} D_a W \bar{D}_{\bar{b}} \bar{W} - 3|W|^2 \right), \tag{4.1.31}$$

where the superpotential, W, is a holomorphic function of the complex scalars $\{\varphi_a\}$. Notice that the $-3|W|^2$ term is absent in our effective action. This 'no-scale' form arises from a simple but general cancellation inherent to Calabi-Yau compactifications at the classical level. Namely, because the classical superpotential is independent of the Kähler moduli, the Kähler dependence of the scalar potential arises solely from the contribution to $\sim |DW|^2$ from

$$\mathcal{K}^{a\bar{b}}\, \mathcal{K}_a\, W\, \mathcal{K}_{\bar{b}}\, \bar{W} = \mathcal{K}_a\, \mathcal{K}^a\, |W|^2 \tag{4.1.32}$$

with indices running over the Kähler moduli only. The classical expression for their

Kähler potential (i.e. that which comes from the special geometry) is,

$$\mathcal{K}^{\text{kä}} = -2\log\left(\int_Y J\wedge J\wedge J\right) \tag{4.1.33}$$

$$= -2\log\left(\frac{1}{\ell_s^6}\int_Y dV\right) = -\log(\mathcal{V}_0^2) \tag{4.1.34}$$

$$= -3\log\left(-i\left(\rho-\bar{\rho}\right)\right). \tag{4.1.35}$$

So,

$$\mathcal{K}_a\,\mathcal{K}_{\bar{b}}\,\mathcal{K}^{a\bar{b}} = \partial_a\,\rho\,\partial_{\bar{b}}\,\bar{\rho}\,\mathcal{K}_\rho\mathcal{K}_{\bar{\rho}}\;\frac{1}{\partial_\rho\partial_{\bar{\rho}}\,\mathcal{K}}\;\partial_\rho\,\varphi^a\partial_{\bar{\rho}}\,\bar{\varphi}^b \tag{4.1.36}$$

$$= \mathcal{K}_\rho\,\mathcal{K}_{\bar{\rho}}\,\mathcal{K}^{\rho\bar{\rho}} \tag{4.1.37}$$

which gives,

$$\mathcal{K}_a\,\mathcal{K}^a = \frac{-3}{\rho-\bar{\rho}}\frac{+3}{\rho-\bar{\rho}}\frac{-(\rho-\bar{\rho})^2}{3} = +3. \tag{4.1.38}$$

This then yields the cancellation

$$\mathcal{K}^{a\bar{b}}\,\mathcal{K}_a W\,\mathcal{K}_{\bar{b}}\bar{W} - 3|W|^2 = 0. \tag{4.1.39}$$

The resulting scalar potential is positive semi-definite, and so its zeros are its global minima. Solutions of the SUSY condition, $D_I W = 0$ for all $I = 0, 1, ..., h^{2,1}$, are the only zeros because the metric and $e^{\mathcal{K}}$ are positive definite. In general, when $V \neq 0$ the scalar potential depends on the Kähler moduli through its overall dimensionful factor, $M_{\text{pl}}^2/4\pi\mathcal{V}_0^2$, but when $V = 0$, all such dependence drops out. The flattening of the potential at a zero in the volume direction of parameter space is shown schematically in figure 1.1.

We see too that the ρ-dependent factor in the kinetic term for the volume modulus in eq. 4.1.27 is indeed its Kähler metric, $\mathcal{K}_{\rho\bar{\rho}}$. We may identify this term as the net kinetic term for the Kähler moduli in eq. 4.1.29, similarly by the chain rule. Finally,

we recognize $1/\mathcal{V}_0^2$ in eq. 4.1.29 as $e^{\mathcal{K}^{\text{kä}}}$, and thus, the effective action we obtain upon compactification as that of a theory with $1 + h^{2,1} + h^{1,1}$ complex scalars and $\mathcal{N} = 1$ supersymmetry with an additional/non-generic feature. Namely, the cancellation of the $-3|W|^2$ in the potential by the contribution from a subset of the scalars, specifically $h^{1,1}$ of them. The feature is entirely due to the fact we've compactified on a Calabi-Yau manifold and used only classical expressions.

These are, generally speaking, subject to both α' and g_s corrections. In type IIb, the complex structure Kähler potential is protected from both types, but the Kähler moduli are not shielded from either. However, as is well known, such corrections are suppressed in the large volume limit,[3] as are the instanton corrections the superpotential receives. This setting also ensures backreaction of the fluxes on the geometry of the manifold is subdominant. We will work in this regime and so now use the formulae we've reviewed to set up explicit calculations on the mirror quintic.

Period Integrals

To search for local minima of the effective potential and compute its Taylor coefficients in the expansion about these minima one must express the quantities in eq. 4.1.29 as explicit functions of the complex structure(s) and axio-dilaton. To accomplish this we need only express W and $\mathcal{K}^{\text{cs}}$ in this fashion, as all terms in eq. 4.1.29 are obtained from them. Generally, the integrals over the compactification manifold need not be computed directly. Rather they can be expressed in terms of a basis of systematically calculable functions, the *period integrals* of the Calabi-Yau manifold, which are solutions to differential equations (specific to the compactification manifold) known as the Picard-Fuchs equations.

By the Poincaré dulaity $H^{(3)}(Y)$ is isomorphic to $H_{(3)}(Y)$, the space of nontrivial

[3]This limit is one in which not only the 6-volume but all subvolumes are large compared to the natural sizes (involving the dimensionful constants).

3-cycles. Thus, for any two closed 3-forms $\alpha_{(3)}$ and $\beta_{(3)}$ there exist two 3-cycles A and B such that,

$$\int_Y \alpha_{(3)} \wedge \beta_{(3)} = \int_A \beta_{(3)} = \int_B \alpha_{(3)}. \tag{4.1.40}$$

If $\{C_i\}$ are a basis of 3-cycles, the right hand sides of eq. 4.1.40 are a linear combination of the integrals of the relevant 3-form over the basis cycles.

$$\int_A \beta_{(3)} = \sum_{i=1}^{h^3} A^i \int_{C_i} \beta_{(3)} \tag{4.1.41}$$

$$\int_B \alpha_{(3)} = \sum_{i=1}^{h^3} B^i \int_{C_i} \alpha_{(3)} \tag{4.1.42}$$

where the A^i and B^i are real numbers (the components of A and B in the C_i basis). Thus, W can be expressed as a linear combination of the integrals of the holomorphic 3-form over the basis cycles for $H_{(3)}(Y)$. These are known as the *period integrals*, or *period functions*. They are functions of the complex structure moduli only.

We note the existence of an integral and symplectic basis. The first of these properties means C_i is a geometrical cycle (that is, a submanifold, not merely a formal object defined as the dual to a 3-form). The second means each basis cycle intersects only one other basis cycle, and does so exactly one time. We denote the period functions in this basis as follows,

$$\Pi_i(z^1, ...z^{h^{2,1}}) = \int_{C_i} \Omega \tag{4.1.43}$$

where the index i ranges from zero to $2h^{2,1}+1$ for a total of h^3 different periods. The symplectic basis is the one most natural for us because the period functions have well defined expansions about special points in the moduli space where vacua accumulate, as we shall discuss at greater length shortly.

The intersection form allows us to express the effective action in terms of these

natural period functions. Two 3-cycles intersect at points in a 6-dimensional manifold. Since cycles are oriented such points will have multiplicity ± 1. The intersection form, in the context where the (3)-homology groups are the domain, takes in two 3-cycles and sums the intersection multiplicities. In light of the Poincaré duality this is equally viewed as a map from two copies of the (3)-cohomology groups. That is, we write

$$Q_{ij} = Q(C_i, C_j) = \langle C_i \smile C_j[Y] \rangle \tag{4.1.44}$$

$$= \tilde{Q}_{ij} = \tilde{Q}(\alpha_i, \alpha_j) = \int_Y \alpha_i \wedge \alpha_j. \tag{4.1.45}$$

In an integral and symplectic basis Q_{ij} are the entries of a symplectic $h^3 \times h^3$-matrix.

The superpotential, W, can now be expressed as follows,

$$W = \sum_{i=0}^{4} G^i \Pi_i(z) \tag{4.1.46}$$

$$= (F - \tau H) \cdot \Pi(z) \tag{4.1.47}$$

where F and H are row vectors whose four entries indicate the quantity of RR and NSNS flux wrapping the basis cycles, and $\Pi(z)$ is a column vector containing the h^3 period functions. It can be shown that the 3-form fluxes wrapping the integral and symplectic basis cycles are integrally quantized in units of $4\pi^2\alpha'$,

$$\frac{1}{2\pi\alpha'} \int_{C_i} F_{(3)} \in 2\pi\mathbb{Z} \tag{4.1.48}$$

and similarly for $H_{(3)}$. Since the overall dimensionful factor has been pulled outside the potential, this amounts to requiring the entries of the F and H vectors in eq. 4.1.47 be integers.

The Kähler potential for the complex structure modulus is expressed in terms of

the period functions as follows,

$$\mathcal{K}^{\rm cs}(z,\bar{z}) = -\log(i\Pi^\dagger(\bar{z})Q^{-1}\Pi(z)) \tag{4.1.49}$$

In evaluating these functions, one can avoid performing an integration over the compactification manifold because the periods are solutions to particular differential equations, the Picard-Fuchs equations (associated with the given Calabi-Yau). Given the above expressions for the superpotential and Kähler potential, one need only find the solutions to these differential equations to write down an explicit effective action for the moduli.

The complexity of the Picard-Fuchs equations quickly mounts as the number of moduli increase. We consider the simplest case, where $h^{2,1} = 1$, and so there are a total of four period functions. There is a complete list 14 such compactifications, the most well known being the mirror quintic. For these 14 models the Picard-Fuchs equation takes the following form,

$$\left[\delta^4 - z(\delta+\alpha_1)(\delta+\alpha_2)(\delta+\alpha_3)(\delta+\alpha_4)\right] u(z) = 0 \tag{4.1.50}$$

where $\delta \equiv z\frac{d}{dz}$, and the α_j are rational numbers specific to the compactification (the mirror quintic has $\alpha_j = j/5$).

A convenient basis for expressing solutions to this ODE, which we shall label

$\{U_i(z)\}_{i=0}^3$, is as follows [50]

$$U_0(z) = c\, G^{1,3}_{4,0}(-z; \{1-\alpha_1, 1-\alpha_2, 1-\alpha_3, 1-\alpha_4\}, \{0,0,0,0\}) \tag{4.1.51}$$

$$U_1(z) = \frac{c}{2\pi i} G^{2,2}_{4,0}(z; \{1-\alpha_1, 1-\alpha_2, 1-\alpha_3, 1-\alpha_4\}, \{0,0,0,0\}) \tag{4.1.52}$$

$$U_2^-(z) = \frac{c}{(2\pi i)^2} G^{3,1}_{4,0}(-z; \{1-\alpha_1, 1-\alpha_2, 1-\alpha_3, 1-\alpha_4\}, \{0,0,0,0\})$$

$$U_3(z) = \frac{c}{(2\pi i)^3} G^{4,0}_{4,0}(z; \{1-\alpha_1, 1-\alpha_2, 1-\alpha_3, 1-\alpha_4\}, \{0,0,0,0\}) \tag{4.1.53}$$

$$U_2(z) = \begin{cases} U_2^-(z) & \mathrm{Im}(z) \leq 0 \\ U_2^-(z) - U_1(z) & \mathrm{Im}(z) > 0 \end{cases} \tag{4.1.54}$$

The $G^{m,n}_{p,q}$ are Meijer-G functions defined in terms of contour integrals in the complex, say, s-plane,

$$G^{m,n}_{p,q}(z; \{a_1, ...a_p\}, \{b_1, ..., b_q\}) = \frac{1}{2\pi i} \int_L ds \frac{\Pi_{j=1}^m \Gamma(b_j - s) \Pi_{j=1}^n \Gamma(1 - a_j + s)}{\Pi_{j=m+1}^q \Gamma(1 - b_j + s) \Pi_{j=n+1}^p \Gamma(a_j - s)} z^s \tag{4.1.55}$$

where c is a constant specific to the given Calabi-Yau (one of the 14 models),

$$c = \frac{1}{\Gamma(\alpha_1)\Gamma(\alpha_2)\Gamma(\alpha_3)\Gamma(\alpha_4)}. \tag{4.1.56}$$

The particular linear combinations of the $U_i(z)$ that yield the periods in the integral symplectic basis, the $\Pi_i(z)$'s, are fixed by the calculable monodromy transformations of the homology cycles when transported about certain special points in the moduli space. For the case of $h^{2,1} = 1$ there are three such special points: the large complex structure point (which corresponds to $z = 0$ in our coordinates), the conifold point ($z = 1$) and the Landau-Ginsburg point ($z = \infty$). These nontrivial monodromy transformations of the 3-cycles in turn yield nontrivial transformations for the corresponding period functions.

For instance, if we donate the shrinking sphere as the conifold is approached by

C_3, and the cycle it intersects by C_0, then

$$Q_{03} = \langle C_0 \smile C_3, [Y] \rangle \rightarrow \langle C_0 + nC_3 \smile C_3, [Y] \rangle \tag{4.1.57}$$

$$= \langle C_0 \smile C_3, [Y] \rangle + n \langle C_3 \smile C_3, [Y] \rangle \tag{4.1.58}$$

$$= Q_{03} + n * 0 = Q_{03}. \tag{4.1.59}$$

The integer n is specified by requiring mutual consistency between all the monodromy transformations in the mirror quintic's moduli space, and as is well-known, this requires $n = 1$. The monodromy transformations imply that the linear combinations of the aforementioned solutions to the Picard-Fuchs equation, $\{U_i\}$, that correspond to the period integrals in a symplectic basis for the mirror quintic are given by,

$$\Pi_0(z) = U_0(z) \tag{4.1.60}$$

$$\Pi_1(z) = -U_1(z) \tag{4.1.61}$$

$$\Pi_2(z) = 3U_1(z) - 5U_2(z) \tag{4.1.62}$$

$$\Pi_3(z) = 5U_1(z) + 5U_3(z) \tag{4.1.63}$$

where Π_3 is the (analytic) period that vanishes at the conifold point, it's partner, Π_0, picks up a copy of Π_3 for each revolution about the conifold point, and the remaining periods are analytic and nonvanishing. For a detailed derivation including the general form for any of the 14 one parameter models see, for instance, Appendix A of [50].

The transformations of the periods upon circling a given special point in the moduli space fix their expansions in the neighborhood of the special point. In the case of the conifold point the transformation,

$$\Pi_0(z) \rightarrow \Pi_0(z) + \Pi_3(z) \tag{4.1.64}$$

for each revolution $z \to (z-1)e^{2\pi i}+1$, implies

$$\Pi_0(z) = \Pi_3(z)\frac{\log(z-1)}{2\pi i} + f(z) \tag{4.1.65}$$

where $f(z)$ is analytic and nonvanishing at the conifold point. The expansions of the period functions are discussed in detail in the following section. For now we remark that the branch cut for Π_0 introduces a branch point singularity in first derivative of Π_0 which in turn results in a singularity in the Kähler metric at the conifold point.

We also adopt the standard convention (see, e.g., [50] for details) where the entries of the period vector, $\Pi(z)$, are given in descending order,

$$\Pi(z) = \begin{pmatrix} \Pi_3(z) \\ \Pi_2(z) \\ \Pi_1(z) \\ \Pi_0(z) \end{pmatrix} \tag{4.1.66}$$

while those in the flux vectors are labeled in ascending order,

$$F = \begin{pmatrix} F_0, & F_1, & F_2, & F_3 \end{pmatrix} \tag{4.1.67}$$

$$H = \begin{pmatrix} H_0, & H_1, & H_2, & H_3 \end{pmatrix}. \tag{4.1.68}$$

With this review of notation and conventions, all functions in the effective action have now been specified. The only free parameters are the fluxes, which for us consist of eight integers (four RR and four NSNS fluxes). So, by randomly selecting a set of eight integers, constructing the corresponding scalar potential, searching for local minima (in the $z-\tau$ field space), and evaluating the potential's Taylor coefficients about the local minima so identified, one obtains the masses and couplings of a sample of effective field theories in the landscape of the mirror quintic. Since this model's only

dynamical fields are the axio-dilaton and the mirror quintic's sole complex structure modulus there are a total of four real degrees of freedom.

For the masses and couplings to have physical significance one must trade the $\{z, \tau, \bar{z}, \bar{\tau}\}$ basis for one that simultaneously diagonalizes the Hessian of the scalar potential, and yields kinetic terms that are canonical (i.e. the Kähler metric evaluated at the vacuum is the identity). This transformation and several other technicalities are discussed in detail in section 4.2, but here we finish outlining the strategy in broad strokes.

To minimize a function numerically we must begin by providing a guess for the vacuum location. Vacua are known to accumulate near the aforementioned special points in the moduli space, especially near the conifold point. We focus our search there. Moreover, we look specifically for zeros of the scalar potential, which are solutions to the SUSY condition $D_z W = D_\tau W = 0$. This restriction both dramatically reduces the computational expense of searching for vacua by decreasing the (real) dimension of the space over which the function needs to be minimized from four to two, as well as enables us to compute a guess location given a choice of fluxes (which is essential for numerical minimization). These are not SUSY vacua in the traditional sense because we do not require that the superpotential itself vanish at the vacua.

The first of these simplifications is due the fact that the two SUSY conditions imply that the vacuum value of the axio-dilaton τ_{SUSY} for a given choice of fluxes is an explicit function of the complex structure vacuum location. In particular,

$$\tau_{SUSY} = \frac{F \cdot \bar{\Pi}(\bar{z}_{SUSY})}{H \cdot \bar{\Pi}(\bar{z}_{SUSY})} \tag{4.1.69}$$

So, we evaluate the axio-dilaton in the function we seek to minimize, $|D_z W|^2$, at $\tau = \tau_{SUSY}(z)$. We then need only minimize over the variation of two real fields (the real and imaginary parts of z). The guess location, z_{guess}, for the given set of fluxes

can be computed straightforwardly by using the near conifold period expansions in the period vectors and the Kähler potential below,

$$D_z W(z, \tau_{SUSY}(z)) = \left(F - \frac{F \cdot \bar{\Pi}(\bar{z})}{H \cdot \bar{\Pi}(\bar{z})} H \right) \cdot (\Pi'(z) + \mathcal{K}_z \Pi(z)) = 0, \tag{4.1.70}$$

We compute the leading order solution to the above, which amounts to retaining the $\log(z-1)$ and constant terms, and dropping everything $\mathcal{O}(z-1)$. The resulting z_{guess} is given in terms of the flux integers and period expansion coefficients in section 4.2.

To proceed further, it is essential to have high accuracy approximations to the period functions near the conifold point. The Meijer-G functions, with respect to which the periods and their derivatives can be expressed, are generally slow to evaluate numerically. As the singularities of the Meijer-G's are approached (for example the branch point singularity for $\Pi_0'(z)$, and terms $\sim \frac{1}{(z-1)^{k-1}}$ for its k^{th} order derivative) this becomes a significant obstacle. We not only evaluate such expressions multiple times while searching for a single vacuum, but we then must compute the Taylor coefficients at the near conifold vacuum found. This will involve many additional evaluations of increasingly divergent (due to the derivatives taken) Meijer-G's near their singularities. The tremendous number of times the search algorithm needs to be run to find a sufficiently large random sample of vacua, and the subsequent computation of the Taylor coefficients makes it essential to have high accuracy fast approximations to the period functions near the conifold point.

Additionally, we note that such approximations are also needed near the large complex structure point ($z = 0$). The minima we are searching for typically have basins of attraction that narrow sharply near the minimum. Though a particular set of fluxes may yield a guess in the neighborhood of the conifold point, and so be worthy of pursuing, the guess may lie far up the minimum's basin outside the basin's thin throat. Iterative minimization procedures work by taking a steps in the direction

of the gradient of the function being minimized. A narrow basin that then flattens out can result in significant overshooting of the minimum during the first steps. The search region needs to be large enough to contain these initial sweeps as it ping-pongs around the minimum, and eventually spiral into it.

The surrounding buffer area we need includes the large complex structure point. The behavior of the periods here is well known, $\Pi_i \to (z\log(z))^i$. Due to the branch cuts in the periods, many of the Meijer-G's in the expressions we seek to minimize are singular. So, when searching for vacua we use "patched period functions" — piecewise defined fast approximations to the exact expressions in terms of the Meijer-G's. Outside the neighborhoods of both the large complex structure point and conifold point (where the expansions are used), we build interpolating functions by evaluating the exact periods on a grid. The entire search region showing the neighborhoods where each of the three type of approximations to the period functions are used is found in figure 4.1. We postpone further discussion of the search algorithm until the Calculational Approach section, and now turn to the computation of the fast approximations to the period functions.

Period Expansions for the Mirror Quintic

Three of the mirror quintic's four period integrals (in the integral and symplectic basis) are analytic in the neighborhood of the conifold point. These are the intersecting pair $\Pi_1(z)$ and $\Pi_2(z)$ which are nontrivial at the conifold point, and $\Pi_3(z)$ which vanishes because it is an integral over the collapsing three cycle. These can be

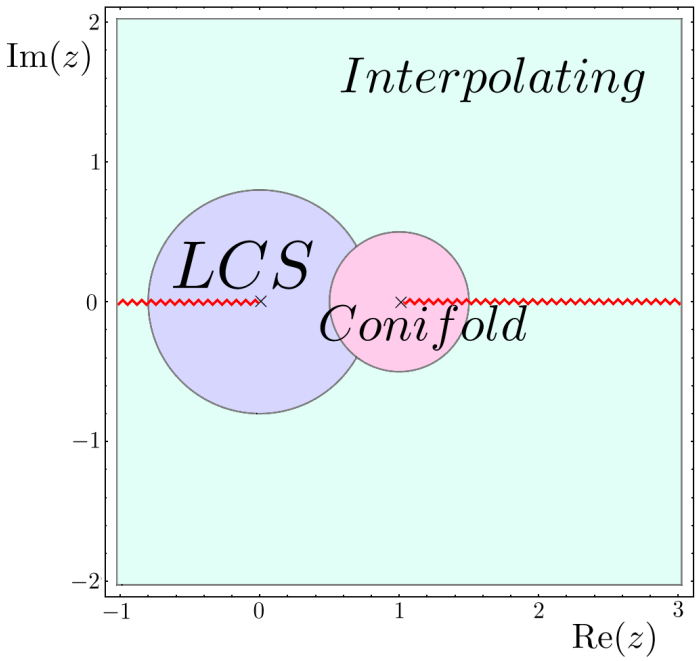

Figure 4.1: We search for no scale vacua in the square portion of the complex plane for z depicted above. The three regions where we use different fast approximations to the period functions are shown using different colors. The near-conifold patch consists of the disk of radius 0.5 centered at the conifold, $z = 1$. The portion of the disk of radius 0.8 centered at the LCS point, $z = 0$, that is not contained within the near-conifold region is shown in purple. Here we use the 12th order expansions about $z = 0$ obtained directly from Mathematica. Lastly, an interpolating function built from discrete Meijer-G data is used in the remaining portion of the square search region, shown in light green. Branch cuts are indicated by the red zigzag lines, with the one emanating from the conifold point along the positive real axis applying to Π_0, and those emanating along the negative real axis from the LCS point of relevance to all periods excluding Π_0.

approximated straightforwardly by truncating their Taylor series. We write,

$$\Pi_1(z) = \sum_{n=0}^{q} b_n (z-1)^n \tag{4.1.71}$$

$$\Pi_2(z) = \sum_{n=0}^{q} c_n (z-1)^n \tag{4.1.72}$$

$$\Pi_3(z) = \sum_{n=1}^{q} d_n (z-1)^n. \tag{4.1.73}$$

The periods and their first derivatives enter the scalar potential. Since we seek

to collect up to fourth order Taylor coefficients of the scalar potential at the vacua located, we will be evaluating fifth order derivatives of the periods near $z = 1$. For the sake of accuracy we take $q = 8$. The expansion coefficients can be found in table 1 of Appendix 4.4.

The remaining period, Π_0, picks up one factor of its intersecting partner, Π_3, for each loop about the conifold point. This transformation property of Π_0 restricts its form to

$$\Pi_0(z) = \Pi_3(z)\frac{\log(z-1)}{2\pi i} + f(z) \tag{4.1.74}$$

for some function $f(z)$ that is analytic at the conifold point. Before proceeding we note that we shall henceforth include an overall minus sign in front of the argument in the logarithm in the expansion of Π_0 so that all explicit values of the expansion coefficients correspond to a consistent choice of branch cuts in Mathematica. Specifically, the expressions given for the periods in terms of the Meijer-G's use the convention of branch cuts emanating from the conifold point along the positive real axis, and from the large complex structure point along the negative real axis. Since Mathematica's logarithm function places the branch cut along the argument's negative real axis, it is necessary to include a minus sign in front of the log's argument in the expansion, eq. 4.1.74, to flip it from $(-\infty, 1]$ to $[1, +\infty)$.

Note that the argument of the logarithm in Π_0's expansion may be rescaled freely because this amounts to a relabeling of analytic terms. The righthand side of eq. 4.1.74 is equivalently written as

$$\Pi_3(z)\frac{\log(-(z-1))}{2\pi i} + f(z) - \frac{\Pi_3(z)}{2} = \Pi_3(z)\frac{\log(-(z-1))}{2\pi i} + \tilde{f}(z). \tag{4.1.75}$$

The shifted function, $\tilde{f}(z)$, is still analytic because Π_3 is. Relabeling $\tilde{f}(z)$ by $f(z)$ we have the same expression as eq. 4.1.74, only with a negative sign in front of the $(z-1)$. We choose however to keep the "extra" analytic term, $-\Pi_3/2$, separate and

take the form,

$$\Pi_0(z) = \Pi_3(z)\left(\frac{\log(-(z-1))}{2\pi i} - \frac{1}{2}\right) + f(z). \tag{4.1.76}$$

It is a convenient choice for performing checks of the accuracy of the Π_0 approximation because the factor multiplying Π_3 does not change sign (the range of the imaginary part of the logarithm function in Mathematica is $[-\pi, \pi]$).

Since we have a polynomial expansion for Π_3, the task of obtaining a fast approximation for Π_0 amounts to finding one for the unknown $f(z)$. Since we have no special restrictions to this function's properties aside from analyticity, the simplest approximation is a Taylor series about $z = 1$. We write

$$f(z) = \sum_{n=0}^{q} a_n (z-1)^n. \tag{4.1.77}$$

The zeroth coefficient is the value of Π_0 at the conifold point, which is trivial to compute. The higher order coefficients are more difficult.

Although each

$$a_n = \frac{1}{n!}\frac{d^n f}{dz^n}\bigg|_{z=1} = \frac{1}{n!}\left(\frac{d^n \Pi_0}{dz^n}\bigg|_{z=1} - \frac{1}{2\pi i}\frac{d^n}{dz^n}\left[\Pi_3(z)\left(\log(-(z-1)) - \frac{1}{2}\right)\right]\bigg|_{z=1}\right) \tag{4.1.78}$$

is finite, the fact that the divergences between the two terms on the righthand side cancel exactly at each order is lost if one attempts to evaluate (numerically) the righthand side exactly the conifold point. Mathematica's "Limit" function cannot be used to remedy this. However, the next coefficient, a_1, is nonetheless easily obtained numerically by exploiting the weakness of the divergences that cancel in the first derivative, which are logarithmic.

In particular, to leading order in $s \equiv (z-1)$, a_1 is given by,

$$a_1 = \left(\frac{d\Pi_0}{dz}\bigg|_{z=1} - d_1\frac{\log(-s)}{2\pi i}\right) + \frac{i d_1}{2\pi} + \frac{d_1}{2} + \mathcal{O}(s\log(s)). \tag{4.1.79}$$

We obtain an approximate value for a_1 by dropping the $\mathcal{O}(s)$ terms which involve higher order (unknown as of now) a_i's and evaluating the remaining known expressions on the righthand side sufficiently close to the conifold point that errors due to the truncation are negligible. Taking the form $s = e^{-t}$, the negligibility of such errors at a finite $t = t^*$ is ensured if the value of $\tilde{a}_1(t)$ defined by,

$$\tilde{a}_1(t) = \Pi_0'(1 + e^{-t}) + \frac{id_1}{2\pi} + \frac{d_1}{2} - d_1 \frac{\log(-e^{-t})}{2\pi i} \tag{4.1.80}$$

converges within the relevant precision one is using for $t \to t^*$. Such convergence is exhibited in table 4.1.

t	$\tilde{a}_1(t)$
2	$0.0082657465 - 0.1488734062i$
3	$0.0143193561 - 0.1662234075i$
4	$0.0193211265 - 0.1734738528i$
5	$0.0221685901 - 0.1762752502i$
6	$0.0235728366 - 0.1773249249i$
7	$0.0242171435 - 0.1777137131i$
8	$0.0245004660 - 0.1778570993i$
9	$0.0246216047 - 0.1779098968i$
10	$0.0246723700 - 0.1779293266i$
12	$0.0247018694 - 0.1779391052i$
14	$0.0247067045 - 0.1779404287i$
16	$0.0247074729 - 0.1779406078i$
20	$0.0247076106 - 0.1779406353i$

Table 4.1: Depiction of the the convergence of the expansion coefficient a_1 computed numerically.

The third coefficient in f's expansion, a_2, can be obtained in a similar fashion. We write

$$\tilde{a}_2(t) \equiv \frac{1}{2}\left[\Pi_0''(1 + e^{-t}) + d_2 + \frac{3id_2}{2\pi} + \frac{id_1 e^t}{2\pi} - \frac{d_2 \log(-e^{-t})}{\pi}\right] \tag{4.1.81}$$

However, here it is essential to use high-digit accuracy computations when evaluating the righthand side for a given value of t. This is because we're extracting a small

number by taking the difference of two large numbers, $\Pi_0''(1+e^{-t})$ and the term proportional to e^t in eq. 4.1.81. table 4.2 displays the convergence of a_2.

t	$\tilde{a}_2(t)$
2	$0.00213219053 + 0.09247047120i$
3	$-0.00142768524 + 0.11114853496i$
4	$-0.00594277215 + 0.11937168288i$
5	$-0.00880198201 + 0.12261391639i$
6	$-0.01027763172 + 0.12383805148i$
7	$-0.01097135473 + 0.12429273911i$
8	$-0.01128102108 + 0.12446060393i$
10	$-0.01147126928 + 0.12454519737i$
12	$-0.01150432390 + 0.12455665210i$
16	$-0.01151065730 + 0.12455841226i$
20	$-0.01151081435 + 0.12455844450i$
24	$-0.01151081798 + 0.12455844509i$
28	$-0.01151081806 + 0.12455844510i$

Table 4.2: Depiction of the convergence of the expansion coefficient a_2 computed numerically.

Clearly this strategy is limited to the lowest expansion coefficients. At each higher order the righthand side will involve evaluating increasingly divergent terms near the conifold point and extracting an ever (comparatively) smaller difference. To obtain the higher order coefficients we instead derive a recursion relation for the a_n's by using the fact that both Π_0 and Π_3 are solutions to the Picard-Fuchs equation. Specifically, since the Picard-Fuchs equation is linear, $f(z)$ must satisfy

$$\hat{O}_{PF}[f(z)] = -\hat{O}_{PF}\left[\Pi_3(z)\left(\frac{\log(-(z-1))}{2\pi i} - \frac{1}{2}\right)\right]. \tag{4.1.82}$$

The righthand side is a known, albeit messy, analytic function due to the fact that Π_3's near conifold expansion coefficients are known. Note that because $\mathcal{O}_{PF}$ is a fourth order differential operator the righthand side will contain terms that are individually divergent (from derivatives acting on the log times the lower order terms in Π_3 so as to yield contributions $\sim s^{-1}$ and s^{-2}). The divergences, though, exactly

cancel due to the strict relationship among Π_3's coefficients, owing to the fact that it satisfies

$$\hat{O}_{PF}[\Pi_3(z)] = 0. \tag{4.1.83}$$

Thus, we need only express the lefthand side of eq. 4.1.82 as a power series in s (whose coefficient at a given order is a linear combination of a subset of the $\{a_i\}$) and ensure we have enough of the lowest order coefficients to generate the rest. It will turn out that the zeroth order term on the lefthand side involves f's four lowest order coefficients, and all those of order $n > 0$ involve the $n-1^{\text{th}}$ and subsequent four coefficients: $\{a_{n-1}, .., a_{n+3}\}$. Hence, the a_0, a_1 and a_2 obtained numerically as described above will be sufficient to start off the recursive procedure, and provide us as many coefficients as we need.

To that end, we rewrite the Picard-Fuchs differential operator as follows,

$$\begin{aligned}\hat{O}_{PF} &= -s\delta^4 - s(k_1\delta^3 - k_2\delta^2 - k_3\delta - k_4) - (k_1\delta^3 - k_2\delta^2 - k_3\delta - k_4) \\ &= -s\sum_{i=0}^{4} k_i\delta^{4-i} - \sum_{i=1}^{4} k_i\delta^{4-i}\end{aligned} \tag{4.1.84}$$

where the k_i are the constants,

$$k_0 = 1 \tag{4.1.85}$$

$$k_1 = \sum_{i=1}^{4} \alpha_i \tag{4.1.86}$$

$$k_2 = \sum_{i=1}^{4}\sum_{j=i+1}^{4} \alpha_i\alpha_j \tag{4.1.87}$$

$$k_3 = \alpha_1\alpha_2\alpha_3 + \alpha_1\alpha_2\alpha_4 + \alpha_2\alpha_3\alpha_4 \tag{4.1.88}$$

$$k_4 = \alpha_1\alpha_2\alpha_3\alpha_4. \tag{4.1.89}$$

Next note that δ acts on s^n as,

$$\begin{aligned}\delta s^n &= (s+1)\frac{d}{dz}(z-1)^n \\ &= (s+1)ns^{n-1} \\ &= n(s^n + s^{n-1}).\end{aligned}$$

By repeatedly applying this rule each of the $\delta^j s^n$ terms can be computed. For instance,

$$\begin{aligned}\delta^2 s^n &= \delta[n(s^n + s^{n-1})] \\ &= n(n(s^n + s^{n-1}) + (n-1)(s^{n-1} + s^{n-2})) \\ &= n^2 s^n + n(2n-1)s^{n-1} + n(n-1)s^{n-2}.\end{aligned}$$

After similarly obtaining δ^3 and δ^4 on s^n, collecting terms and shifting indices of summation, the Picard-Fuchs operator's action on $f(z)$ can be expressed in the form,

$$\hat{O}_{PF}\left[f(z)\right] = \sum_{n=0}^{\infty}\Big(C_{-1}(n)a_{n-1} + C_0(n)a_n + C_1(n)a_{n+1} + C_2(n)a_{n+2} + C_3(n)a_{n+3}\Big)s^n, \tag{4.1.90}$$

where $a_{-1} \equiv 0$ and the constants $C_j(n)$ are also functions of the k_i. Though a tedious exercise, the $C_j(n)$ can be obtained straightforwardly with the aid of Mathematica. A similar procedure yields the expansion of the righthand side of eq. 4.1.82 thus completing the recursion relation. The resulting values for the a_n are given in table 2 located in Appendix 4.4.

The analogous expansions about the large complex structure point are far easier to obtain numerically, despite the fact that three as opposed to one of the cycles transform nontrivially upon circling it. Being finite but multiple-valued, the form

of the corresponding three periods involve linear combinations of powers of $z \log z$. As mentioned at the end of subsection 4.1, the leading order behavior of the jth period in our notation (that is the term that contributes the most divergent term to the period's derivative) is $(z \log z)^j$. This form includes the behavior of the analytic period, Π_0, which is $\approxeq 1$.

Since each of the other three periods has its own residual analytic term (analogous to $f(z)$ in eq. 4.1.74) as well as an additional subleading logarithmic term at each period index j higher, the near large complex structure expressions are more complicated. Nonetheless, the approximations can be obtained using Mathematica's "Series" function, due to the special properties of Meijer-Gs. Essentially, one can expand the $G^{m,n}_{p,q}$ in eq. 4.1.55 about $z = 0$ to yield a series of integrals whose individual terms are easy to evaluate.

Structure of the Hessian

The masses of the moduli in the effective field theory associated with a given vacuum are contained in the Hessian of the scalar potential specified by the particular flux configuration. When evaluated at the vacuum location in the moduli space, the eigenvalues of the Hessian in canonically normalized field coordinates are the squares of the masses in the effective theory. No scale vacua have additional structure built in from the outset as compared to ordinary general $\mathcal{N} = 1$ supersymmetric theories.

We begin by expressing the general $\mathcal{N} = 1$ scalar potential — that which includes the Kähler moduli and does not assume cancellation of the $3|W|^2$ term — and its partial derivatives in terms of the appropriately invariant quantities. It is convenient to adopt the standard notation for the Kähler and geometrically covariant derivatives of the superpotential, up to third order,

$$F_I \equiv D_I W; \;\; Z_{IJ} \equiv D_I D_J W; \;\; U_{IJK} \equiv D_I D_J D_K W \tag{4.1.91}$$

Note that F_I is not to be confused with the amount of RR flux wrapping a particular 3-cycle of the compact manifold. We express general $\mathcal{N}=1$ scalar potential then as,

$$V = e^{\mathcal{K}}(F_I \bar{F}^I - 3|W|^2). \tag{4.1.92}$$

where indices run over all moduli.

Due to the Kähler invariance of eq. 4.1.92 we may trade partial derivatives for covariant ones and obtain the following covariant expressions [36].

$$\begin{aligned}
\partial_I V &= e^{\mathcal{K}}\left((D_I D_J W)\bar{F}^J - 2F_I \bar{W}\right) = e^{\mathcal{K}}\left(Z_{IJ}\bar{F}^J - 2F_I\bar{W}\right) \\
\partial_I \partial_J V &= e^{\mathcal{K}}\left((D_I D_J D_K W)\bar{F}^K - D_I D_J \bar{W}\right) = e^{\mathcal{K}}\left(U_{IJK}\bar{F}^K - Z_{IJ}\bar{W}\right) \\
\partial_I \partial_{\bar{J}} V &= e^{\mathcal{K}}\left(-R_{I\bar{J}K\bar{L}}\bar{F}^K F^{\bar{L}} + K_{I\bar{J}}F_K\bar{F}^K - F_I\bar{F}_{\bar{J}} + (D_I D_K W)(\bar{D}_{\bar{J}}\bar{D}^K\bar{W}) - 2K_{I\bar{J}}|W|^2\right) \\
&= e^{\mathcal{K}}\left(-R_{I\bar{J}K\bar{L}}\bar{F}^K F^{\bar{L}} + K_{I\bar{J}}F_K\bar{F}^K - F_I\bar{F}_{\bar{J}} + Z\bar{Z}_{I\bar{J}} - 2K_{I\bar{J}}|W|^2\right).
\end{aligned}$$

When the no scale cancellation takes place, and the SUSY condition for the remaining dynamical moduli in the theory is imposed the nontrivial components of the Hessian reduce to,

$$\partial_I \partial_J V = 2e^{\mathcal{K}}\bar{W}Z_{IJ} \tag{4.1.93}$$

$$\partial_I \partial_{\bar{J}} V = e^{\mathcal{K}}\left(Z\bar{Z}_{I\bar{J}} + \mathcal{K}_{I\bar{J}}|W|^2\right). \tag{4.1.94}$$

where $Z\bar{Z}$ is defined with the contraction of one holomorphic and one anti-holomorphic index using the (inverse) Kähler metric, and indices now run over only the axio-dilaton and complex structure moduli.

Next choose a basis for the complex moduli fields that is orthonormal with respect to the vacuum Kähler metric,

$$\mathcal{K}_{I\bar{J}}|_{vac} = \delta_{I\bar{J}}. \tag{4.1.95}$$

Such a basis is only unique up to unitary transformations. An arbitrary choice will not in general simultaneously diagonalize $Z^{can}\bar{Z}^{can}$. Note that while Z and $\bar{Z}$ are complex and symmetric, $Z\bar{Z}$ is Hermitian and positive definite, and is thus related to the diagonal matrix containing $N = 1 + h^{2,1}$ eigenvalues by a unitary transformation. In canonical coordinates we write,

$$Z^{can}\bar{Z}^{can} = U\Sigma^2 U^\dagger \tag{4.1.96}$$

and express the eigenvalues as the squares of real positive numbers λ_i. The columns of the unitary matrix, U, are of course the corresponding eigenvectors of the canonical $Z\bar{Z}$. (An excellent resource for understanding no scale structure and its implications is [51]. We've adopted their notation in our abridged calculation here in order to facilitate its use to readers seeking greater detail). Thus, the Hessian in canonical coordinates,

$$\mathcal{H}^{\text{can}} = e^{\mathcal{K}}\mathcal{U}^\dagger \begin{pmatrix} (Z\bar{Z})^{can}_{I\bar{J}} + \mathbb{1}_{2\times 2}|W|^2 & 2\bar{Z}^{can}_{\bar{I}\bar{J}}W \\ 2Z^{can}_{IJ}\bar{W} & (Z\bar{Z})^{can}_{\bar{I}J} + \mathbb{1}_{2\times 2}|W|^2 \end{pmatrix} \mathcal{U} \tag{4.1.97}$$

can be diagonalized by a unitary transformation defined in terms of the 2N×2N-matrix $\mathcal{U}$,

$$\mathcal{U} = \begin{pmatrix} U & 0 \\ 0 & U^\dagger \end{pmatrix}. \tag{4.1.98}$$

In particular, one can rewrite eq. 4.1.97 as,

$$\mathcal{H}^{\text{can}} = e^{\mathcal{K}}\mathcal{U}^\dagger \begin{pmatrix} \Sigma^2 + \mathbb{1}_{2\times 2}|W|^2 & 2\Sigma W \\ 2\Sigma\bar{W} & \Sigma^2 + \mathbb{1}_{2\times 2}|W|^2 \end{pmatrix} \mathcal{U} \tag{4.1.99}$$

A permutation of the rows and columns of matrix between $\mathcal{U}$ and $\mathcal{U}^\dagger$ in eq. 4.1.99

casts it as block diagonal, with each of the N 2×2 blocks having the form,

$$\begin{pmatrix} \lambda_i^2 + |W|^2 & 2\lambda_i W \\ 2\lambda_i \bar{W} & \lambda_i^2 + |W|^2 \end{pmatrix}. \tag{4.1.100}$$

The eigenvalues of the Hessian then come in pairs, namely those of each block times the overall factor of $e^{\mathcal{K}}$,

$$m_{i\pm}^2 = e^{\mathcal{K}} \left(\lambda_i \pm |W|\right)^2. \tag{4.1.101}$$

The fact that the scalar masses in no scale supergravity take the form of eq. 4.1.101 does not ensure a discernible pattern among the masses of an ensemble of vacua will emerge. Which pattern is present, if any, depends on the relative scales of the λ_i as well as how they compare to the magnitude of the superpotential at vacua. We shall see that a pronounced hierarchy and splitting of the field space *consistent across the ensemble* arises due to the special features of the conifold point, where our vacua accumulate. This is discussed at length in section 4.3. It is worth remarking that no association of one particular kind of moduli field (or a particular linear combination) with a heavy or light mass pair, nor the existence of separated mass pairs, is imposed by eq. 4.1.101.

4.2 Calculational Approach

There are two components to our procedure for generating a random sample of effective field theories in the mirror quintic's moduli space. In this section we discuss each of these in turn.

Generating a Random Sample of Vacua

Recall that we make the assumptions that the effect of O3-planes on the compact geometry is negligible at the level of the 4-dimensional action for the moduli, that all Kähler moduli are stabilized, and that the backreaction from fluxes (warping) can be ignored thus preserving the no scale structure given by compactifying type IIb supergravity on a Calabi-Yau.

The effective action for the two remaining complex scalars takes the form,

$$S_{eff} = \frac{M_{\rm pl}^2}{2}\int d^4x\, \mathcal{K}^{\rm cs}_{z\bar{z}}\partial_\mu z\partial^\mu\bar{z} + \mathcal{K}^{\rm ax}_{\tau\bar{\tau}}\partial_\mu\tau\partial^\mu\bar{\tau} - V(z,\tau,\bar{z},\bar{\tau}), \tag{4.2.1}$$

where both components of the field space metric are obtained by taking one holomorphic and one antiholomorphic derivative of the relevant Kähler potential. The Kähler potential for the complex structure is given by eq. 4.1.49, which is known explicitly in terms of Meijer-G functions via eqs. 4.1.60 —4.1.63 and 4.1.51–4.1.54. That for the axio-dilaton is obtained from eq. 4.1.19.

The scalar potential, V, is not a holomorphic function of z and τ. It is however defined in terms of the holomorphic superpotential, $W(z,\tau)$,

$$V = \frac{M_{\rm pl}^2}{4\pi\mathcal{V}_0^2}e^{\mathcal{K}^{\rm cs}(z,\bar{z})+\mathcal{K}^{\rm ax}(\tau,\bar{\tau})}\left(\mathcal{K}^{z\bar{z}}D_zW\bar{D}_{\bar{z}}\bar{W} + \mathcal{K}^{\tau\bar{\tau}}D_\tau W\bar{D}_{\bar{\tau}}\bar{W}\right). \tag{4.2.2}$$

The superpotential is parameterized by eight integers indicating the amount of RR and NSNS fluxes wrapping/piercing each of the mirror quintic's four 3-cycles. In particular, we write the superpotential as in eq. 4.1.47; a linear combination of the mirror quintic's period integrals in a symplectic basis (the Π_i's).

Solutions to the SUSY condition, $D_zW = D_\tau W = 0$, are zeros of the scalar potential and thus are global minima of the theory. We search specifically for such solutions by randomly scanning through models defined by eq. 4.2.1, that is by

randomly drawing eight flux integers. For simplicity, we assume a flat measure for the fluxes, and draw from the interval, $[-20, 20]$. Once the set of fluxes is drawn, the corresponding superpotential can be built, and the zeros of $D_I W$ can be searched for numerically.

The SUSY condition for the axio-dilaton implies it is an explicit function of the complex structure vacuum location, specifically that in eq. 4.1.69. By evaluating the SUSY condition for the complex structure, $D_z W = 0$, at $\tau = \tau_{SUSY}(z)$ we accomplish an important reduction in the computational expense of finding vacua numerically — we need only minimize a single (semipositive definite) function of two real variables, namely,

$$u(x, y; \{F_i, H_i\}) = \left| (F - \tau_{SUSY}(x + iy)H) \cdot (\Pi'(x + iy) + \mathcal{K}_z \Pi(x + iy)) \right|^2 . \quad (4.2.3)$$

where $\mathcal{K}_z$ is of course also a function of the real and imaginary parts of the complex structure, x and y. Specifically,

$$\mathcal{K}_z = -\frac{\Pi^\dagger(x - iy) Q^{-1} \Pi'(x + iy)}{\Pi^\dagger(x - iy) Q^{-1} \Pi(x + iy)}. \quad (4.2.4)$$

For a given set of fluxes the function, u, defined in eq. 4.2.3 can be assembled and minimized directly in Mathematica using its FindMinimum function, provided that an initial starting point (for x and y) is specified. Vacua are known to accumulate near the conifold point, $z = 1$, so it is reasonable to target our search here. Since we have simple expansions for the period functions here, namely eqs. 4.1.71–4.1.74, we may expand the Kähler covariant derivative of the superpotential with respect to the complex structure in $z - 1$. The term involving Π'_0 in $D_z W$ will yield a logarithm of $z - 1$. This is the most divergent term. By retaining only the logarithmic and $\mathcal{O}(1)$ terms in $D_z W = 0$ we can solve for z in terms of the fluxes. The result is,

$$z_{guess} = 1 - e^{\varphi} \tag{4.2.5}$$

$$\varphi = -1 + 2\pi i \left(\frac{\beta a_0 - a_1 - \frac{d_1}{2}}{d1} + \frac{F_2 - tH_2}{F_3 - tH_3}\frac{\beta b_0 - b_1}{d_1} + \frac{F_1 - tH_1}{F_3 - tH_3}\frac{\beta c_0 - c_1}{d_1} - \frac{F_0 - tH_0}{F_3 - tH_3} \right) \tag{4.2.6}$$

$$\beta = -\frac{\bar{a_0}d_1 - \bar{c_0}b_1 + b_0\bar{c_1}}{\bar{b_0}c_0 - \bar{c_0}b_0} \tag{4.2.7}$$

$$t = \frac{F_3\bar{a_0} + F_2\bar{b_0} + F_1\bar{c_0}}{H_3\bar{a_0} + H_2\bar{b_0} + H_1\bar{c_0}} \tag{4.2.8}$$

Note that the axio-dilaton has been evaluated at $\tau_{SUSY}(z; F, H)$ and expanded as well. It is the the $\mathcal{O}(1)$ constant, t, above.

There is no guarantee that a random choice of fluxes will have a near conifold minimum that satisfies the SUSY condition. In fact, the vast majority do not. Whether this is the case can be determined from the initial guess. If $z_{guess} - 1$ is so large that $\mathcal{O}(z-1)$ terms dominate $\log(z-1)$, then the expansion that lead to z_{guess} was not valid to begin with, and so the eight fluxes are redrawn.

To summarize, then, the steps of our search algorithm are:

1. Randomly draw eight integers independently from the interval $[-20, 20]$.

2. Compute the guess via eq. 4.2.6. If it is more than 0.5 away from conifold redraw the fluxes. Otherwise construct $u(x, y; F, H)$ using the patched period functions.

3. Minimize u using FindMinimum, with the real and imaginary parts of the guess as the starting point. (We further invoke the option that limits the search region to avoid Mathematica searching far away from the region of interest when there is no near conifold minimum, and/or extrapolating the periods so as to give artificial minima).

4. If a minimum is found, and that minimum is sufficiently close to the conifold,

we collect a variety of useful information including the list of fluxes, the minimum's location, the magnitude of u, and the axio-dilaton's location $\tau_{SUSY}(z_{min})$.

5. Repeat.

Lastly, it is necessary to filter these local minima of u. Since the imaginary part of the axio-dilaton is proportional to the inverse of the string coupling, any minima found during the search that have negative $\mathrm{Im}(\tau_{SUSY}(z_{min}))$ are unphysical. Removing these, the list of potential vacua is approximately cut in half. Next, only the zeros of u should be kept, as the evaluation of the axio-dilaton at 4.1.69 assumes vacua solve $D_I W = 0$. We eliminate minima whose u is above a threshold of 10^{-6}.

To compare vacua properly, particularly with regard to their locations in the the τ field space, we need to perform an $SL(2,\mathbb{Z})$ transformation that maps each vacua's τ value into the fundamental domain. A set of four integers $\{a, b, c, d\}$ is found such that the transformation,

$$\tau \to \frac{a\tau + b}{c\tau + d} \tag{4.2.9}$$

maps the axio-dilaton into the strip in the upper half-plane with both $\mathrm{Re}(\tau) < \frac{1}{2}$ and $|\tau| > \frac{1}{2}$. The vacuum's fluxes are then mapped as follows,

$$F_i \to aF_i + bH_i$$
$$H_i \to cF_i + dH_i.$$

This is the 4-dimensional incarnation of the original $SL(2,\mathbb{Z})$ symmetry enjoyed by the 10-dimensional type IIb supergravity action. In fact, one reason for formulating the theory in terms of the axio-dilaton is so this symmetry is made manifest. The transformation is stated for the total 3-form flux as,

$$G_{(3)} \to cG_{(3)} + d. \tag{4.2.10}$$

Performing the transformation also enables us to check for duplicate vacua. The transformation is not 1-to-1, so vacua with different fluxes prior to mapping may actually correspond to the same vacuum in the fundamental domain. Though possible, no instances of double counting were found among the vacua identified with our algorithm.

Finally, we impose the type IIb tadpole condition on the fluxes, eq. 4.1.30. This integral expression can be restated conveniently in terms the number of orientifold planes and D3-branes, and the dimensionless fluxes wrapping the mirror quintic's 3-cycles as

$$F \cdot Q \cdot H = \frac{1}{4} N_{O3} - N_{D3}, \tag{4.2.11}$$

where Q is the intersection matrix, and F and H are the vectors containing the four RR and four NSNS flux integers. The condition is often stated as an inequality by defining the maximum of the righthand side as the positive number L_{max},

$$F \cdot Q \cdot H \leq L_{max}. \tag{4.2.12}$$

We make an admittedly arbitrary choice of $L_{max} = 300$, and dispose of vacua whose fluxes combine via Q to violate this threshold. We are interested in the statistical features of flux vacua in the mirror quintic's moduli space as a probe of the landscape more broadly. So long as our results are not sensitive to the particular choice of L_{max}, we believe it is reasonable to relax the condition. We find this is the case and so proceed without concern for the actual maximum number of orientifold planes the mirror quintic can support.

The results for the masses and couplings given in the following section are for the largest random sample of vacua we found using this search algorithm and filtering. It consists of 1358 near conifold vacua whose complex structure and axio-dilaton's locations are shown in figure 4.2.

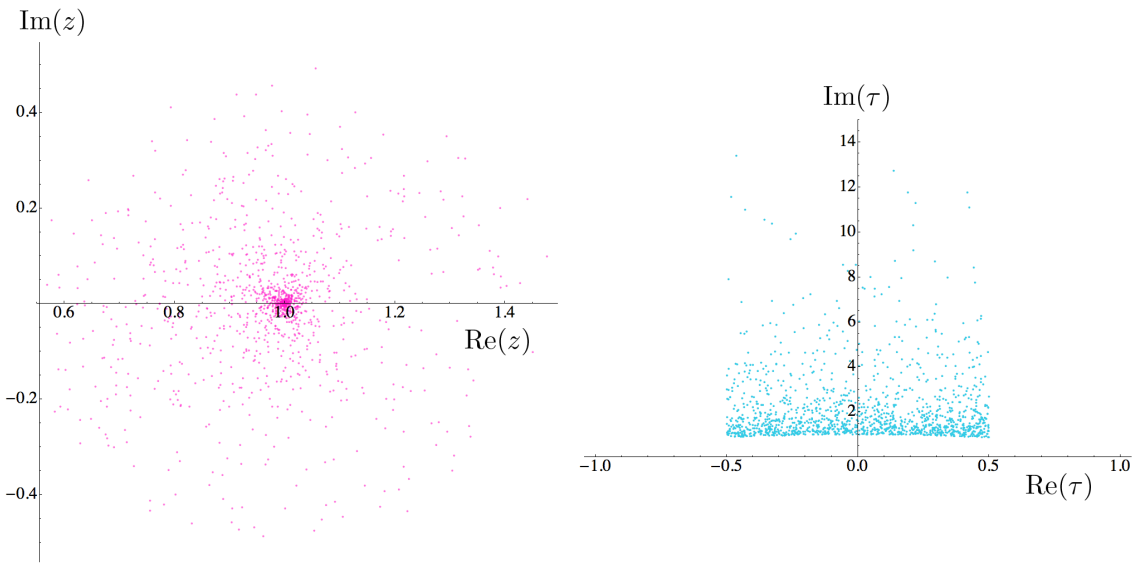

Figure 4.2: Complex structure and axio-dilaton vacuum locations for the random sample of 1358 vacua.

Computing Coefficients

Now that we have a random sample of flux vacua, we turn to our second computational task — obtaining the masses and couplings to quartic order in the corresponding ensemble of effective field theories. These are the data whose statistics we want to analyze. For a given model, the n^{th} order couplings are the n^{th} order Taylor coefficients of the corresponding scalar potential expanded about the model's vacuum and transformed appropriately so that the kinetic terms in all the effective field theories are canonical.

Though the vacuum axio-dilaton coordinate location in each model is fixed in terms of the vacuum's complex structure location, the axio-dilaton is a full degree of freedom. We fixed it as an explicit function of z in our search algorithm as a short-cut to finding the location of minima of the scalar potential. Here we leave τ as a variable in the scalar potential, and so have two complex degrees of freedom. The Hessian then is a 4×4-matrix, and the four masses come in two pairs due to the special structure of the mass matrix in no scale models, as we reviewed in section 4.1.

This structure is relevant to the higher order couplings because we need to report them in a basis which not only yields canonical kinetic terms but also diagonalizes the mass matrix. In this subsection we first discuss the field redefinitions,

$$\{z, \tau, \bar{z}, \bar{\tau}\} \to \{y_1, y_2, y_3, y_4\} \tag{4.2.13}$$

$$(z, \tau) \in \mathbb{C}^2, \quad y \in \mathbb{R}^4 \tag{4.2.14}$$

that accomplish this, and we then the numerical algorithm for evaluating the Taylor coefficients. Though the original complex coordinates are the simplest in which to evaluate the Taylor coefficients because we have expansions for the periods in $z-1$, it will still be necessary to design an efficient algorithm. This somewhat tedious exercise is discussed in the second half of this section after defining the specific transformation that is applied to each tensor of Taylor coefficients calculated with the algorithm.

To that end, we define the column vector of fields in our original complex basis,

$$\Phi \equiv \begin{pmatrix} z \\ \tau \\ \bar{z} \\ \bar{\tau} \end{pmatrix}. \tag{4.2.15}$$

The effective field theory is obtained by expanding about a homogeneous background, Φ_{vac}. We begin by writing, $\Phi = \Phi_{vac} + B\Psi$, where the matrix B will serve to canonically normalize the kinetic terms. We have,

$$\mathcal{L}(\Phi) = \mathcal{L}(\Phi_{vac}) + \partial_\mu \Psi^\dagger B^\dagger (G_{vac} + \mathcal{O}(\Psi)) B \partial^\mu \Psi - V(B\Psi) \tag{4.2.16}$$

$$= \mathcal{L}_{vac} + \partial_\mu \Psi^\dagger B^\dagger G_{vac} B \partial^\mu \Psi - \frac{1}{2} \Psi^\dagger B^\dagger M B \Psi + \mathcal{O}(\Psi^3) \tag{4.2.17}$$

where $G(\Phi)$ is the Hermitian matrix containing the components of the Kähler metrics.

Specifically,

$$G(\Phi) = \begin{pmatrix} \mathcal{K}_{z\bar{z}} & 0 & 0 & 0 \\ 0 & \mathcal{K}_{\tau\bar{\tau}} & 0 & 0 \\ 0 & 0 & \mathcal{K}_{\bar{z}z} & 0 \\ 0 & 0 & 0 & \mathcal{K}_{\bar{\tau}\tau} \end{pmatrix}. \tag{4.2.18}$$

and G_{vac} is that evaluated at the vacuum.

The effective field theory will have canonical kinetic terms provided

$$B^{\dagger} G_{vac} B = 1. \tag{4.2.19}$$

This is easily accomplished by rescaling the fields. A normalized complex basis, which we denote $\{\xi, \sigma\}$, will be useful in discussing our results so we define one during this otherwise intermediate step. It will be convenient, in addition, to shift the normalized complex structure field so that it is zero at the conifold. Thus we write,

$$z = 1 + C_1 \xi \ , \quad \tau = C_2 \sigma \tag{4.2.20}$$

where C_1 and C_2 are the constants $1/\sqrt{\mathcal{K}_{z\bar{z}}|_{vac}}$ and $1/\sqrt{\mathcal{K}_{\tau\bar{\tau}}|_{vac}}$, respectively (we drop the superscripts on the Kähler potentials indicating the complex structure and axio-dilaton as its diagonal form in z and τ renders them superfluous in the metric). Then,

$$\Psi \equiv \begin{pmatrix} \xi - \xi_{vac} \\ \sigma - \sigma_{vac} \\ \bar{\xi} - \bar{\xi}_{vac} \\ \bar{\sigma} - \bar{\sigma}_{vac} \end{pmatrix}. \tag{4.2.21}$$

The matrix M contains the partial derivatives of the scalar potential (in the original coordinates) evaluated at the vacuum, but with the appropriate ordering so that it is Hermitian. We take the ordering $(z, \tau, \bar{z}, \bar{\tau})$ for the columns, so our rows

have the barred ordering $(\bar{z}, \bar{\tau}, z, \tau)$. Using the like orderings for columns and rows will not yield a Hermitian matrix, only a symmetric one. We included the subscripts in the definition of G in part to emphasize this.

The "rescaled" mass matrix, $B^\dagger M B$, is not in general diagonal. This is because the scalar potential nontrivially mixes the complex structure with the axio-dilaton so that mixed partials, like $\partial_z \partial_\tau V$, do not vanish at the vacuum. We choose first to transform to a set of four real fields, and then to diagonalize the resulting real and symmetric matrix by an orthogonal transformation (for reasons that will become clear momentarily.)

We express Ψ as

$$\Psi = TX, \text{ where } X = \frac{1}{\sqrt{2}} \begin{pmatrix} \mathrm{Re}(\xi - \xi_{vac}) \\ \mathrm{Im}(\xi - \xi_{vac}) \\ \mathrm{Re}(\sigma - \sigma_{vac}) \\ \mathrm{Im}(\sigma - \sigma_{vac}) \end{pmatrix}. \tag{4.2.22}$$

Note that T it is unitary. Lastly, we take

$$X = OY \tag{4.2.23}$$

where O is the orthogonal matrix containing the (normalized) eigenvectors of $T^\dagger B^\dagger M B T$ as columns. That is,

$$Y^T O^T T^\dagger B^\dagger M B T O Y = Y^T D Y = \sum_{i=1}^{4} m_i^2 y_i^2 \tag{4.2.24}$$

where D is diagonal.

The full transformation to the real basis that simultaneously diagonalizes the

Hessian and canonically normalizes the kinetic terms (locally) is

$$\tilde{J} : (\Phi - \Phi_{vac}) \to Y$$
$$\tilde{J} = (BTO)^{-1}$$

So, if we compute the rank three and four symmetric tensors of partial derivatives of the scalar potential at the vacuum in the original complex coordinates,

$$A_{ijk} = \frac{\partial}{\partial \Phi^i} \frac{\partial}{\partial \Phi^j} \frac{\partial}{\partial \Phi^k} V \Big|_{\Phi_{vac}}, \tag{4.2.25}$$

we need to transform according to the standard tensor transformation law,

$$A_{i'j'k'} = \frac{\partial \Phi^i}{\partial Y^{i'}} \frac{\partial \Phi^j}{\partial Y^{j'}} \frac{\partial \Phi^k}{\partial Y^{k'}} A_{ijk} \tag{4.2.26}$$
$$= J^i_{i'} J^j_{j'} J^k_{k'} A_{ijk}, \tag{4.2.27}$$

with J defined as the inverse of $\tilde{J}$, and similarly for the fourth order coefficients, $A_{i'j'k'l'}$ as well. By choosing the particular unitary transformation that diagonalizes the rescaled mass matrix and yields a basis of real fields, y_i, we avoid concerning ourselves about reordering of the entries of the complex symmetric rank three and four tensors we compute numerically. This final task, evaluating the Taylor coefficients in the original complex field coordinates, may seem trivial. After all, the vacua reside near the conifold point where the period functions are polynomial in $(z-1)$ and/or $(z-1)^n \log(z-1)$, so we never need evaluate the divergent Meijer-G's in the scalar potential resulting from derivatives of Π_0 (and $\bar{\Pi}_0$). However, the seemingly mundane exercise of symbolically simplifying the near conifold scalar potential resulting from plugging in the period expansions and its partial derivatives proves prohibitive.

This is mainly due to the cumbersome way the scalar potential mixes up the

periods and the relative factors of

$$\sim \frac{\partial^m \Pi^\dagger Q^{-1} \partial^n \Pi}{(\Pi^\dagger Q^{-1} \Pi)^{m+n}} \tag{4.2.28}$$

between its summands. Since we are plugging in eighth order expressions for the periods, the number of terms that need to be expanded, collected and organized is large. Rather than try to undo the natural packaging of the period functions, we make use of it.

Our strategy is to express each entry in the tensors we wish to evaluate, the A_{ijk} and A_{ijkl}, in terms of simple combinations of a small number of blocks. Each block is built out of smaller elements, which include the periods, their derivatives and combinations thereof (the Kähler potential for the complex structure and its partial derivatives). For each model in the ensemble, we evaluate the periods and their derivatives up to fifth order once. The values in this array are then combined appropriately to obtain the rest of the elements needed to construct the blocks. The blocks are then assembled into each entry required by the tensors. Essentially, we are exploiting the fact that many expressions appear repeatedly within a given entry and across entries, and so we need not evaluate them repeatedly.

The blocks consist of all the Kähler covariant derivatives of the superpotential, F_I, and their partial derivatives up to third order taken with respect to any of the complex fields. Some of these are zero, for instance $\partial_{\bar{\tau}} F_z$, but note $\partial_{\bar{z}} F_z$ is in general non-vanishing. Since the scalar potential is

$$V = e^{\mathcal{K}} \left(\mathcal{K}^{z\bar{z}} F_z \bar{F}_{\bar{z}} + \mathcal{K}^{\tau\bar{\tau}} F_\tau \bar{F}_{\bar{\tau}} \right) \tag{4.2.29}$$

its third and fourth order partial derivatives involve several terms linear in F_I. All such contributions vanish however because the SUSY condition, $F_I = 0$, is satisfied at all the vacua. By only retaining those terms in A_{ijk} and A_{ijkl} that have at least one

partial derivative on F_I and at least one on its conjugate we have more manageable expressions for each Taylor coefficient that need to be combined.

The individual blocks are compact when expressed in terms of the elements. For example,

$$\partial_z \partial_{\bar{z}} \partial_\tau F_z = \partial_z \partial_{\bar{z}} \partial_\tau (F - \tau H) \cdot (\Pi' + \mathcal{K}_z \Pi) \tag{4.2.30}$$

$$= -H \cdot (\Pi'' + \mathcal{K}_{z\bar{z}} \Pi' + \mathcal{K}_{zz\bar{z}} \Pi). \tag{4.2.31}$$

This approach enables us to compute both rank 3 and 4 tensors for the entire sample of 1358 vacua in time of order tens of minutes.

Lastly, we note that the form of the Hessian outlined in subsection 4.1 is confirmed by comparing that obtained by direct differentiation with that built from the metric and (separately constructed) Z and $\bar{Z}$ matrices in the original noncanonical basis. The percent deviation between the eigenvalues of the two are on the order of 10^{-13}.

4.3 Results

In this section we analyze the distributions of masses and couplings for a collection of 1358 vacua, found using the vacuum hunting algorithm described in subsection 4.2. There is a great deal of structure built in from the get-go. The task is to untangle the randomness that is present from that structure. As indicated in subsection 4.1, the no-scale structure for a theory with N complex moduli is responsible for pairing the $2N$ scalar masses of the effective field theory.

The association of each mass pair with a single one of the complex scalars (for us, either z or τ) is *not* expected, a priori, because of the mixing between the axio-dilaton and the complex structure in the scalar potential.

However, for near conifold flux vacua in the mirror quintic's moduli space that satisfy the SUSY condition, $D_I W = 0$, the two scalar fields *do* approximately separate;

ever more so as the vacuum-to-conifold distance is diminished. Tied to this cleaving of the field space is also a scale separation between the associated axio-dilaton and complex structure mass pairs. We observe that such a hierarchy percolates through third and fourth order couplings. All this structure, nearly universal across our ensemble, can be traced back to a single quantity: the mirror quintic's Yukawa coupling.

We will show that the larger the Yukawa coupling, the more exaggerated this structure becomes. Its singularity, located precisely where vacua accumulate — at the conifold point — is responsible for the expected pattern of near conifold mass and couplings dominating the ensemble. We use the qualifier "expected" because there is one random ingredient: the vev of the superpotential. Depending on your point of view, it muddies otherwise sharply defined features, or provides the possibility of freedom from rigidity (albeit a vanishingly small possibility as the conifold is approached).

In this section we first establish the distance of a vacuum from the conifold as the key quantity controlling the degree to which structure is amplified or diluted. Next, we build intuition for the mass pairs and their distributions. Finally we present the hierarchies and correlations observed in the data for cubic and quartic couplings, which similarly is attributable to the singular dependence on the vacuum-to-conifold distance. For ease of discussion, we will loosely refer to the magnitude of a vacuum's canonical complex structure coordinate, $|\xi_{vac}|$, as its distance to the conifold in moduli space. More precisely, this distance is a monotonically increasing fucntion of $|\xi|$, but is not identically equal to it. During our investigation we developed a Random Matrix Model that accurately captures this particular combination of both regularity and randomness. We comment on the possible generalizations of these results to models with more complex structure moduli in the Discussion section.

Masses

Since the SUSY condition is satisfied at our vacua, the complex 2×2-matrix $Z_{IJ} \equiv D_I D_J W$ is the matrix of vacuum values of the partial derivatives of F_I, specifically,

$$Z = \begin{pmatrix} \partial_\tau F_\tau & \partial_z F_\tau \\ \partial_\tau F_z & \partial_z F_z \end{pmatrix}. \tag{4.3.1}$$

Not all entries in this matrix are independent. It's form is restricted because there is no mixing between the complex structure and the axio-dilaton at the level of the Kähler potential ($\mathcal{K}_{z\tau} = 0$) and also because $\mathcal{K}_{\tau\bar{\tau}} = -{\mathcal{K}_\tau}^2$. These two, together with the SUSY condition in τ, imply Z has the form,

$$Z = \begin{pmatrix} 0 & Z_{01} \\ Z_{10} & Z_{11} \end{pmatrix}, \tag{4.3.2}$$

where the entries are complex valued (and $Z_{01} = Z_{10}$).

The two nontrivial entries, it turns out, are related by a known analytic function when the canonical basis is used (the fields we labeled ξ and σ, whose corresponding Z matrix is Z^{can}). For compactifications of type IIb on general Calabi-Yau the following equation is valid at solutions to $D_I W = 0$,

$$Z_{IJ} = \mathcal{F}_{IJK} \bar{Z}^{0K} \tag{4.3.3}$$

in a basis where the fields in the effective action are canonically normalized. The $\mathcal{F}_{IJK}$ in eq. 4.3.3 are the Yukawa couplings between the Calabi-Yau's complex structure moduli and their fermionic counterpart in the effective field theory. Since the mirror quintic has a single complex structure modulus we have the direct proportionality,

$$Z_{11} = \mathcal{F}_{111} \bar{Z}^{01}. \tag{4.3.4}$$

where we've suppressed the "can" superscripts.

The Yukawa coupling is singular at the conifold point. Its exact analytic form was found by Candelas and de la Ossa (see for e.g. [52]). Stated in terms of their complex structure field coordinate before canonical normalization, ψ, which is related to ours by $z = \psi^{-5}$ the Yukawa coupling takes the form

$$\kappa_{\psi\psi\psi} = \left(\frac{2\pi i}{5}\right)^3 \frac{5\psi^2}{1-\psi^5}. \tag{4.3.5}$$

Note that while zero and infinity switch under the coordinate transformation between ψ and z, the conifold point is fixed. The conifold singularity in eq. 4.3.5 persists through the coordinate transformation to our $\mathcal{F}_{111}$, and manifests as one naively expects (as a $1/\xi$ divergence) with minor modification. This is because the prepotential from which $\kappa_{\psi\psi\psi}$ derives is the same as ours.

It is useful to briefly sketch the calculation of Candelas and de la Ossa in order to understand the origin of the divergence, as well as its leading order form in our coordinates. They define a set of functions, "Wronskians", in terms of derivatives of the prepotential. The kth Wronskian is given by

$$W_k = \mathcal{Z}^i \frac{d^k}{d\psi^k}\mathcal{G}_i - \mathcal{G}^i \frac{d^k}{d\psi^k}\mathcal{Z}_i \tag{4.3.6}$$

where $\mathcal{Z}^i$ and $\mathcal{G}_i$ are an intersecting pair of periods (in an integral and symplectic basis). Since there are four nontrivial cycles, i ranges from 1 to 2. The prepotential is

$$\mathcal{G} = \frac{1}{2}\mathcal{Z}^i\mathcal{G}_i. \tag{4.3.7}$$

A crucial next step is to identify the Yukawa coupling,

$$\kappa_{\psi\psi\psi} = \int \Omega \wedge \frac{d^3\Omega}{d\psi^3}, \tag{4.3.8}$$

with the third Wronskian. Together with the properties of Calabi-Yau, particularly the fact that the periods solve the Picard-Fuchs equation, they obtain an ordinary differential equation for W_3, whose solution is given in eq. 4.3.5.

When the fields in the effective action are canonically normalized, the Yukawa coupling receives a total factor of the inverse vacuum Kähler metric for the complex structure raised to the *three halves*; one half power from the rescaling of the scalar field and one full power from the transformation of the fermion (one half power for each of the two factors of the fermion in the original interaction term $\sim \kappa\varphi\chi\chi$).

We've already accounted for one half of the total three halves by canonically normalizing our z coordinate. This implies the ratio of our Z_{11}^{can} to Z_{01}^{can} will have a leading order behavior of $1/(\xi \log \xi)$, since the Kähler metric goes like $\log(\xi)$ near the conifold point, $\xi = 0$. In figure 4.3 we display the actual vacuum data for the magnitude of this ratio against the conifold distance. A numerical fit to the leading order form is overlaid in red. Note the exceedingly tight agreement between the two. Essentially, the $\sim \frac{1}{\xi}$ dependence comes from a contribution $\sim \Pi_3 \frac{d^3}{d\xi^3}\Pi_0$, since

$$\Pi_3 \frac{d^3}{d\xi^3}\Pi_0 = \mathcal{O}(\xi)\frac{d^3}{d\xi^3}\left(\mathcal{O}(\xi)\log\xi + \text{analytic}\right) \tag{4.3.9}$$

$$= \mathcal{O}(\xi)\left(\mathcal{O}(\xi)\frac{d^3}{d\xi^3}\log\xi + \mathcal{O}(1)\frac{d^2}{d\xi^2}\log\xi + \mathcal{O}(1)\right) \tag{4.3.10}$$

$$= \mathcal{O}(\xi)\mathcal{O}(1/\xi^2) \tag{4.3.11}$$

$$= \mathcal{O}(1/\xi) \tag{4.3.12}$$

Our vacua live in a region where $|\mathcal{F}| \gg 1$, so Z_{11} always dominates Z_{01}. This is consequential for the mass spectra and coordinate transformation that enters into the computation of the subsequent higher order couplings. Expressed in terms of the magnitude of the Yukawa coupling (where we've suppressed the "111" indices), the

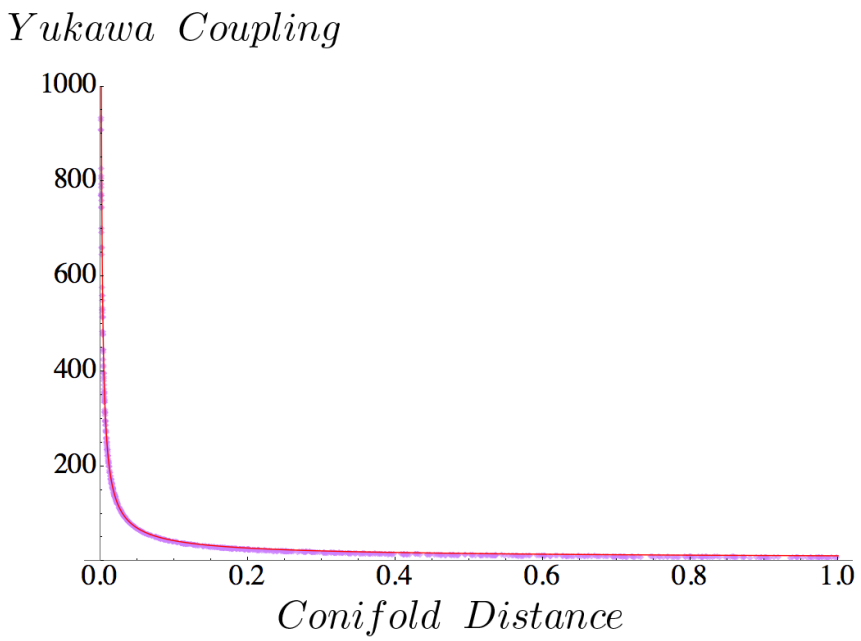

Figure 4.3: Plotted in light purple is the ratio of the magnitudes of the entries of the Z matrix for our vacua (the 11 entry over the 01 entry) on the vertical, against $|\xi_{vac}|$ which is a measure of the vacuum to conifold distance. Special geometry implies that this ratio ought to be the magnitude of the Calabi-Yau Yukawa coupling. The function plotted in red is a numerical fit of the data to the leading order form of the mirror quintic's $|\mathcal{F}|^2$. Note the extremely good agreement between the two, and the divergence at the conifold point, precisely where vacua accumulate.

$Z\bar{Z}$ matrix takes the form,

$$Z\bar{Z} = |Z_{01}|^2 \begin{pmatrix} 0 & |\mathcal{F}|e^{-i\delta} \\ |\mathcal{F}|e^{+i\delta} & |\mathcal{F}|^2+1 \end{pmatrix}, \tag{4.3.13}$$

whose eigenvalues come in the pair,

$$\Lambda_\pm^2 = \frac{|Z_{01}|^2}{2}\left(|\mathcal{F}|^2+2 \pm |\mathcal{F}|\sqrt{|\mathcal{F}|^2+4}\right). \tag{4.3.14}$$

The larger of these is always Λ_+^2, so, in our labeling convention for the λ_i's we identify $\lambda_1^2 = \Lambda_+^2$, and $\lambda_2^2 = \Lambda_-^2$.

Note that in either limit, $|\mathcal{F}| \gg 1$, or the reverse, we have $\Lambda_+^2 \gg \Lambda_-^2$. If $|\mathcal{F}| \gg 1$

the eigenvector associated with the larger eigenvalue is almost entirely contained within the span of the complex structure field, and in the opposite limit within that of axio-dilaton field. Since we always have the former case, the largest eigenvalue of $Z\bar{Z}$, λ_1^2, is associated always with the complex structure, and the smaller, λ_2^2, with the axio-dilaton. An immediate consequence of this is the cleaving of the eigenspace of the Hessian in two.

One subspace is spanned almost entirely by the complex structure and is associated with the mass pair $m_{1\pm}^2$, while the other is spanned by the axio-dilaton and is associated with $m_{2\pm}^2$. This is because the 2×2 blocks entering into the diagonalization of the Hessian, which would otherwise mix these two fields, are approximately equal to the identity. These 2×2 blocks in the complex field coordinates of section 4.1 are U and its Hermitian conjugate. In the real field coordinates of section 4.2 they form two by two blocks in O, upon a reordering of rows and columns.

Whether or not the hierarchy in the λ_i leads to a hierarchy between the two mass pairs — a heavy complex structure pair and a light axio-dilaton pair — depends on the relative sizes of $|W|$, λ_1 and λ_2. More precisely, we begin by noting there is no ambiguity about the heaviest mass. It is always m_{1+}^2, which for us is always associated with z. It's partner (still associated with z) need not be second heaviest, however. To see why note that

$$\begin{aligned}(\lambda_1 - |W|)^2 &< (\lambda_2 \pm |W|)^2 \\ \lambda_1^2 - \lambda_2^2 &< 2|W|(\lambda_1 \pm \lambda_2) \\ \lambda_1 \mp \lambda_2 &< 2|W|.\end{aligned}$$

So, if half of the gap between the λ_i is less than the magnitude of the vacuum superpotential the second heaviest of the four masses is the larger of the axio-dilaton masses, m_{2+}. If the average of the λ_i is *also* less than the magnitude of the super-

potential then the third heaviest mass is the lighter of the axio-dilaton pair, and the lightest of the four masses is the lighter of the complex structure pair. To summarize, the naive/expected ordering among the masses,

$$m_{1+}^2 > m_{1-}^2 > m_{2+}^2 > m_{2-}^2 \tag{4.3.15}$$

is realized if the difference condition is not met (large discrepancy between the λ_i's).

The middle two masses swap places,

$$m_{1+}^2 > m_{2+}^2 > m_{1-}^2 > m_{2-}^2 \tag{4.3.16}$$

if the gap condition is met but the average condition is *not*. Lastly, if both conditions are met the lighter complex structure mass shuffles all the way to the bottom of the mass scale,

$$m_{1+}^2 > m_{2+}^2 > m_{2-}^2 > m_{1-}^2. \tag{4.3.17}$$

As we've seen, the difference in scale between the two distinct nontrivial entries of Z diverges as the conifold point is approached. Since the larger the scale difference the larger the gap between the λ_i will be, we expect the likelihood of the gap condition being met to diminish as the conifold point is approached. This is precisely what we find. In figure 4.4 we plot $\lambda_1 - \lambda_2$ divided by twice the magnitude of the superpotential against the conifold distance for each vacuum. A horizontal line at 1 is indicated by the dashed line, so points above this line fail the gap condition and the naive order exists, while those below have at least one rightward shift of m_{1-}^2 down the hierarchy in 4.3.15.

There are two important observations. First, the vacua migrate upward as the conifold is approached making the condition ever more unlikely to be satisfied, verifying our expectation. Second, there are nonetheless a few vacua for whom the

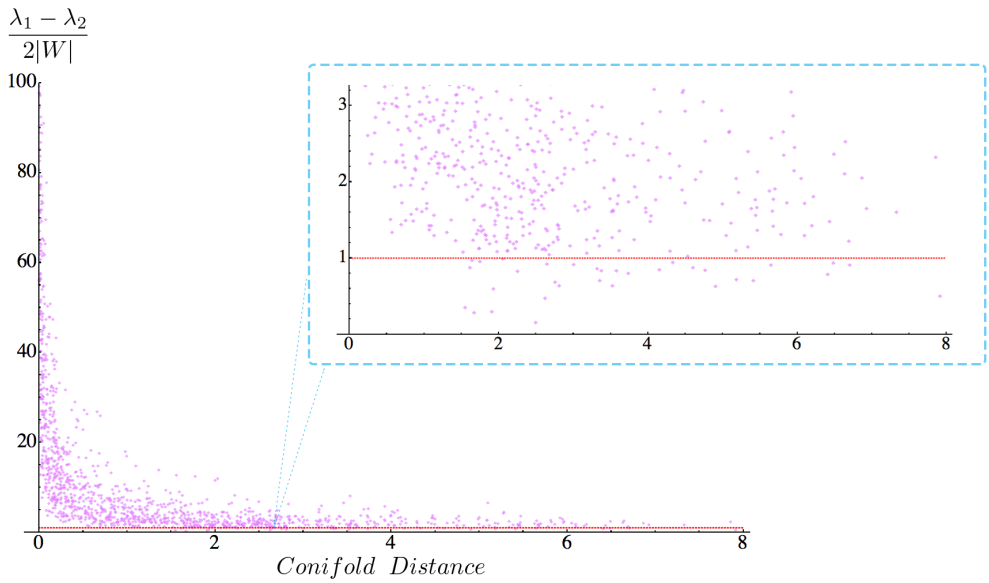

Figure 4.4: The difference between the λ_i divided by twice the vev of the superpotential vs. $|\xi_{vac}|$, illustrating the key quantity in the hierarchy condition. Data points that fall below the dashed pink line do not satisfy the condition and have a mass hierarchy that differs from the expected one by at least one swap. Note that as the conifold distance decreases the data points float upwards, confirming the expectation (based on the divergence of the Yukawa coupling) that the condition becomes ever more difficult to satisfy as the location of the vacuua approaches the conifold.

condition is met. Specifically, we find 33 out of 1358 such instances, or 2.4%. The image toward the upper-right of figure 4.4 shows the portion of the plot focused near the bottom (with exactly 33 points below the dashed line). The random ingredient that allows for vacua to dip below the threshold for mass swaps is the magnitude of the superpotential. The vev shows no dependence on the distance of the vacuum from the conifold. This is shown in figure 4.5.

We reiterate that in all cases, including these nonconformist 33, the Hessian's eigenspace enjoys an approximate separation between the complex structure field space, and axio-dilaton field space. The angle between the subspace spanned by one of the moduli — ξ or σ — and that spanned by the two eigenvectors associated with one of the mass pairs — $m^2_{1\pm}$ or $m^2_{2\pm}$ — can be computed. In figure 4.6 we display

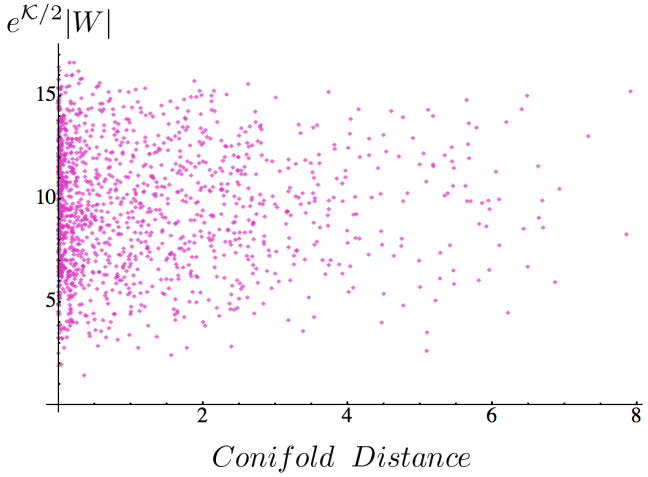

Figure 4.5: A scatter plot of the magnitude of the vev of the superpotential vs. ξ_{vac}. Note that the two bear no significant dependence on one another. Data points become more clustered as one moves toward the peak or either quantity's distribution *independently*.

the histogram of angles between the complex structure subspace and the $i = 1$ mass pair for all vacua. The mean angle is 5.85 degrees, indicating that the subspaces are approximately parallel. The identical statement holds for the axio-dilaton subspace and the second mass pair. A visual depiction of the subspaces is included to the right of the histogram, and uses the mean angle.

Now that we have established that this separation between z and τ lines up with the half-way marker between the masses in virtually all cases, we turn to developing intuition for each pair. We display the distributions of λ_1 and λ_2 in figure 4.7, and of $|W|$ in figure 4.8. We have absorbed a factor of the vev of $e^{\mathcal{K}/2}$ into the definitions of each of these three, as they are the correct Kähler invariant quantities, i.e. the physically relevant values to consider.

As expected, the λ_1 distribution's scale is significantly larger than λ_2's due to the accumulation of vacua where the Yukawa coupling diverges. Specifically, we find a difference of two to three orders of magnitude. The characteristics of the corresponding mass pairs will depend on the relative sizes of the λ_i to $|W|$ individually.

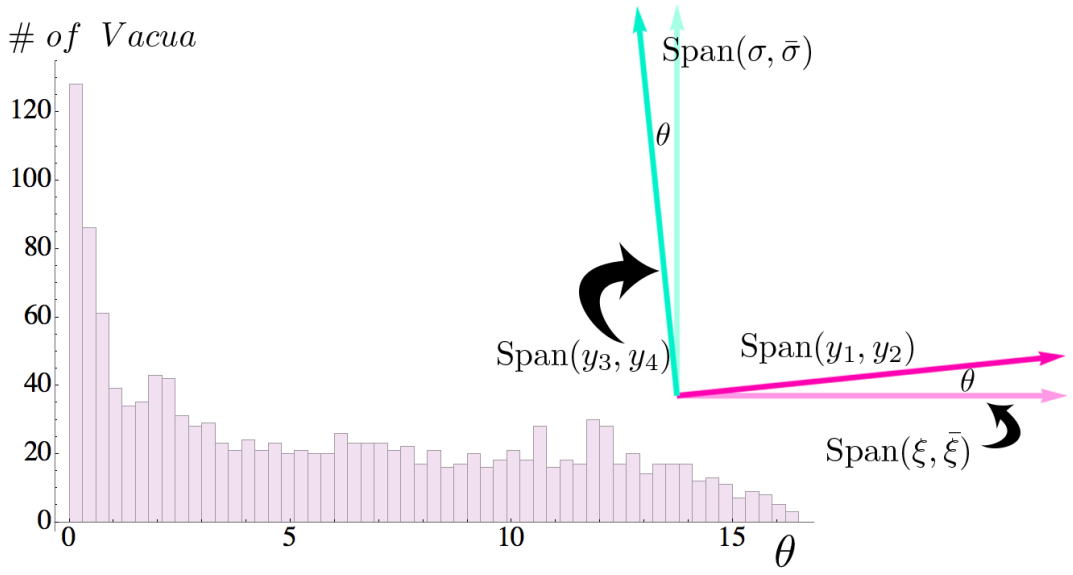

Figure 4.6: A distribution of relative angle, θ, between the complex structure subspace of the moduli space and the $m^2_{1\pm}$ eigenspace, which is identical to that between the axio-dilaton subspace and the $m^2_{2\pm}$ eigenspace. The fact that the angles for all vacua are small indicates that the former pair are approximately parallel to each other, and likewise for the latter. A visual aid depicting this split of the eigenspace is shown to the right using the mean value of this angle, which is 5.85 degrees for our vacua.

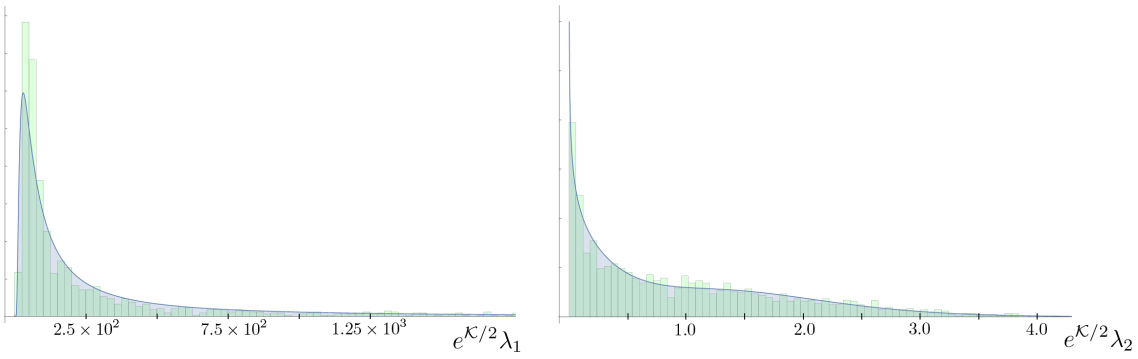

Figure 4.7: Histograms of the Kähler independent λ_i for our ensemble of vacua. Estimated distributions obtained numerically are plotted over each histogram in blue.

We find a superpotential that is approximately one order of magnitude larger than λ_2, but one order smaller than λ_1 (several orders smaller for vacua in the tail).

The resulting two mass pairs are displayed in figures 4.9 and 4.10, with the larger mass of each couple plotted on the horizontal. We immediately notice that the com-

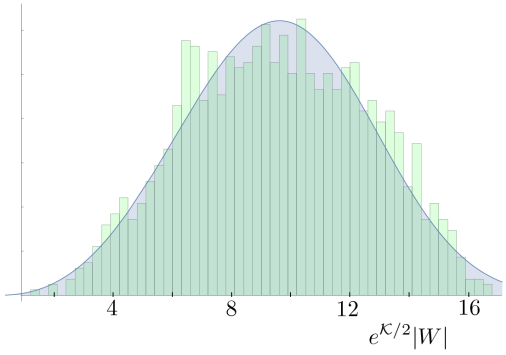

Figure 4.8: The histogram of the Kähler independent vevs of the superpotential for our ensemble. The estimated distribution obtained numerically is overlaid.

plex structure mass pair looks more tightly correlated than the axio-dilaton pair. This, as we'll analyze more precisely later, is entirely an artifact of the difference in scale between the two field's pairs; an effect that is exaggerated by the particularly wide range needed to include all of the z mass data points in figure 4.9. The distribution (for both members of the z pair) peaks at much lower values, around 100. A fairer comparison with the τ masses, which are more widely/evenly distributed, would come from zooming in and excluding the z masses' long tails. A partial zoom is shown in the ellipsoidal window on the right in figure 4.9. A more refined analysis will nonetheless reveal that the two fields have virtually identical levels of *relative* degeneracy between the members of their respective pairs.

Turning to the τ data points shown in figure 4.10, note firstly that they fill in more of the triangular half below the diagonal *including* the region immediately beneath the diagonal. This indicates that there is a larger variety among the dimensionful mass gaps for the axio-dilaton, than for the complex structure. There are more instances of near equality between the masses — in an absolute/dimensionful sense — as compared to those in the lower range of z's distribution (there are far more data points along the diagonal boundary in the axio-dilaton's scatter plot than in the zoomed in complex structure's). There are also more instances of large differences for the τ pairs than

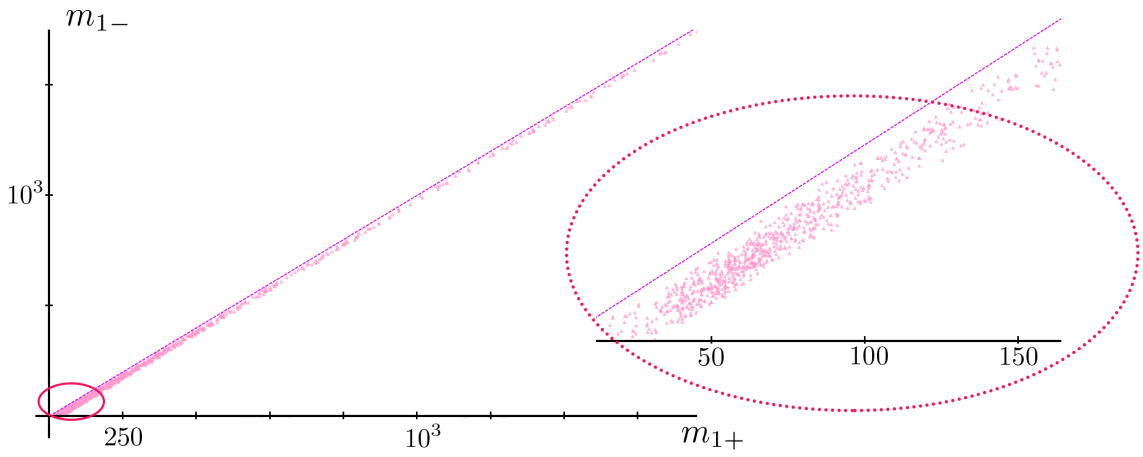

Figure 4.9: A scatter plot for the mass pair associated with the complex structure modulus, with the heavier of the two, m_{1+}, on the horizontal and the lighter, m^{1-}on the vertical. A dashed line with slope one is plotted in purple. The portion of the plot focused where the masses distributions peak (i.e. where the data points cluster) is shown to the right.

the z's. Clearly, the latter statement remains true when z's tail is considered, but the former may not. These distinctions make sense given the distributions for the λ_i and $|W|$. Essentially, the τ masses are dominated by the superpotential, which has a rather large spread and is not skewed (roughly Gaussian). This leads to a more uniform distribution horizontally throughout the triangle.

The lack of space between data points and the diagonal is due to the fact that λ_2 peaks very near zero, and decays quickly before its decline steadies around ~ 0.5. This increases the frequency of λ_2's that are completely negligible compared to $|W|$, and thus very nearly equal masses among the given pair. The axio-dilaton pairs' greater vertical extent throughout the triangle is due to the combination of the larger spread in λ_2 and $|W|$, and the fact that the intervals where they are supported partially overlap. Thus, more instances of close competition between λ_2 and $|W|$ occur than for λ_1 and W.

These observations are helpful for building intuition, but a comparison of the *degree* of degeneracy in the mass pairs of the two fields should involve dimensionless

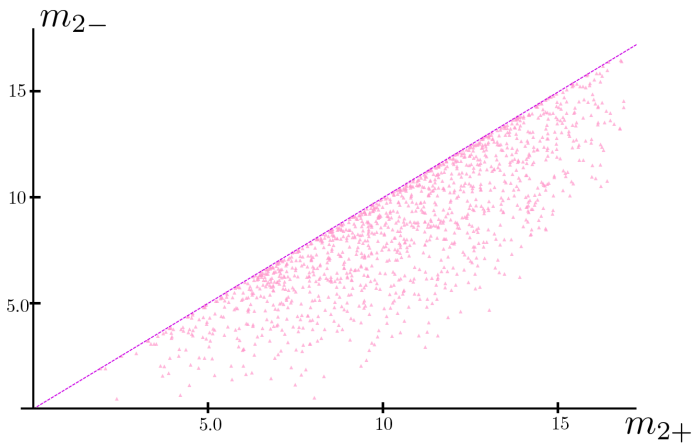

Figure 4.10: The analogous scatter plot for the mass pair associated with the axio-dilaton as that in figure 4.9.

mass gaps, namely those scaled by the mean of the masses in each pair. Starting with the difference in the squared masses of the two members in the ith pair, $4\lambda_i|W|$, one finds the limiting form,

$$\frac{\Delta m_i/2}{m_{i,avg}} = \sqrt{\frac{\lambda_i|W|}{\lambda_i^2+|W|^2}} \tag{4.3.18}$$

$$\lambda_i \ll |W| : \quad \frac{\Delta m_i/2}{m_{i,avg}} \rightarrow \frac{\lambda_i}{|W|} \ll 1 \tag{4.3.19}$$

$$\lambda_i \gg |W| : \quad \frac{\Delta m_i/2}{m_{i,avg}} \rightarrow \frac{|W|}{\lambda_i} \gg 1 \tag{4.3.20}$$

That the result is the same for both limits simply reflects the fact that one can equally well view λ_i as the degeneracy breaking term as one can $|W|$. A small λ_i compared to $|W|$ yields a mass pair $m_{i\pm} \approx |W| \pm \epsilon$, and the reverse yields a mass pair $\approx \lambda_i \pm \epsilon$.

Now, we may consider a probability density for each modulus as a function of the rescaled half mass gaps. For a given one of the moduli its value integrated over an interval $[a, b]$ would yield the probability of finding a vacuum for whom that modulus' associated masses each lie within $(b-a)m_{i,avg}$ of their mean, $m_{i,avg}$. We can then consider a cumulative density function obtained by integrating the probability density from $a = 0$. In figure 4.11 we display the histograms for our data corresponding to

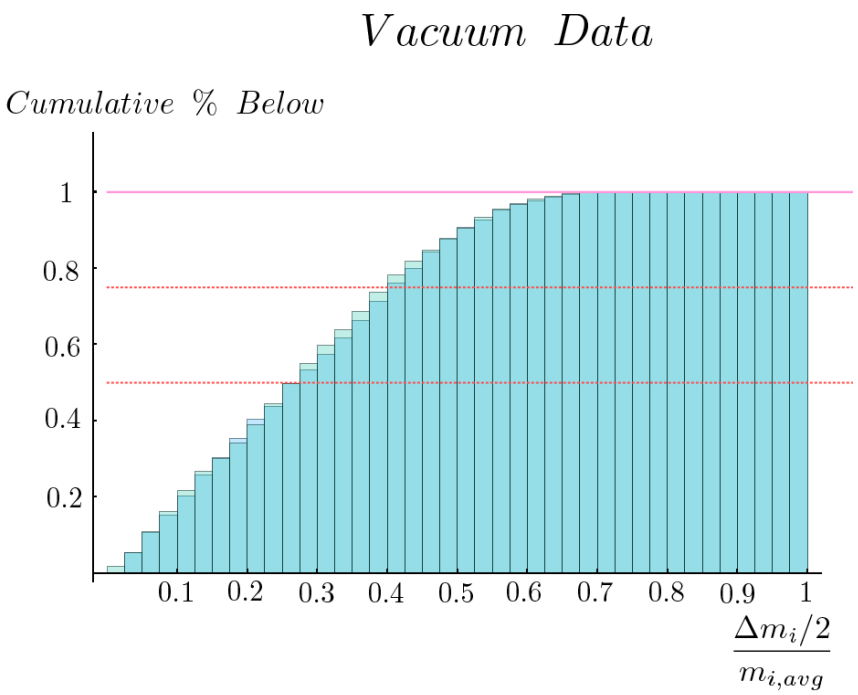

Figure 4.11: The cumulative relative mass gaps for each pair of masses, $m_{i\pm}$. The pair associated with the axio-dilaton is shown in on top in the darker shade of blue, while that associated with the complex structure is shown behind in the lighter turquoise color. The two are nearly identical meaning that the relative degree of non-degeneracy between the masses in a given pair is distributed in the same manner across the vacua of our ensemble, regardless of with which of the moduli the mass pair is associated.

the cumulative density functions (their discrete analogs) for our sample of vacua.

Notice that the complex structure and the axio-dilaton's histograms are virtually indistinguishable. They both achieve 50% within a threshold of 0.26, and continue to rise together in step with 75% of both fields having scaled gaps within the threshold of 0.40. This assessment of relative degeneracy, or relative spread, is not evident from looking at the scatter plots alone.

The structure and patterns we've encountered in the masses clearly won't be replicated with an ordinary Random Matrix Model where the Hessian for each vacuum is taken to be Wirshart — a Hermitian random matrix that is positive definite by construction. One essentially "squares" a random (Wigner) matrix, A, which is not in general Hermitian, by multiplying it with its complex conjugate. The entries of

the Wigner matrix are taken to be independent and identically distributed, that is drawn from an $\mathcal{O}(N^2)$-dimensional Gaussian.

In light of the analytic form of the Hessian with which we begin, and the limiting behavior of one of its essential building blocks, Z, for near conifold vacua, we design a different Random Matrix Model. We've seen three (Kähler independent) parameters are ultimately in control. These are (1) the proximity of a given vacuum to the conifold point, (2) its value of $e^{\mathcal{K}/2}|Z_{01}|$ and (3) its value of $e^{\mathcal{K}/2}|W|$. We should be able to mimic the actual mass data with a random sample of these triples. The simplest case would be to treat each parameter independently.

We saw earlier that control parameters (1) and (3) do not appear to depend on one another, as indicated by figure 4.5. A similar scatter plot for (1) and (2) is displayed in the right panel of figure 4.12, demonstrating their lack of correlation. The plot for (2) and (3) shows a sharp cutoff because the tadpole condition forbids these data points from leaving the quarter circle. It can be shown that the tadpole condition implies,

$$|Z_{01}|^2 + |W|^2 \leq L_{max} \tag{4.3.21}$$

in Gaussian normal coordinates.

The radius of the arc plotted in figure 4.12 is indeed $\sqrt{L_{max}} = \sqrt{300}$. Within this region however the data points vary independently. The empty bands along both axes are simply a reflection of the fact that the two distributions are peaked away from zero, with relatively little of their support coming from the interval $\approx [0, 5]$. Just as with the other two scatter plots, the density of data points increases as either parameter is pushed towards the value where its distribution peaks while the other is held fixed. The lack of correlation within the region suggests we do the following.

First obtain estimated probability densities for the Kähler invariant magnitudes in the canonically normalized fields, namely, $e^{\mathcal{K}/2}|W|$ and $e^{\mathcal{K}/2}|Z_{01}|$, as well as for the conifold distance. Draw a value from each distribution independently. If it has

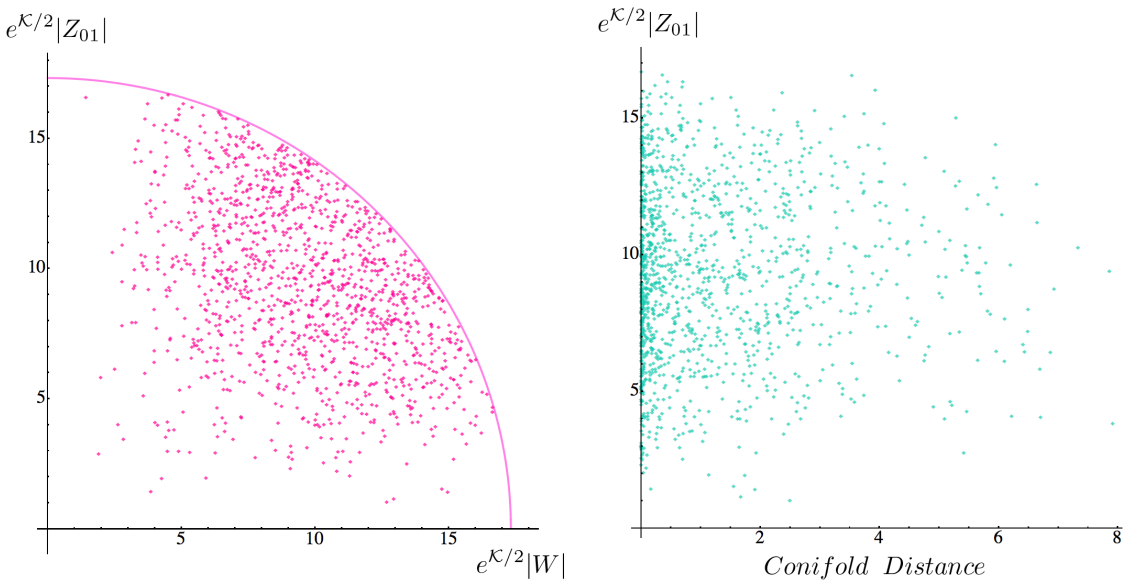

Figure 4.12: The left panel shows a scatter plot of the (Kähler independent) magnitude of the 01 entry of the Z matrix in canonical coordinates against the vev of the superpotential. The sharp quarter-circle boundary is a manifestation of the tadpole condition, with the radius of the arc being $\sqrt{L_{max}}$ which for us is $\sqrt{300}$. Within the region allowed by the tadpole condition the data points exhibit no correlation. The panel on the right displays a plot of the Z matrix entry against the remaining control parameter, the conifold distance. No correlation is evident between these either.

parameters (2) and (3) that violate inequality 4.3.21 dispose of it and redraw the triple until it is satisfied. Then compute the random eigenvalues, λ_1^2 and λ_2^2, by evaluating the Yukawa coupling at the randomly drawn conifold distance, and using it with the random $|Z_{01}|$ in eq. 4.3.14.

In figure 4.13 we display the resulting scatter plot for the $i = 1$ random mass pair — the artificial complex structure pair — atop that from our sample of actual flux vacua for the full range of masses. The image in the ellipsoidal window zooms in on the range where complex structure mass distributions peak. The RMM does a good job in reproducing the data's features in both regimes: the peak and the tail of the mass distributions. The same is true for the RMM's performance with the axio-dilaton mass pair. The two are virually indistinguishable in their superposed scatter plots, shown in figure 4.14.

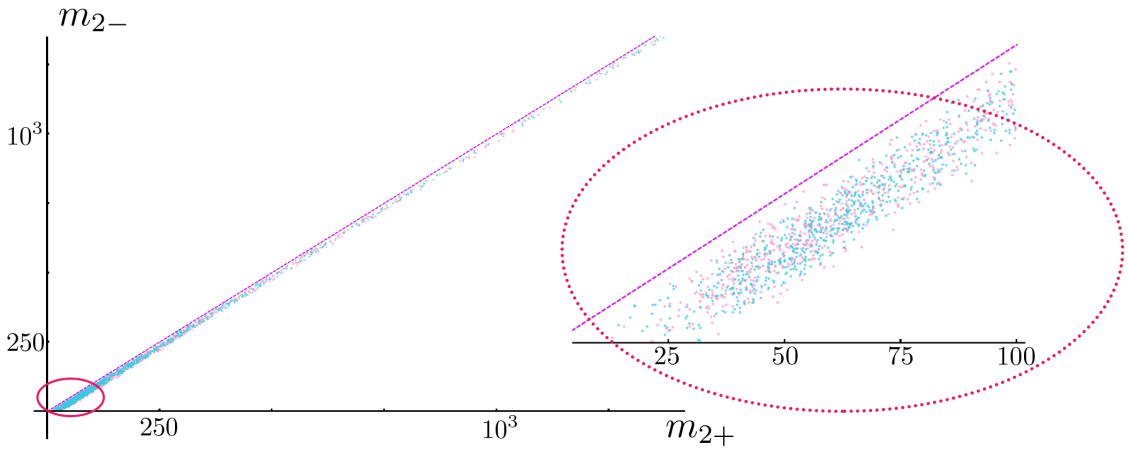

Figure 4.13: The random matrix model data for the artificial complex structure mass pair are plotted in light blue over that of the actual vacuum data, shown in light pink. The panel to the right magnifies the portion of the plot where the mass distributions peak.

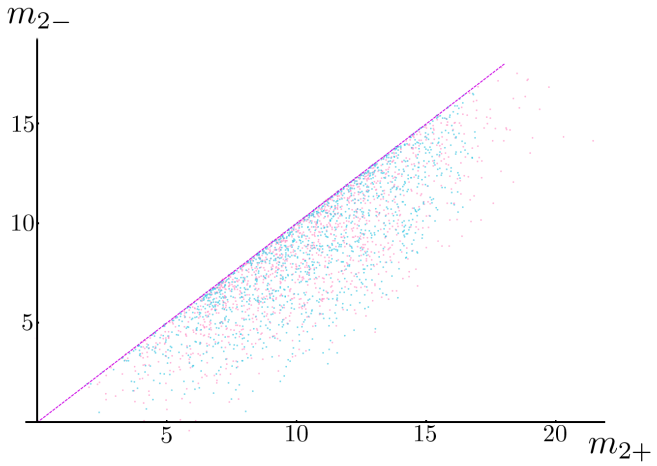

Figure 4.14: The random matrix model data for the artificial axio-dilaton mass pair are plotted in light blue over that of the actual vacuum data, shown in light pink.

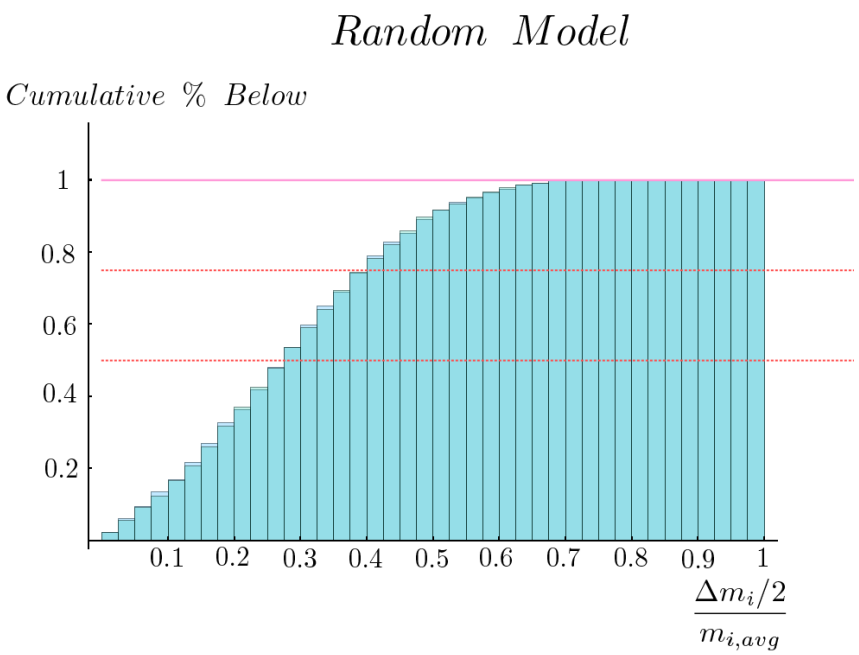

Figure 4.15: The analogous histograms to those in figure 4.11 for the random matrix model.

The scaled mass gap CDFs for the RMM also agree rather well with the actual data, and is shown in figure 4.15. It is worth noting that without the step in the RMM procedure that eliminates draws that live outside the quarter circle allowed by the tadpole condition there is a noticeable overdensity of RMM axio-dilaton data points away from the diagonal in the analogous version of figure 4.14. The effect on the complex structure's scatter plot of removing RMM tadpole condition is not perceptible.

Couplings

The hierarchy present in the masses, due to the fact that our vacua accumulate where the Yukawa coupling is singular, persists through the third and fourth order couplings. Since the basis in which couplings ought to be reported factors into one half associated almost entirely with the complex structure and the other with the axio-dilaton, we naively expect each additional index associated with the former at

the expense of the latter to involve the evaluation of increasingly more divergent terms near they singularity.

In particular, one expects four distinct scales to emerge among the distributions of third order coefficients, and five scales for the fourth order couplings. These correspond to the 3-choose-2 and 4-choose-2 ways one can differentiate the scalar potential. For instance, at third order we expect the $A_{i'j'k'}$ with all indices related to the complex structure (that is, equal to 1 or 2 in our convention for the basis of real canonically normalized fields) to be dominated by the term involving a derivative of the Yukawa coupling. The next highest scale expected would then be that with two complex structure and one axio-dilaton indices (3 or 4 in our convention), followed by one complex structure and two axio-dilaton, and lastly that with all three axio-dilaton.

First we establish that such a hierarchy of scales is realized, and then confirm the explanation in the preceding paragraph is valid by showing that the scale separation becomes ever more prominent as the vacuum-to-conifold distance diminishes. We then qualitatively investigate the correlations between the couplings at a given order, and indicate that they are *not* the result of the coordinate transformation alone. We accomplish this with the use of another random construction. Specifically, we generate a set of random rank three symmetric tensors and transform each by the orthogonal matrices from the actual set of vacuum data. Though one might expect correlations to be built in by the special structure of the Hessian's eigenspace, the fact that none of the correlations present in the mirror quintic data is replicated by the random procedure indicates that they are not the consequence of diagonalization.

Turning to the hierarchy among the magnitudes of the couplings, the scale separation can be shown visually by first imagining each of the entries in the third order couplings for a given vacuum, $A_{i'j'k'}$, as living in one of 64 cells of a 4-by-4-by-4 celled cube. We have one cube for each vacuum, and its entries take on positive or negative values (with equal likelihood, as indicated by the roughly Gaussian distributions cen-

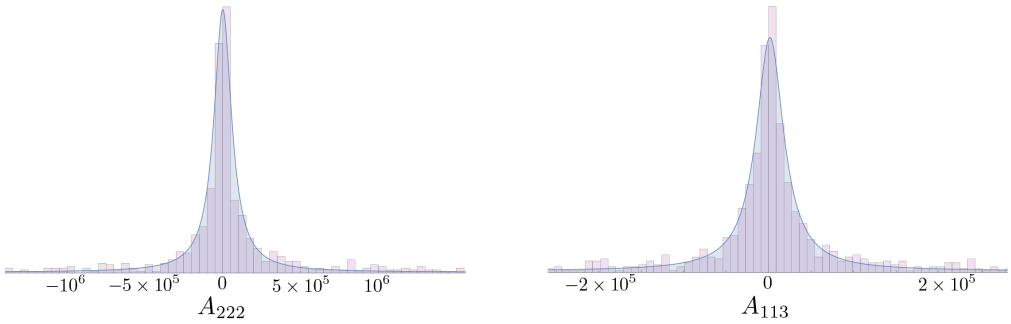

Figure 4.16: Representative example of the distributions of higher order couplings.

tered at zero found for all coefficients. A representative sample of the histograms and estimated distributions can be found in figure 4.16). Taking the labeling convention for the real and canonically normalized field coordinates defined in subsection 4.2, one 2-by-2-by-2 subblock in, say, the front-bottom corner of this cube will involve all complex structure related indices. The subblock diagonally opposite it in the top-far corner will involve all axio-dilaton indices, and the two types of mixed index subblocks will live interspersed throughout the remaining 6 off-diagonal subblocks.

Next, consider taking the magnitude of the value in each cell and then computing the median for each entry across the ensemble of cubes. The median is the more appropriate quantity because the distributions of the magnitudes are heavily skewed, just as the masses were. We may then represent the cube containing the ensemble's median values visually by coloring each cell according to a continuous scheme. The resulting hierarchy is, not surprisingly, best illustrated using a logarithmic scale. Two views of the resulting cube are shown in figure 4.17, with a color gradient of green to white to pink indicating smallest to largest.

The cube arranges itself into the four 8-celled subcubes of different scale, which we've described. This is indicated by the green quadrant, which is flanked by much paler green (identical by symmetry) subcubes adjacent to it, the vibrant pink quadrant diagonally across from the green corner and lastly the (identical) subcubes with pale pink and green cells that share an edge with the pink corner.

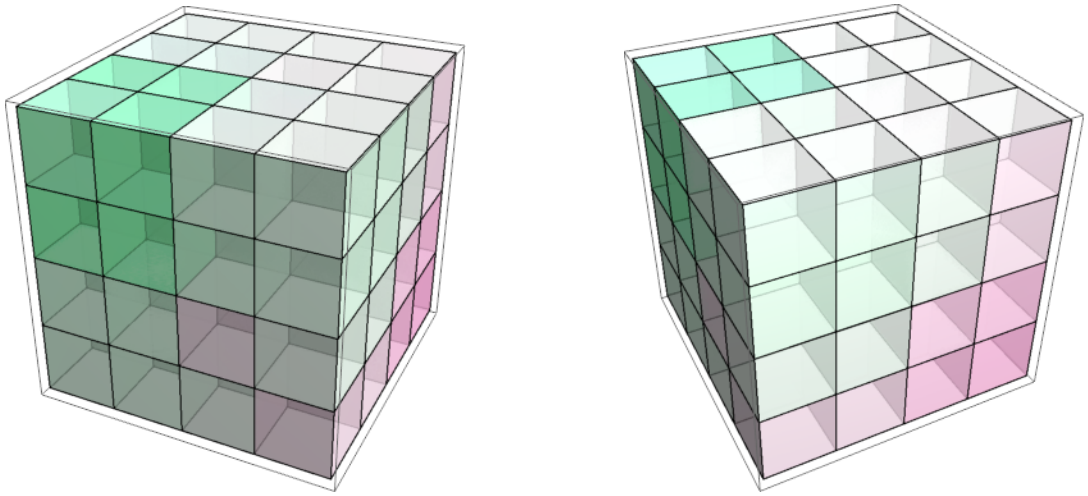

Figure 4.17: The median across the ensemble of the magnitude of the transformed third order couplings, $A_{i'j'k'}$. Each cell represents one choice for the three indices. $i' = 1$ or 2 corresponds to the complex structure associated eigenvectors, y_1 and y_2, whereas $i' = 3$ or 4 corresponds to the axio-dilaton associated eigenvectors, y_3 and y_4. The scale is logarithmic with green representing the smallest median magnitude and pink representing the largest. The "origin," so to speak, is located in the bottom right corner of the back face in the view of the cube in the left panel. The pink 2-by-2-by-2 subcube in this corner contains the all-complex-structure subset of couplings since the indices are all either 1 or 2. Similarly the green corner diagonally opposite contains the all-axio-dilaton couplings. The four expected hierarchies based on the leading order behavior of the Yukawa coupling near the conifold can be seen by the partitioning of the cube into four types of subblocks each with cell colors in a different regime of the scale: pink, light pink/pale green, light green, and green. A view of the cube rotated about the vertical axis is shown on the right.

The smallest couplings (green) do indeed reside in the all-axio-dilaton subblock, which is located at the top left of the front face of the cube in the first view. The pink corner is in fact the all-complex structure subblock. Its neighboring subcubes — those that share an edge with it (for instance those directly above and directly to the left of the pink corner in the front face of the second view) — still have two complex structure indices because they are in the same 2-cell thick "slice" of the cube, but have only one axio-dilaton index. The fact that the pale colors in these neighboring subcubes are pinker/less green than the pale subcubes that neighbor the green axio-dilaton corner means the ξ-ξ-σ couplings are larger than the other mixed index cubic couplings, ξ-σ-σ.

The hierarchy among the quartic couplings can be visualized in much the same way, only with a stack of four 64 celled cubes instead of a single one. We show two views of this hypercube in figure 4.18. The blocks are arranged top to bottom according to the first index, i', in $A_{i'j'k'l'}$; the top having $i' = 1$ and bottom having $i' = 4$. The color scheme here is CMYK with cyan/blue representing the smallest magnitude, followed by purple, magenta, orange, yellow, gray and finally black indicating the largest. Notice that each cube in the stack partitions itself into quadrants of four distinct scales (just like the single cube of third order couplings).

The top pair of blocks then has one additional index associated with the canonical complex structure coordinate, relative to the bottom pair with the canonical axio-dilaton. The largest magnitudes (the blackest cells) do in fact fill in the ξ-ξ-ξ subcube of the top pair of blocks. These are the all-complex-structure quartic couplings. These corner subcubes each share an edge with (identical) yellow subcubes. Since neighboring subcubes differ by one index type these neighbors contain couplings with three complex structure indices and one axio-dilaton. The fact that it is yellow means ξ-ξ-ξ-σ couplings rank second largest. Across from the black corner subcubes but within the same 2-cell thick slice we have the couplings that involve one more σ in place of ξ, the ξ-ξ-σ-σ couplings. The fact that they are orange indicates they are the third largest scale.

The remaining two scales in the hierarchy are displayed by the purple corners of the top pair of blocks in the stack and the blue corner cubes that are only present in the bottom two blocks in the stack. The purple corners of the top pair of blocks blocks do in fact lie diagonally opposite the black corners, making them cells containing ξ-σ-σ-σ couplings. The subcube located in this same top back corner position in the bottom pair of blocks in the stack differs from the purple ones of the preceding top pair in the stack by the first index, making them the all-axio-dilaton couplings. The cells are indeed cyan/blue, making these couplings the smallest in scale.

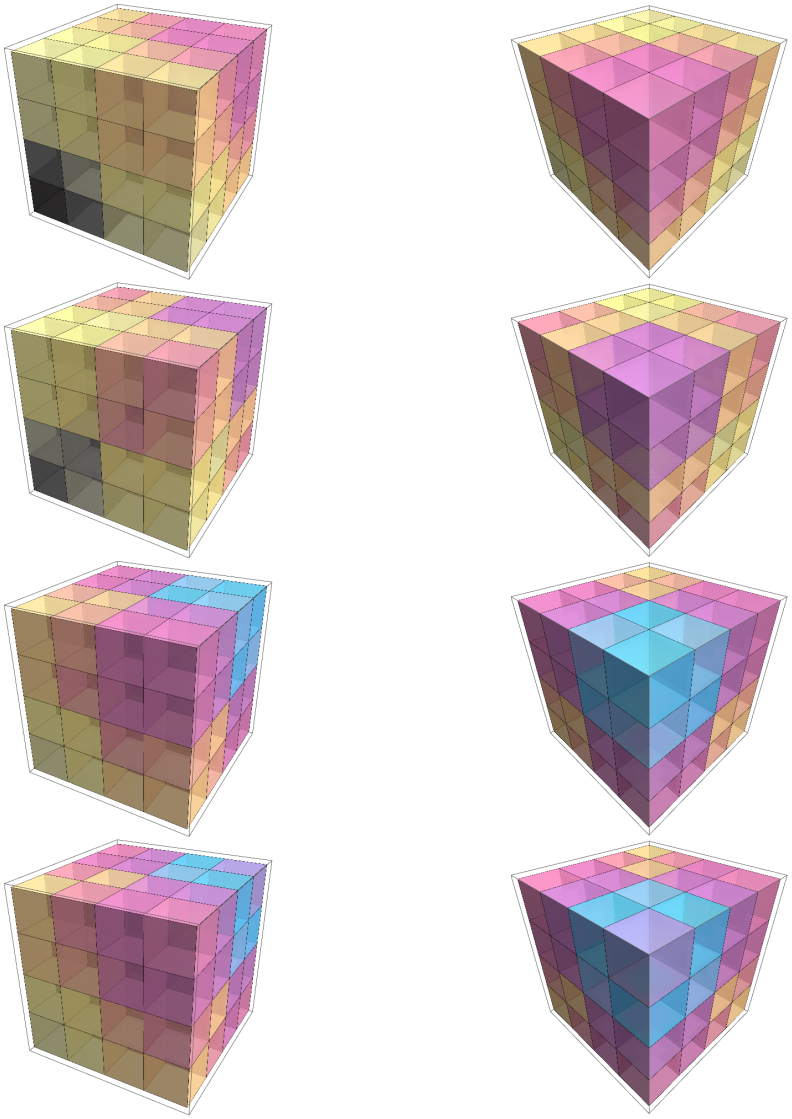

Figure 4.18: The analogous data as that displayed in figure 4.17 for the quartic couplings $A_{i'j'k'l'}$ with a logarithmic scale for the magnitudes represented with a CMYK color scheme (black being the largest, followed by yellow, magenta then cyan). The five scales expected due to the behavior of the Yukawa coupling near the conifold manifest themselves as the five different types of subcubes — those with cells in the black, yellow, orange/pink, pink/purple, and blue. The origin of each of the four cubes in the stack is at the bottom left of the front face in the view on the left, making the all-complex-structure-couplings contained in the black corners of the top pair of cubes. The panel on the right shows a view of the hypercube rotated about the vertical axis, with the all-axio-dilaton couplings in the top front corner of the bottom pair of cubes in the stack, which are blue as expected.

Now that we've confirmed the existence of the naively expected hierarchies we turn to their source — the proximity to the conifold point. A priori it is possible that the divergent contributions due to the Yukawa coupling and its derivatives could have been tempered by some other mechanism as the conifold is approached. It is also important to assess the degree of variation in the expected scale separation. Just as the vev of the superpotential played the role of a random element complicating an otherwise clean analytic dependence on the conifold distance, here too we will have a layer of noise atop the signal. The significance of this noise, and importantly the degree to which it changes as the conifold is approached, is not obvious at the outset.

We show the conifold distance dependence of the cubic couplings' scale separation visually as well. For each vacuum's four independent 8-cell subcubes we first compute each subcube's mean magnitude. The mean is the appropriate measure here since the entries in a single subcube for *an individual* vacuum *are* comparable. Each vacuum then has a list of four positive values — the average magnitude of each of the four type of cubic couplings. We take the logarithm of each value in the list, as well that of the magnitude of the canonical vacuum coordinate, $|\xi_{vac}|$. The ensemble data for all four types of cubic couplings are displayed in the single log-log scatter plot in figure 4.19, with different colors used for each of the four types.

Notice first that the colors separate into four approximately linear bands with negative slope. This indicates that each type of coupling has an inverse power law dependence on the canonical vacuum coordinate, $|\xi_{vac}|$. The data points with most negative slope, the pink band, are the ensemble of all-complex-structure cubic couplings. Each pink point is a different vacuum's mean ξ-ξ-ξ —type coupling magnitude. Below this band lies the second largest scale in the cubic couplings involving two ξ and one σ, shown in teal, followed by purple and navy blue for the σ-σ-ξ and the all-axio-dilaton couplings, respectively. The fact that the bands are approximately linear reflects the domination of the leading order term in the Yukawa coupling and

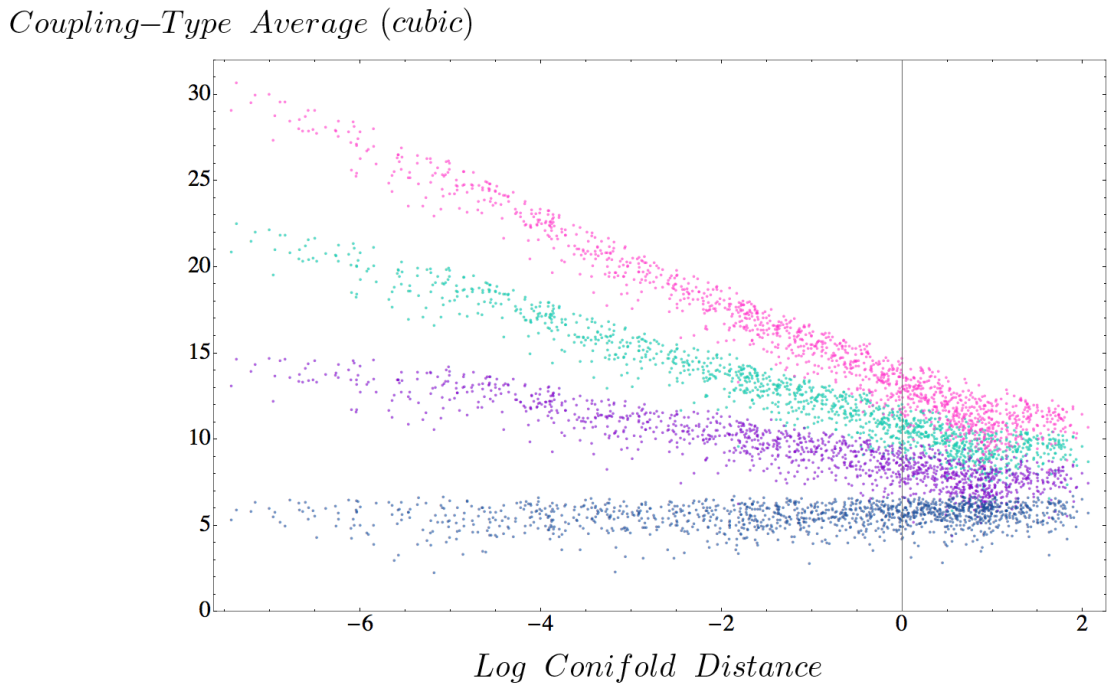

Figure 4.19: A log-log scatter plot of the vacuum cubic couplings' subcube average magnitude versus conifold distance. Each subcube contains couplings of one of the four types: all-ξ (shown in pink), ξ-ξ-σ (green), ξ-ξ-σ (purple), and all-σ (navy). The fact that the data points organize themselves into approximately linear bands with increasingly negative slope for each ξ at the expense of a σ confirms the Yukawa coupling (through its successively more singular partial derivatives) is responsible for the hierarchy observed. The width of individual bands signals the presence/role of the random element, the vev of the superpotential.

derivatives thereof over other terms in the expressions for the cubic couplings.

The same analysis can be performed for the quartic couplings. We show the resulting log-log scatter plot for the five types of couplings in figure 4.20, with the same coloring scheme descending from the largest in pink (ξ-ξ-ξ-ξ–type), and the addition of a fifth color, light-blue, for the smallest (all-axio-dilaton type). The same reasoning indicates that the source of the hierarchy among the quartic couplings are the terms involving the most ξ derivatives of Yukawa coupling evaluated near the conifold point. For both the cubic and the quartic scatter plots we may view the statistical variation within a given band as being supplied by the random element,

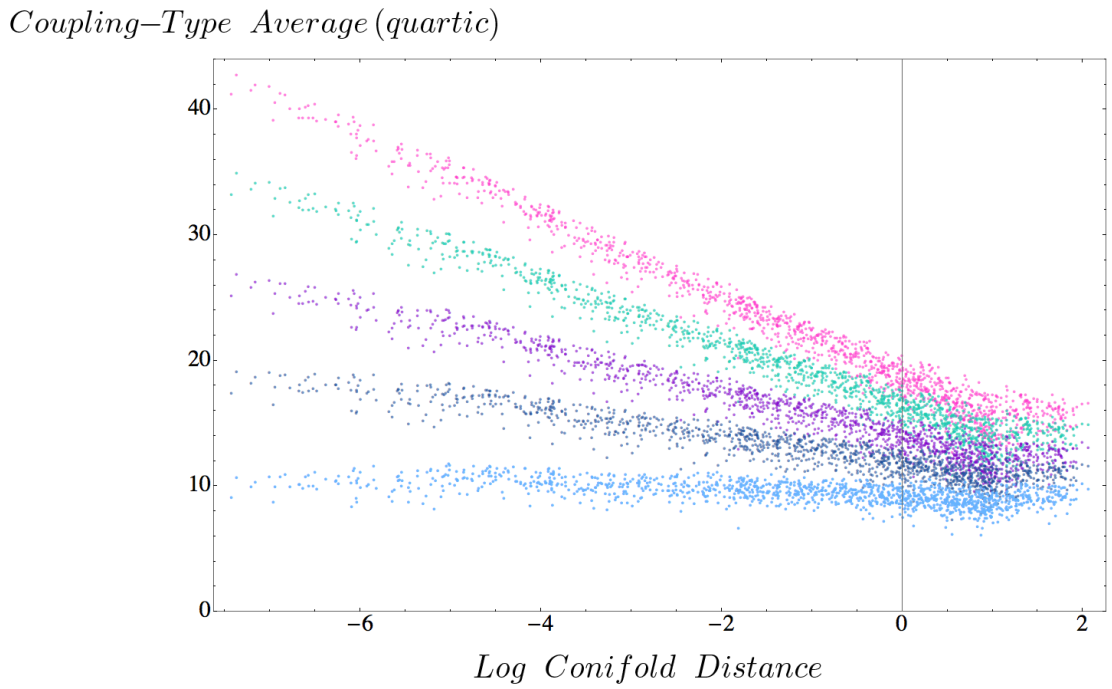

Figure 4.20: The analogous plot as that in figure 4.19 for the quartic couplings. The colors are ordered in the same manner according to the number of ξ's in the coupling-type, descending from all-ξ (pink), with the addition of light-blue for the last of the five types, all-σ. The self organization of the vacuum data into the approximately linear bands of increasingly negative slope for every ξ at the expense of a σ confirms the validity of our explanation of the hierarchies based on the behavior of the Yukawa coupling near the conifold.

the vev of the superpotential.

We conclude with a qualitative discussion of the remaining aspect of the structure among the couplings that is not captured by a Random Matrix Model, for example that of [37]. These are the pattern of nontrivial correlations we find between couplings. That is, the ensemble of $A_{i'j'k'}$ and $A_{i'j'k'l'}$ are *not* accurately modeled by totally symmetric tensors whose entries are drawn separately from independent distributions. We've seen that the distribution of a particular cubic or quartic coupling is roughly Gaussian and is centered at zero. The hierarchies discussed mean that the spread of these distributions differ in scale, according to index type. For instance the A_{112} distribution is comparable to A_{222} in this regard, but not to, say, A_{113}, whose spread

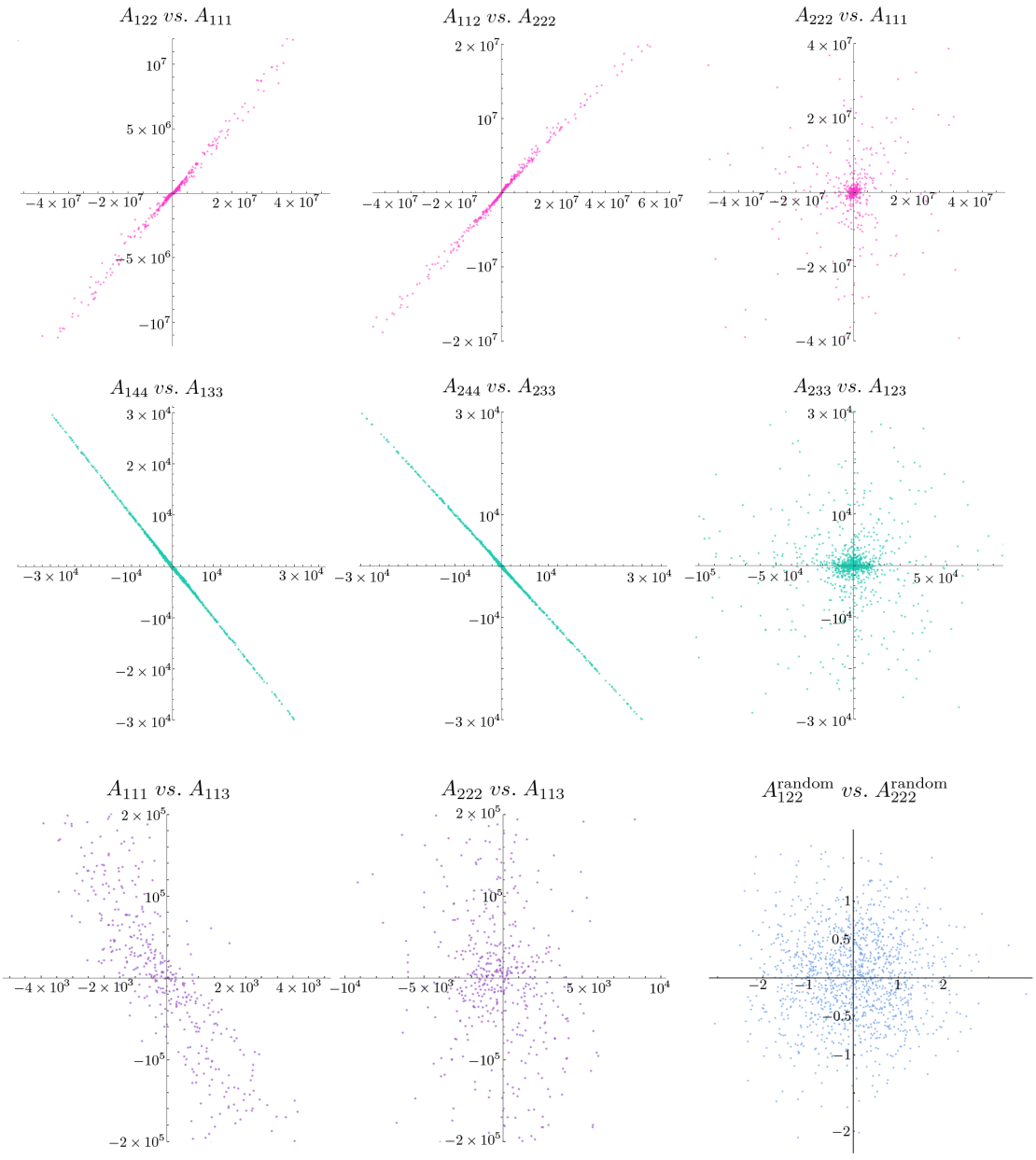

Figure 4.21: A representative sample of the scatter plots of pairs of cubic and quartic couplings from the vacuum data (pink, green, and purple), as well as from the random matrix model couplings (blue) designed as a diagnostic. Note that whereas the vacuum data exhibits sharply defined correlations between certain pairs of couplings, all the random matrix model pairs do not. This indicates that correlations are not merely built in by the diagnoalization of the Hessian in canonical coordinates.

is smaller by comparison.

The hierarchies and the non-flat distributions themselves need not have come with correlations between couplings. The fact that we find approximately linear scatter plots between particular pairs of couplings renders a random approach involving independent distributions — uniform or otherwise — a poor approximation to the actual coefficients. A representative sample of the nontrivial correlations for the cubic coupling data sets are shown eight of the nine panels in figure 4.21, excluding that in the bottom right corner (in blue).

The pink plots on the top row show that while the pairs A_{111} with A_{122}, and A_{112} with A_{222} have an approximately constant ratio across the ensemble of vacua, there is no relationship between A_{111} and A_{222}. We also find correlations in the couplings of medium scale, namely those that mix moduli type. For instance, A_{144} and A_{133} are approximately equal in magnitude, but opposite in sign, across models. This is shown in the teal plots in the middle row.

A reasonable hypothesis for the source of these correlations is the transformation performed to the field coordinates that simultaneously diagonalize the Hessian and canonically normalizes the kinetic terms. This seemingly mundane step in the processing of the raw coupling data might be suspected as being nontrivial at the level of correlations because of the special structure of the Hessian's eigenspace. We test this hypothesis by comparing the results of a modified Random Matrix Model designed entirely as a diagnostic for this purpose.

If it is the case that the transformation from the original noncanonical complex coordinates builds in the patterns of correlations we observe, then an ensemble of real and totally symmetric tensors with i.i.d. entries acted upon by the orthogonal transformation O (defined in subsection 4.2) ought to exhibit correlations. Since we have 1358 O matrices, we build the same number of random rank-3 tensors and

perform the transformation,

$$A^{rand}_{ijk} \to O^i_{i'} O^j_{j'} O^k_{k'} A^{rand}_{ijk}. \tag{4.3.22}$$

The result is that the transformed random couplings are uncorrelated. We've included a single scatter plot of these RMM couplings as a representative example. This is the ninth panel in figure 4.21.

4.4 Discussion

The initial expectation that string theory would result in a unique, or nearly unique, vacuum state whose low energy excitations would explain the familiar properties of particle physics has not been borne out by developments over the past few decades. Instead, a wealth of discoveries have revealed an ever greater abundance of mathematically consistent vacua, without any allied developments that single out one (or perhaps a few) such vacua as physically relevant. Because of this, significant attention has shifted to statistical properties of these vacua and, more generally, to statistical properties of the easier to analyze surrogate, random field theories in high-dimensional moduli spaces.

In this work, we have investigated the degree to which this latter surrogate faithfully models the space of low energy field theories arising from string compactifications. We reviewed arguments which suggest the relevance of random field theories — namely, the randomizing effects of arbitrary fluxes coupled with the broad spectrum of vacuum locations in moduli space associated with each such flux choice. We then tested this argument by focusing our attention on one particular compactification of the type IIb string, the famous mirror to the quintic hypersurface. We identified a class of 1358 low energy flux models built on this compactification, computed the scalar potential for the canonically normalized scalar fields in each such model, and

considered the statistical distributions of the renormalizable coefficients in the Taylor expansions of the potentials. We confirmed previously known results for the second order coefficients — mass terms — and went on to study the third and fourth order terms. Our main result is that we found significant deviations from a random collection of coefficients, as illustrated in figures 4.17, 4.18 and 4.21, showing that some of the rich structure inherent in type IIb supergravity survives the randomizing influence of flux compactifications.

The lesson, then, is that one must exercise care when invoking random field theories as a model for the space of low energy compactified string dynamics. More particularly, our results, and generalizations thereof to higher dimensional moduli spaces, provide a sharper ensemble for accurate statistical modeling of the features of low energy string theory.

Going forward, these results suggest a number of research directions. For ease of computation we have focused on a Calabi-Yau compactification with a single complex structure modulus. One would like to acquire an understanding of the distributions we have studied in more generic cases with higher dimensional moduli spaces. Explicit analysis of the sort we've undertaken here would be difficult. However, in the vicinity of a conifold locus — where vacua generally accumulate — we've reduced the statistical dependence to the three dominant control parameters introduced earlier.

These each have natural higher dimensional generalizations and so it would be of interest to see if we can gain insight into more general Calabi-Yau compactifications guided by the results we found here, and thus avoiding direct calculation. Our results also suggest revisiting the work [37], which have investigated the quantum stability of vacua in random high dimensional scalar field theories as a surrogate for the stability of the string landscape; specifically assessing whether decay rates are modified by using a collection of random field theories whose distribution more closely aligns our findings.

Bibliography

[1] S. Coleman, "Fate of the false vacuum: Semiclassical theory," *Physical review d*, vol. 16, no. 4, pp. 1248–1248, 1977. DOI: 10.1103/physrevd.16.1248.

[2] M. Dine, "Naturalness Under Stress," *Annual review of nuclear and particle science*, vol. 65, pp. 43–62, 2015. DOI: 10.1146/annurev-nucl-102014-022053. arXiv: 1501.01035 [hep-ph].

[3] S. Coleman and J. Mandula, "All possible symmetries of the s-matrix," *Physical review*, vol. 159, no. 5, pp. 1251–1256, 1967. DOI: 10.1103/physrev.159.1251.

[4] R. Haag, J. T. Łopuszański, and M. Sohnius, "All possible generators of supersymmetries of the s-matrix," *Nuclear physics b*, vol. 88, no. 2, pp. 257–274, 1975. DOI: 10.1016/0550-3213(75)90279-5.

[5] J. D. Lykken, "Introduction to supersymmetry," in *Fields, strings and duality. Proceedings, Summer School, Theoretical Advanced Study Institute in Elementary Particle Physics, TASI'96, Boulder, USA, June 2-28, 1996*, 1996, pp. 85–153. arXiv: hep-th/9612114 [hep-th]. [Online]. Available: http://lss.fnal.gov/cgi-bin/find_paper.pl?pub-96-445-T.

[6] M. B. Green, J. H. Schwarz, and E. Witten, *Superstring theory: Volume 2, loop amplitudes, anomalies and phenomenology (cambridge monographs on mathematical physics)*. Cambridge University Press, 1988, ISBN: 9780521357531.

[7] F. Denef, "Les Houches Lectures on Constructing String Vacua," in *String Theory And The Real World: From Particle Physics To Astrophysics. Proceedings, Summer School in Theoretical Physics, 87th Session, Les Houches, France, July 2-27, 2007*, 2008, pp. 483–610. arXiv: 0803.1194 [hep-th]. [Online]. Available: https://inspirehep.net/record/780946/files/arXiv:0803.1194.pdf.

[8] J. Overduin and P. Wesson, "Kaluza-klein gravity," *Physics reports*, vol. 283, no. 5-6, pp. 303–378, 1997. DOI: 10.1016/s0370-1573(96)00046-4.

[9] R. Rattazzi, "Cargese lectures on extra-dimensions," in *Particle physics and cosmology: The interface. Proceedings, NATO Advanced Study Institute, School, Cargese, France, August 4-16, 2003*, 2003.

[10] M. Dine and N. Seiberg, "Is the Superstring Weakly Coupled?" *Physics letters*, vol. B162, pp. 299–302, 1985. DOI: 10.1016/0370-2693(85)90927-X.

[11] R. Bousso and J. Polchinski, "Quantization of four-form fluxes and dynamical neutralization of the cosmological constant," *Journal of high energy physics*, vol. 2000, no. 06, pp. 006–006, 2000. DOI: 10.1088/1126-6708/2000/06/006.

[12] L. Susskind, "The anthropic landscape of string theory," Feb. 27, 2003. arXiv: hep-th/0302219 [hep-th].

[13] S. Kachru, R. Kallosh, A. Linde, and S. P. Trivedi, "De sitter vacua in string theory," *Physical review d*, vol. 68, no. 4, 2003. DOI: 10.1103/physrevd.68.046005.

[14] S. B. Giddings, S. Kachru, and J. Polchinski, "Hierarchies from fluxes in string compactifications," *Physical review d*, vol. 66, no. 10, 2002. DOI: 10.1103/physrevd.66.106006.

[15] S. Gukov, C. Vafa, and E. Witten, "CFT's from Calabi-Yau four folds," *Nucl. phys.*, vol. B584, pp. 69–108, 2000, [Erratum: Nucl. Phys.B608,477(2001)]. DOI: 10.1016/S0550-3213(01)00289-9,10.1016/S0550-3213(00)00373-4. arXiv: hep-th/9906070 [hep-th].

[16] K. Dasgupta, G. Rajesh, and S. Sethi, "M theory, orientifolds and G - flux," *Journal of high energy physics*, vol. 08, p. 023, 1999. DOI: 10.1088/1126-6708/1999/08/023. arXiv: hep-th/9908088 [hep-th].

[17] G. Curio, A. Klemm, D. Lust, and S. Theisen, "On the vacuum structure of type II string compactifications on Calabi-Yau spaces with H fluxes," *Nucl. phys.*, vol. B609, pp. 3–45, 2001. DOI: 10.1016/S0550-3213(01)00285-1. arXiv: hep-th/0012213 [hep-th].

[18] E. Silverstein, "(A)dS Backgrounds from Asymmetric Orientifolds," Jun. 22, 2001. arXiv: hep-th/0106209v1 [hep-th].

[19] B. R. Greene, "String Theory on Calabi-Yau Manifolds," in *Fields, strings and duality. Proceedings, Summer School, Theoretical Advanced Study Institute in Elementary Particle Physics, TASI'96, Boulder, USA, June 2-28, 1996*, 1996, pp. 543–726. arXiv: hep-th/9702155 [hep-th].

[20] S.-T. Yau, "Calabi's Conjecture and some new results in algebraic geometry," *Proc. nat. acad. sci.*, vol. 74, pp. 1798–1799, 1977. DOI: 10.1073/pnas.74.5.1798.

[21] P. Candelas and X. C. de la Ossa, "Moduli space of calabi-yau manifolds," *Nuclear physics b*, vol. 355, no. 2, pp. 455–481, 1991. DOI: 10.1016/0550-3213(91)90122-e.

[22] P. Candelas, "Yukawa couplings between (2, 1)-forms," *Nuclear physics b*, vol. 298, no. 3, pp. 458–492, 1988. DOI: 10.1016/0550-3213(88)90351-3.

[23] T. W. Grimm, "The Effective Action Of Type II Calabi-Yau Orientifolds," *Fortschritte der physik*, vol. 53, pp. 1179–1271, 2005. DOI: 10.1002/prop.200510253. arXiv: hep-th/0507153 [hep-th].

[24] V. Bouchard, "Lectures On Complex Geometry, Calabi-Yau Manifolds and Toric geometry," 2007. arXiv: hep-th/0702063 [hep-th].

[25] A. Strominger, "Special Geometry," *Communications in mathematical physics*, vol. 133, pp. 163–180, 1990. DOI: 10.1007/BF02096559.

[26] T. C. Bachlechner, K. Eckerle, O. Janssen, and M. Kleban, "Axions of evil," 2017. arXiv: 1703.00453v2 [hep-th].

[27] M. Graña, "Flux compactifications in string theory: A comprehensive review," *Physics reports*, vol. 423, no. 3, pp. 91–158, 2006. DOI: 10.1016/j.physrep.2005.10.008.

[28] M. R. Douglas and S. Kachru, "Flux compactification," *Reviews of modern physics*, vol. 79, no. 2, pp. 733–796, 2007. DOI: 10.1103/revmodphys.79.733.

[29] L. B. Anderson, Y.-H. He, and A. Lukas, "Heterotic Compactification, An Algorithmic Approach," *Journal of high energy physics*, vol. 07, p. 049, 2007. DOI: 10.1088/1126-6708/2007/07/049. arXiv: hep-th/0702210 [hep-th].

[30] L. B. Anderson, J. Gray, A. Lukas, and B. Ovrut, "Stabilizing The Complex Structure in Heterotic Calabi-Yau Vacua," 2010. DOI: 10.1007/JHEP02(2011)088. arXiv: 1010.0255 [hep-th].

[31] L. B. Anderson, J. Gray, A. Lukas, and B. Ovrut, "Stabilizing All Geometric Moduli in Heterotic Calabi-Yau Vacua," *Physical review d*, vol. 83, p. 106 011, 2011. DOI: 10.1103/PhysRevD.83.106011. arXiv: 1102.0011 [hep-th].

[32] M. Cicoli and F. Quevedo, "String moduli inflation: An overview," *Classical and quantum gravity*, vol. 28, no. 20, p. 204 001, 2011. DOI: 10.1088/0264-9381/28/20/204001.

[33] S. Kachru, M. Schulz, and S. P. Trivedi, "Moduli stabilization from fluxes in a simple IIB orientifold," *Journal of high energy physics*, vol. 2003, no. 10, pp. 007–007, 2003. DOI: 10.1088/1126-6708/2003/10/007.

[34] F. Denef, M. R. Douglas, B. Florea, A. Grassi, and S. Kachru, "Fixing all moduli in a simple f-theory compactification," *Advances in theoretical and mathematical physics*, vol. 9, no. 6, pp. 861–929, 2005. DOI: 10.4310/atmp.2005.v9.n6.a1.

[35] F. Denef and M. R. Douglas, "Distributions of flux vacua," *Journal of high energy physics*, vol. 2004, no. 05, pp. 072–072, 2004. DOI: 10.1088/1126-6708/2004/05/072.

[36] F. Denef and M. R. Douglas, "Distributions of Nonsupersymmetric Flux Vacua," *Journal of high energy physics*, vol. 03, pp. 061–061, 2005. DOI: 10.1088/1126-6708/2005/03/061.

[37] B. Greene, D. Kagan, A. Masoumi, D. Mehta, E. J. Weinberg, and X. Xiao, "Tumbling through a landscape: Evidence of instabilities in high-dimensional moduli spaces," *Physical review d*, vol. 88, no. 2, 2013. DOI: 10.1103/physrevd.88.026005.

[38] R. Easther and L. McAllister, "Random matrices and the spectrum of n-flation," *Journal of cosmology and astroparticle physics*, vol. 2006, no. 05, pp. 018–018, 2006. DOI: 10.1088/1475-7516/2006/05/018.

[39] D. Marsh, L. McAllister, and T. Wrase, "The wasteland of random supergravities," *Journal of high energy physics*, vol. 2012, no. 3, 2012. DOI: 10.1007/jhep03(2012)102.

[40] C. G. Callan and S. Coleman, "Fate Of The False Vacuum. II. First Quantum Corrections," *Physical review d*, vol. 16, no. 6, pp. 1762–1768, 1977. DOI: 10.1103/physrevd.16.1762.

[41] S. Coleman and F. D. Luccia, "Gravitational effects on and of vacuum decay," *Physical review d*, vol. 21, no. 12, pp. 3305–3315, 1980. DOI: 10.1103/physrevd.21.3305.

[42] P. Ahlqvist, K. Eckerle, and B. Greene, "Bubble universe dynamics after free passage," *Journal of high energy physics*, vol. 2015, no. 3, 2015. DOI: 10.1007/jhep03(2015)031.

[43] R. Easther, J. T. Giblin, L. Hui, and E. A. Lim, "New mechanism for bubble nucleation: Classical transitions," *Physical review d*, vol. 80, no. 12, 2009. DOI: 10.1103/physrevd.80.123519.

[44] J. T. Giblin Jr, L. Hui, E. A. Lim, and I.-S. Yang, "How to Run Through Walls: Dynamics of Bubble and Soliton Collisions," *Phys. rev.*, vol. D82, p. 045 019, 2010. DOI: 10.1103/PhysRevD.82.045019. arXiv: 1005.3493 [hep-th].

[45] A. Aguirre, M. C. Johnson, and M. Tysanner, "Surviving the crash: Assessing the aftermath of cosmic bubble collisions," *Physical review d*, vol. 79, no. 12, 2009. DOI: 10.1103/physrevd.79.123514.

[46] M. C. Johnson, H. V. Peiris, and L. Lehner, "Determining the outcome of cosmic bubble collisions in full general relativity," *Physical review d*, vol. 85, no. 8, 2012. DOI: 10.1103/physrevd.85.083516.

[47] S. Coleman, *Aspects of symmetry*. Cambridge University Press, 1985. DOI: 10.1017/cbo9780511565045.

[48] P. Ahlqvist, K. Eckerle, and B. Greene, "Kink collisions in curved field space," *Journal of high energy physics*, vol. 2015, no. 4, 2015. DOI: 10 . 1007 / jhep04(2015)059.

[49] K. Eckerle and B. Greene, "Random field theories in the mirror quintic moduli space," Aug. 18, 2016. arXiv: 1608.05189v1 [hep-th].

[50] P. Ahlqvist, B. R. Greene, D. Kagan, E. A. Lim, S. Sarangi, and I.-S. Yang, "Conifolds and Tunneling in the String Landscape," *Journal of high energy physics*, vol. 03, p. 119, 2011. DOI: 10.1007/JHEP03(2011)119. arXiv: 1011.6588 [hep-th].

[51] M. C. D. Marsh, B. Vercnocke, and T. Wrase, "Decoupling and de sitter vacua in approximate no-scale supergravities," *Journal of high energy physics*, vol. 2015, no. 5, 2015. DOI: 10.1007/jhep05(2015)081.

[52] P. Candelas, X. C.D. L. Ossa, P. S. Green, and L. Parkes, "A pair of calabi-yau manifolds as an exactly soluble superconformal theory," *Nuclear physics b*, vol. 359, no. 1, pp. 21–74, 1991. DOI: 10.1016/0550-3213(91)90292-6.

Appendix: Near Conifold Period Expansion Coefficients

Recall that our integral and symplectic basis for mirror quintic's period functions are denoted Π_i, with $i = 0$ and 3 an intersecting pair, and $i = 1$ and 2 the other. Π_0 is the only non-analytic period at the conifold point. It's partner, Π_3, is the period obtained by integrating the holomorphic 3-form over the cycle that collapses. This period is nevertheless well-behaved (it simply vanishes at the conifold). The two periods associated with the other intersecting pair of cycles are also analytic. These are nonvanishing. The following expansions about the conifold point at $z = 1$ hold,

$$\Pi_1(z) = \sum_{n=0}^{q} b_n (z-1)^n \tag{4.4.1}$$

$$\Pi_2(z) = \sum_{n=0}^{q} c_n (z-1)^n \tag{4.4.2}$$

$$\Pi_3(z) = \sum_{n=1}^{q} d_n (z-1)^n. \tag{4.4.3}$$

The values for the coefficients were computed in Mathematica by evaluating derivatives of the expressions for the Π_i in terms of the Meijer-G functions (the U_i) at the conifold. We used 40 digit accuracy in these computations. The values are listed in Table 1.

n	b_n	c_n	d_n
0	$+1.293574i$	$6.19502 - 7.11466i$	0
1	$-0.150767i$	$-1.016605 + 0.829217i$	$-0.355881i$
2	$+0.0777445i$	$0.570733 - 0.427595i$	$0.249117i$
3	$-0.0522815i$	$-0.401804 + 0.287548i$	$-0.194548i$
4	$+0.0393684i$	$0.312044 - 0.216526i$	$0.161285i$
5	$-0.0315669i$	$-0.256050 + 0.173618i$	$-0.138686i$
6	$+0.0263447i$	$0.217649 - 0.144896i$	$0.122217i$
7	$-0.0226046i$	$-0.189607 + 0.124325i$	$-0.109620i$
8	$0.0197941i$	$0.168193 - 0.108868i$	$0.0996353i$

Table 1: Expansion coefficients for period functions Π_1, Π_2 and Π_3.

The remaining period, Π_0, is multiple-valued at the conifold point. The cycle it is associated with picks up one copy of its vanishing partner for each revolution around the conifold in moduli space. This fixes the form of Π_0 to 4.1.74. To match

the branch cuts of the logarithm in the expansion with that of the relevant Mejer-G (U_0) in Mathematica we must negate the argument of the logarithm. Ultimately the expression we write for Π_0 is,

$$\Pi_0(z) = \Pi_3(z)\left(\frac{\log(-(z-1))}{2\pi i} - \frac{1}{2}\right) + f(z) \tag{4.4.4}$$

with $f(z)$ analytic.

Its expansion coefficients, a_n, were computed using a recursion relation based on the fact Π_0 satisfies the Picard-Fuchs equation. This is discussed at length in section 4.1. Here we simply tabulate the resulting values. The first three a_n are needed by the recursion to generate the rest. They are obtained numerically, as discussed in section 4.1. All coefficients were calculated using 30–40 digit accuracy computations and are listed in Table 2.

n	a_n
0	1.07073
1	$0.024708 - 0.177941i$
2	$-0.0115108 + 0.1245584i$
3	$0.0065650 - 0.0972742i$
4	$-0.0042768 + 0.0806427i$
5	$0.0030290 - 0.0693428i$
6	$-0.0022701 + 0.0611087i$
7	$0.0017719 - 0.0548102i$
8	$-0.0014261 + 0.0498177i$

Table 2: Expansion coefficients for analytic contribution to Π_0